Safety-related Investigations on a soluble-boron-free Small Modular Reactor Core

Zur Erlangung des akademischen Grades einer
DOKTORIN DER INGENIEURWISSENSCHAFTEN (Dr.-Ing.)

von der KIT-Fakultät für Maschinenbau des
Karlsruher Instituts für Technologie (KIT)
angenommene

DISSERTATION

von

M.Sc.Yi Song

Tag der mündlichen Prüfung: 11.03.2026

Hauptreferent: Prof. Dr.-Ing. Xu Cheng

Korreferent: Prof. Dr. Tengfei Zhang

Acknowledgements

My deepest appreciation goes to my academic supervisors. I am profoundly grateful to Prof. Stieglitz for offering me the invaluable opportunity to pursue my PhD in the RPD group. After his unexpected passing, I would like to thank Prof. Cheng for generously taking me under his supervision and providing steadfast support and guidance throughout my thesis writing and defence preparation.

My sincere thanks also go to Dr. Victor Sanchez, my group leader and my advisor, for guiding me in defining my research direction and for his helpful reviews of my journal papers and PhD thesis.

I would also like to thank Prof. Zhang for kindly reviewing my thesis and offering insightful feedbacks.

I would like to express my heartfelt gratitude to the China Scholarship Council for sponsoring my studies abroad.

I am also thankful to my colleagues—Luigi Mercatali, Kanglong, Gianfranco and Alejandro—for having regular brainstorms and discussions about my work. In addition, I extend my thanks to all my colleagues at INR and IATF for the many meaningful academic exchanges and casual conversations we shared.

On a personal level, I owe sincere thanks to my best friend in Germany, Julian, for his constant companionship and support, which made my daily life abroad much more manageable and enjoyable.

Reflecting on these years, I see my PhD journey as a challenging yet rewarding process of gradual, upward growth. There were many moments of uncertainty and doubt, but step by step, I kept moving forward and have now reached what once seemed a distant finish line. Above all, I thank myself for never giving up. This perseverance has revealed to me the resilient strength within my own heart. Whatever challenges lie ahead, I will carry this spirit with me, drawing on it to move forward and overcome.

Abstract

Many water-cooled small modular reactors (WC-SMRs) are being developed and their deployment is being considered in different countries world-wide, with some designs considering no soluble boron in the coolant. The elimination of soluble boron offers several advantages such as an enhanced negative moderator temperature coefficient, reduced corrosion, and simplified chemical systems, etc. leading to the growing interest in soluble-boron-free (SBF) SMR-designs.

However, the removal of soluble boron introduces distinct challenges in core design and safety. Without soluble boron for distributed reactivity control, excess reactivity control relies entirely on burnable absorbers and control rods, potentially increasing power peaking factors. Due to the small size of the SMR core, careful core design is necessitated to ensure safety margins. Moreover, the higher total worth of control rod system in a SBF SMR, compared to a boron-based SMR, may result in an excessively high single control rod worth, may damaging the cooling capability in the event of a hypothetical rod ejection accident.

This doctoral thesis addresses these challenges by establishing a methodology for SBF-SMR-core optimization across first and equilibrium cycles. Building on the foundational academic KSMR-core design, which previously focuses solely on fresh fuel performance at beginning of cycle, this research extends the investigation to core behaviour throughout the entire burnup cycle. The work develops the SBF SMR core using mature PWR technology with UO_2 enrichment below 5% and Gd_2O_3 as burnable absorber material. The design optimization process involves defining a set of fixed parameters and variables (including fuel enrichment, burnable absorber rod configuration, and Gd_2O_3 content), and then systematically exploring this large variable space to identify optimal configurations. The two-step approach is applied in this process: CASMO5 generate cross sections and SIMULATE5 use these data to conduct the core simulation. A Golang-based tool, named CoreOptimizer, was developed to automate the input file generation, simulation execution and output data extraction, enabling efficient core optimization.

Finally, the optimal core configurations undergo the neutronic and safety evaluations throughout first and equilibrium cycles to ensure target cycle length achievement while satisfying all safety criteria. Furthermore, a hypothetical control rod ejection accident was simulated to confirm the safety performance of the optimized cores under design-basis accident conditions.

Kurzfassung

Weltweit werden zahlreiche wassergekühlte SMRs (WC-SMRs) entwickelt und deren Einsatz in verschiedenen Ländern erwogen. Einige Konzepte verzichten dabei auf lösliches Bor im Kühlmittel. Dies bietet Vorteile wie einen verbesserten negativen Moderator-Temperaturkoeffizienten, reduzierte Korrosion sowie vereinfachte chemische Systeme, wodurch das Interesse an borfreien SMR-Konzepten (Soluble-Boron-Free, SBF-SMR) wächst.

Die Eliminierung von löslichem Bor stellt jedoch spezifische Herausforderungen für das Kerndesign und die Sicherheit dar. Da die verteilte Reaktivitätskontrolle durch Bor entfällt, muss die Kontrolle der Überschussreaktivität vollständig durch abbrennbare Gifte (Burnable Absorbers) und Kontrollstäbe erfolgen. Dies kann potenziell zu erhöhten lokalen Leistungsdichtefaktoren (Power Peaking Factors) führen. Aufgrund der kompakten Größe des SMR-Kerns ist eine sorgfältige Gestaltung der Core-Geometrie erforderlich, um die Sicherheitsparameter einzuhalten. Darüber hinaus kann der im Vergleich zu einem borierten SMR höhere Gesamtwert des Kontrollstabsystems in einem SBF-SMR zu einem übermäßig hohen Reaktivitätsbeitrag einzelner Stäbe führen, was im Falle eines hypothetischen Stabauswurfunfalls (Rod Ejection Accident, REA) die Kühlfähigkeit beeinträchtigen könnte.

Diese Dissertation begegnet diesen Herausforderungen durch die Entwicklung einer Methodik zur Optimierung des SBF-SMR-Kerns über den ersten und den Gleichgewichtskernzyklus. Ausgehend vom akademischen KSMR-Kerndesign, das sich bisher auf die Performance des frischen Brennstoffs zu Beginn des Zyklus konzentrierte, erweitert diese Arbeit die Untersuchung auf das Kernverhalten über den gesamten Abbrandzyklus. Der entwickelte SBF-SMR-Kern basiert auf ausgereifter Druckwasserreaktor-Technologie mit UO_2-Anreicherungen unter 5 % und Gd_2O_3 als Material für das abbrennbare Gift. Der Optimierungsprozess umfasst die Definition einer Reihe fester Parameter und Variablen (u. a. Brennstoffanreicherung, Konfiguration der Absorberstäbe und Gd_2O_3-Gehalt) und die anschließende systematische Exploration dieses großen Variablenraums zur Identifizierung optimaler Konfigurationen. Dabei kommt ein Zwei-Schritt-Ansatz zur Anwendung: CASMO5 generiert Wirkungsquerschnitte, und SIMULATE5 nutzt diese Daten für die Core-Simulationen. Zur Automatisierung der Eingabedatei-Generierung, Simulationsausführung und Ergebnisextraktion wurde ein in Golang entwickeltes Tool namens CoreOptimizer erstellt, was eine effiziente Kernoptimierung ermöglicht.

Abschließend werden die optimalen Kernkonfigurationen einer neutronischen und sicherheitstechnischen Bewertung über den ersten und den Gleichgewichtskernzyklus unterzogen. Dies stellt sicher, dass die angestrebte Zykluslänge erreicht wird und gleichzeitig alle Sicherheitskriterien eingehalten werden. Zusätzlich wurde ein hypothetischer Kontrollstabauswurfunfall simuliert, um die Sicherheitsperformance der optimierten Kerne unter Auslegungsstörfallbedingungen (Design-Basis Accident Conditions) zu validieren.

Publications related to this thesis

At first author in peer review journal papers

- Y.Song, Sánchez-Espinoza, V. (2025). Safety-related Investigations Designing a Soluble-boron-free Small Modular Reactor Core at Equilibrium. EPJ Nuclear Sci. Technol (Accepted). https://doi.org/10.1051/epjn/2025077.
- Y.Song, Sánchez-Espinoza, V. (2026). Optimizing Strategies to Improve the Safety Behavior during Rod Ejection Accident in a Soluble-Boron-Free SMR Core. (Under Review)

At first author in peer review conference papers

- Y. Song, G. Huaccho, L. Mercatali, Sánchez-Espinoza, V. H. (2024). Verification of the KSMR CASMO5/SIMULATE5 models against SERPENT and PARCS/SUBCHANFLOW. In *International Conference on Nuclear Fuel Cycle.* October, 2024. Tokyo, Japan.
- Y. Song, Sanchez-Espinoza, V. H. (2026). Neutron-physical and safety-related core design optimization of a soluble-boron-free small modular reactor . In S. X. Tan (Ed.), *Proceedings of the 32nd International Conference on Nuclear Engineering. 6.* Weihai, China. ICONE 2025. Springer Proceedings in Physics, vol 336. Springer, Singapore. https://doi.org/10.1007/978-981-95-3293-3_37.

Contents

List of Acronyms

Ag-In-Cd	Silver-Indium-Cadmium Alloys
AO	Axial Power Offset
ARI	All Control Rods Fully Inserted
ARO	All Control Rods Fully Withdrawn
BA	Burnable Absorber
B_4C	Boron Carbide
BOC	Beginning of Cycle
BWR	Boiling Water Reactor
CHF	Critical Heat Flux
CR	Control Rod
CR-A	Control Rod Layout A
CR-B	Control Rod Layout B
CRAM	Chebyshev Rational Approximation Method
CSDM	Cold Shutdown Margin
CVCS	Chemical And Volume Control System
CZP	Cold Zero Power
DiD	Defense-in-Depth
DNB	Departure from Nucleate Boiling
DNBR	Departure from Nucleate Boiling Ratio
EG	Energy Group
ENDF	Evaluated Nuclear Data File
ENR	Fuel Enrichment
EOC	End of Cycle
FA	Fuel Assembly
FTC	Fuel Temperature Coefficient

F_q	3D Peak Pin Power Factor
$F_{\Delta H}$	2D Peak Pin Power Factor
Gd_2O_3	Gadolinium Oxide
GUI	Graphic User Interface
HV	History Variables
HFP	Hot Full Power
HZP	Hot Zero Power
HTGR	High-Temperature Gas-Cooled Reactor
IAEA	International Atomic Energy Agency
JANIS	Java-Based Nuclear Data Information Software
k_{inf}	Infinite Multiplication Factor
k_{eff}	Effective Multiplication Factor
LHGR	Linear Heat Generation Rate
LMR	Liquid-Metal Reactor
LWR	Light Water Reactor
LOCA	Loss-of-Coolant Accident
MOC	Method of Characteristics
MSR	Molten Salt Reactor
MTC	Moderator Temperature Coefficient
NTE	Neutron Transport Equation
P_N	Spherical Harmonics Expansion
PRK	Point Reactor Kinetics
PWR	Pressurized Water Reactor
REA	Rod Ejection Accident
RPF	Axially-Averaged Radial Power
RPV	Reactor Pressure Vessel
SBF	Soluble Boron Free

S5	SIMULATE5
S5K	SIMULATE5-K
SCRAM	Emergency Reactor Shutdown
SMART	System-Integrated Modular Advanced Reactor
SMR	Small Modular Reactor
SN	Discrete Ordinates
SS	Stainless Steel
TH	Thermal-Hydraulics
WC-SMR	Water-Cooled Small Modular Reactor
β_{eff}	Effective Delayed Neutron Fraction
^{135}Xe	Xenon-135
^{149}Sm	Samarium-149
^{235}U	Uranium-235
^{238}U	Uranium-238

1 Introduction

The global energy landscape is undergoing a significant transformation, driven by the urgent need for sustainable, secure, stable and economically viable power sources. For decades, fossil fuels have dominated energy production, but their environmental impact, particularly their contribution to climate change through greenhouse gas emissions, has necessitated a shift in the energy production approach. Concurrently, geopolitical instabilities and the finite nature of fossil fuel reserves underscore the critical importance of energy security and diversification. In this complex scenario, nuclear power, as a low-carbon, high-density energy source, presents a compelling option for meeting burgeoning global energy demands.

However, the traditional model of large-scale nuclear power plants has historically faced many challenges. These include prohibitively high upfront capital investments (Lovering, et al., 2017), often running into billions of dollars (Gold, 2017) (BBC, 2019), which can strain national budgets and deter private investors. Construction periods typically extend over a decade or more, leading to the project delays and cost overruns due to unforeseen circumstances, regulatory changes, and interest accrual. Moreover, the stringent siting requirements for large reactors demand vast tracts of land, long construction timeline and robust grid infrastructure, thereby limiting their deployment options, particularly in densely populated or geographically constrained regions. These inherent weaknesses of traditional nuclear power plants are driving the need for the development of Small Modular Reactors (SMRs).

1.1 Features and Current Development Status of SMRs

Small Modular Reactors (SMRs) are a novel generation of nuclear reactors designed to generate electric power, typically up to 300 MWe (Wang, et al., 2024). Their defining characteristics are their smaller physical size and, crucially, their modular fabrication. Unlike traditional large reactors that are custom-built on-site, SMR components are designed to be manufactured in a controlled factory environment. These factory-built components are then transported as modules to various sites for assembly and installation as energy demand arises (Lloyd, et al., 2021). SMRs offer multiple advantages over traditional large-scale nuclear power plants, primarily in terms of economics, risk mitigation, security, deployment flexibility, and versatile multi-use e.g., for non-electric applications such as seawater desalination, district heating, industrial process heat and hydrogen production (Wang, et al., 2024).

Among others, SMRs have the following advantages:

- SMRs significantly reduce the initial capital cost. Their lower aggregate price makes it easier to secure funding from diverse sources and lessens the financial burden on project owners, positively impacting their credit ratings.

- Furthermore, SMRs promise reduced delivery time and construction risks. Their modular design and extensive factory fabrication are expected to shorten construction to 3-5 years, comparing to the 5-10 years for large power plants (Grossi, 2024). This certainty in delivery time and cost lowers accrued interest during construction, shortens investor equity hold periods, and accelerates revenue generation.
- Enhanced safety is another benefit. Many SMR designs incorporate integral reactor designs, where key components such as steam generators, reactor coolant pumps, pressurizer, and the entire reactor core are housed within a single reactor pressure vessel (RPV). This integral design drastically reduces external piping and connections, thereby eliminating the potential for loss-of-coolant accidents (LOCAs), which are design-basis accidents in conventional reactors. In addition, this enclosed unit inherently resists external threats, including terrorism, aircraft impacts, or vulnerabilities arising from natural phenomena. Furthermore, the ability to refuel SMRs in a factory environment and then transport the sealed unit back to the site significantly minimizes radiological risk to the environment and the public during fuel handling operations.
- Finally, SMRs provide deployment flexibility. They're ideal for isolated areas and remote communities where large plants are impractical due to limited energy demands or infrastructure. Their compact footprint allows for placement in industrial parks, military bases, or even as replacements for retiring fossil fuel plants, utilizing existing grid infrastructure and brown field sites to reduce land acquisition and transmission costs. Beyond electricity generation, SMRs are versatile for non-electric applications such as seawater desalination, district heating, industrial process heat and hydrogen production (Wang, et al., 2024).

Due to these benefits, the global SMR landscape is rapidly evolving. The acceleration is driven by supportive government policies, private investment, and international collaboration. According to the IAEA's Advanced Reactors Information System database, there are currently 70 designs at various stages of development and deployment worldwide, with a significant number of these already operational, under construction, or nearing deployment.

Currently, two SMR nuclear power plants are in commercial operation (IAEA, 2024), in addition to the test reactors.

- In the Russian Federation, the Akademik Lomonosov floating NPP, equipped with two 35 MWe KLT-40S reactors, has been supplying heat and power to Pevek in the Chukotka region since May 2020 and underwent its first refueling in 2023.
- In China, the demonstration HTR-PM at the Shidaowan site began commercial operation in December 2023, generating 200 MWe from two reactors linked to a single turbine.

Beyond these operational units, several SMRs are under construction.

- In Argentina, the CAREM-25 prototype reactor is progressing towards grid connection, targeted for 2028 (IAEA, 2024).
- China's ACP100 demonstration plant commenced construction in Hainan province in 2021. Its reactor core was installed in August 2023, with the multi-purpose PWR unit expected to generate 125 MWe by 2026 (IAEA, 2024).
- The Russian Federation began constructing the BREST-OD-300 reactor in June 2021 in Seversk. Major installation work started in 2024 with the placement of its 165-tonne steel reactor base plate. This pilot demonstration reactor is anticipated to become operational in 2026, generating 300MWe. Furthermore, the RITM-200 and ABV-6M have been constructed (Zverev, et al., 2013) (IAEA, 2012).
- In the USA, construction of Kairos Power's Hermes Low-Power Demonstration Reactor began in July 2024 in Oak Ridge, Tennessee. This fluoride salt-cooled, high-temperature reactor, the first non-light-water reactor in the USA in over 50 years to receive a construction license from the U.S. NRC, will demonstrate affordable heat production without generating electricity (IAEA, 2024).
- In the Republic of Korea, the system-integrated modular advanced reactor (SMART) has successfully obtained standard design approval and completed its construction design (IAEA, 2013).

These SMRs are categorized into different types, primarily based on the coolant material they use. Each type offers its own advantages, making it suitable for different applications (IAEA, 2024).

- Water-cooled reactors: These SMRs use light water as both coolant and neutron moderator. They often feature enhanced passive safety systems, relying on natural circulation for heat removal and offering extended coping times during incidents. It is the most common SMR type because it adopts the mature PWR technologies. Examples include China's ACPR50S and ACP-100 (under construction), Russia's VBER-300, SMART from South Korea, NuScale's Power Module from USA and Rolls-Royce SMR from UK.
- High-temperature gas-cooled reactors (HTGRs): HTGRs utilize inert gases, typically helium, as a coolant and graphite as a moderator. Operating at very high temperatures (above 700°C), HTGRs are highly efficient for electricity generation and uniquely suited for high-temperature industrial process heat applications, such as hydrogen production or synthetic fuel manufacturing, which are difficult to decarbonize otherwise. Furthermore, their coated-particle fuel design offers inherent safety advantages. Examples include China's HTR-PM (commercial use) and USA's Xe-100.
- Liquid-metal reactors (LMRs): LMRs employ liquid metals like sodium or lead as coolants, operating with fast neutron spectra. LMRs offer advantages in fuel efficiency and waste reduction by potentially burning long-lived radioactive waste of water-cooled reactors, important for the rational utilization of uranium resources. Besides, their high boiling points enable near-atmospheric

pressure operation, enhancing safety. Examples: China's CEFR (experimental reactor), USA's PRISM, Natrium and ARC-100.

- Molten salt reactors (MSRs): In MSRs, the nuclear fuel itself is dissolved in a molten salt coolant. This innovative design provides inherent safety (as the fuel can drain to a passive cooling system in an emergency), enables high-temperature operation for process heat, and allows for more efficient fuel utilization and waste management. Examples: TMSR-LF1 (China) (Liu, et al., 2020), Moltex SSR-W (UK), Integral MSR (Canada), Seaborg CMSR (Denmark), Hermes prototype (USA).

The global interest in water-cooled small modular reactors (WC-SMRs) is rapidly progressing from design to tangible deployment and international collaboration, marking a significant step towards their commercialization. These land-based, water-cooled SMRs typically utilize existing Light Water Reactor (LWR) fuel designs with ^{235}U enrichment below 5%. They are engineered for high operational availability and low operation and maintenance costs, benefiting from 18–24 month refueling cycles and an average burnup exceeding 45 GWd/tHM, with half the fuel assemblies typically replaced each cycle to optimize economics. Their similarity to existing large, water-cooled designs allows them to leverage established supply chains and regulatory familiarity, facilitating faster deployment. Therefore, several WC-SMR designs are poised for near-term deployment in various countries.

- China: WC-SMR deployment in China is actively advanced by various institutions and companies to address diverse energy needs, including heat, power generation and marine applications. For multi-purpose use, ACP100 has successfully completed its cold functional testing (NewNuclear, 2025). Concurrently, three pool-type WC-SMRs are being specifically promoted for district heating: DHR-400 (Wang, et al., 2022), HAPPY200 (Ning, et al., 2019) and NHR-200- II (Wang, et al., 2025). The floating nuclear power plant is another focus, including the ACPR50S, HHP25, and ACP100S (Qing, et al., 2020).
- USA: Numerous SMR developments are underway, including NuScale's VOYGR (six 77 MW(e) modules), which is shifting focus to new potential users and has garnered collaboration with Romania for a six-module power plant, financially backed by the U.S. Export-Import Bank. Westinghouse has submitted a pre-application for design certification of its AP300 SMR, and Holtec International is developing its SMR-300.
- UK: Rolls-Royce is developing a 470 MW(e) Rolls-Royce SMR. This design was recently selected by the Czech Republic for a small reactors project, with the first unit planned near the Temelin nuclear power plant in the 2030s.
- France: Actively promoting SMR development through France Relance 2030 funds, supporting the EDF-NUWARD SMR (a PWR) and nine other advanced designs such as NAAREA and Newcleo.
- Republic of Korea: Two key SMR designs are prominent: the 100 MW(e) SMART PWR, which received standard design approval in September 2024 and is pursuing licensing in Canada, while

also collaborating with Saudi Arabia on commercialization and design approval. The 170 MW(e) i-SMR, an integral PWR, is being developed by a national consortium.

- Russia: The RITM-200N is a notable water-cooled SMR poised for deployment.

1.2 Introduction to Soluble-Boron-Free WC-SMRs

1.2.1 Reactivity Control Mechanisms

In a typical WC-SMR, burnable absorbers (BAs), control rods (CRs) and soluble poison work interreacting to manage the reactivity and ensure the reactor safety.

Burnable absorber (BA)

BA are materials containing non-fissile nuclei with large neutron-absorption cross sections. The BAs are loaded into a nuclear reactor core at the beginning of cycle (BOC) and depleted over the operational cycle In a light-water reactor core, thermal neutrons are absorbed by fissile nuclei, initiating the fission reactor and generating fast neutrons within the fuel. After leaving the fuel, these neutrons enter the moderator where they are slowed down. The lower-energy neutrons are then scattered back into the fuel to be absorbed for initiating another fission reactions; However, some may be scattered into a burnable absorber material instead of the fuel. The BA is expected to compensate for excess reactivity effectively at BOC and fully consumed at EOC, such that the residual neutron absorption penalty is minimized.

The most common BA materials in commercial PWRs are boron and gadolinium (Evans, et al., 2022). Boron is typically implemented as boron carbide (B_4C), leveraging the high thermal neutron cross-section of ^{10}B, which is approximately 3850 barns. However, the (n,α) reaction ${}^{10}_{\square}B + n \rightarrow {}^{7}_{\square}Li + {}^{4}_{\square}He$ produces helium gas. Over time, helium accumulation may generate internal pressure that risks compromising fuel or cladding integrity. To mitigate this, boron is incorporated into separate components such as ZrB_2 coating or borosilicate glass (B_2O_3-SiO_2) (Galahom, 2017). In contrast, gadolinium is favored due to the high neutron cross section of its isotopes ^{155}Gd and ^{157}Gd. It is commonly used as gadolinium oxide (Gd_2O_3), homogeneously mixed within UO_2 fuel pellets to form UO_2-Gd_2O_3. A significant advantage of gadolinium is that its neutron absorption does not produce helium, thereby avoiding related pressurization issues. Besides boron and gadolinium, other materials are also used as BAs, including UO_2-Er_2O_3, Hafnium-based and Cadmium-based BAs.

Control rod (CR)

The control rods are typically made of materials that have large neutron absorption cross-sections. The control rods are attached to the control rod drive mechanisms located at the top of the reactor vessel. These mechanisms allow the precise control rod motion. Control rods are categorized into regulating banks and safety banks. The regulating banks are withdrawn or inserted slowly and precisely during the operation to

keep the core in a critical condition and flatten the radial power distribution. The safety banks are used during emergency situations for rapid shutdown so they are kept out of the core during normal operation. The typical types of control rods in a PWR are listed below and the neutron absorption cross sections of these CR materials are displayed in Figure 1.1.

- Silver-indium-cadmium alloys (Ag-In-Cd): It generally contains 80% Ag, 15% In and 5% Cd and is a common control rod material for PWRs (Bowsher, 1986). It has different energy absorption regions, good mechanical strength and can be easily fabricated. The primary isotopes in Ag-In-Cd alloy are ^{109}Ag, ^{107}Ag, ^{115}In and ^{113}Cd. As shown in Figure 1.1, all of them have high cross sections in the thermal range (around 0.025eV), confirming Ag-In-Cd as an effective neutron absorber in PWRs. In addition, multiple resonances across a wide energy range enable Ag-In-Cd to effectively absorb neutrons at intermediate energies, even before they are fully thermalized.
- Boron: Boron in its elemental form has unsuitable mechanical properties. Therefore, it is commonly used in the form of high-boron steel or B_4C. Figure 1.1 illustrates that ^{10}B has a wide neutron absorption spectrum. In the thermal neutron region, ^{10}B follows a near 1/v dependence.
- Stainless steel: The control rods containing stainless steel are also called grey rods (Myerscough, 1992) due to their smaller neutron absorption cross sections; they are made of steel without the other material inserted. The main constituents of stainless steel, including ^{52}Cr, ^{56}Fe and ^{58}Ni, show much smaller cross-sections across the thermal and lower energy ranges compared to other control rod isotopes in Figure 1.1.

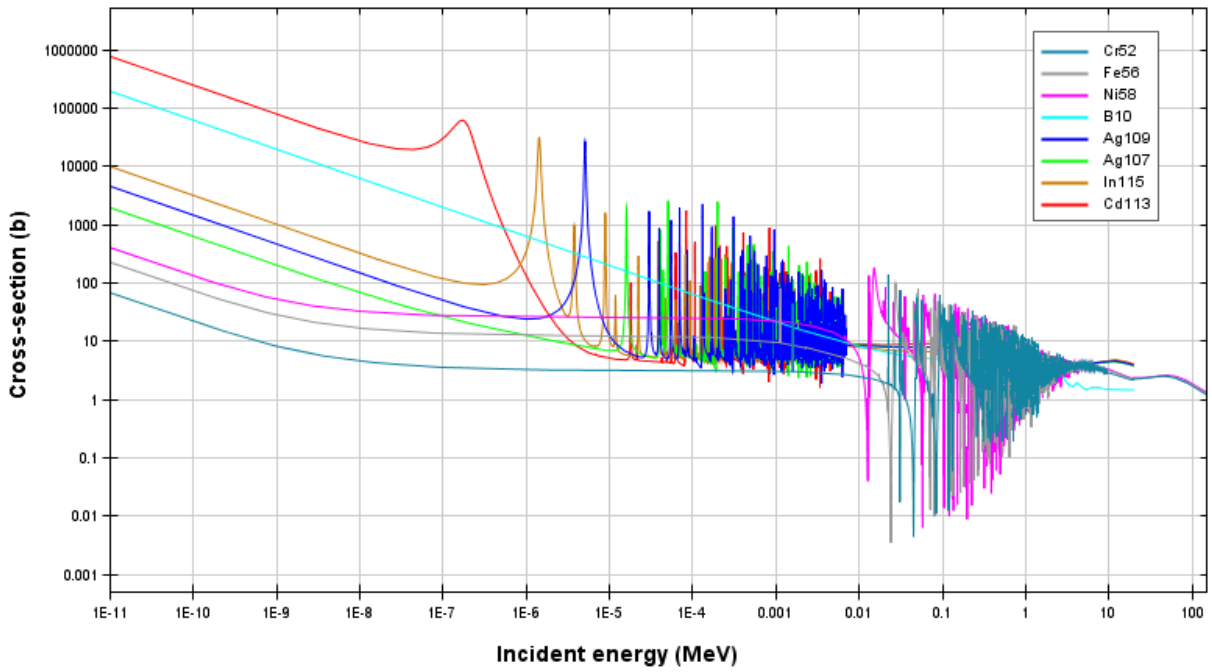

Figure 1.1 Energy dependence of the microscopic cross section of the isotopes of selected control rod materials. Source: JANIS (Java-based Nuclear Data Information Software); ENDF/B-VII.1

Soluble poison

Soluble poisons are dissolved in the coolant and produce a spatially uniform neutron absorption. The most common soluble poison in light-water reactor is boric acid, which is often referred to as soluble boron. The soluble boron decreases the thermal utilization factor, causing a decrease in reactivity. By varying the concentration of boric acid in the coolant, a process referred to as boration and dilution, the reactivity of the core can be easily managed. If the boron concentration is increased (boration), neutron absorption in the coolant increases, adding negative reactivity. If the boron concentration is reduced (dilution), less neutrons are absorbed adding positive reactivity. The changing of boron concentration is a slow process and control the reactivity for a long term. The fast injection of soluble poisons is often used as a redundant shutdown system in light-water reactors.

1.2.2 Benefits and Deployment of Soluble-Boron-Free Design

In typical light water reactors, BAs, CRs and soluble poison are reasonably interacted to manage the reactivity and ensure the reactor safety. However, the boron acid increases corrosion risks, as illustrated in a 2002 incident at Davis-Besse nuclear power plant (USGAOffice, 2006). In this event, a leak of borated water caused severe corrosion on the reactor pressure vessel head. The corrosive water ate through nearly 15 cm of carbon steel, leaving only a 1-cm-thick layer of stainless steel to contain the coolant. This near-catastrophe underscored the risks associated with boric acid and aroused the interest in SBF reactor designs.

The concept of a soluble-boron-free reactor is not entirely new to the nuclear community. Historically, the "Otto Hahn" ship, a nuclear-powered cargo vessel launched in 1968 (Halfinger and Haggerty, 2012), famously demonstrated this concept with a core operating at 38 MWth cooled by non-borated light water. This pioneering project proved the feasibility of operating a reactor without soluble boron for reactivity control. Similarly, in 1989, a comprehensive study by Combustion Engineering for the Electric Power Research Institute (EPRI) investigated the feasibility of eliminating soluble boron in large PWRs (EPRI, 1989). Their findings concluded that the feasibility of an SBF design significantly improves as the core power and size reduce, primarily due to the intrinsic xenon stability of smaller PWRs (Jo and Hah, 2020). During normal operation, the high-yield fission product iodine-135 decays to form the strong neutron absorber Xenon-135 (^{135}Xe). The concentration of ^{135}Xe can undergo spatial oscillation in large cores, leading to power distribution instabilities. Therefore, the SBF design is particularly well-suited for SMRs.

The advantages of SBF reactors are numerous and contribute significantly to their appeal:

- Improved operational stability and moderator temperature coefficient (MTC): The MTC describes how reactivity changes with moderator temperature: a negative MTC means that as moderator temperature increases, reactivity decreases. This provides an inherent negative feedback mechanism, contributing to reactor stability and safety, especially during power excursions. In boron-based WC-SMRs, the high concentration of soluble boron at beginning of cycle (BOC) has the risk of positive MTC (Mart J. , 2013). At BOC, when the coolant temperature rises, the water

density drops, leading to a decrease in the number density of boron atoms. Since boron is a neutron absorber, if this positive effect from reduced boron absorption outweighs the negative reactivity effect from decreased moderation due to lower water density, the overall MTC can become less negative or even positive. By eliminating boron, SBF designs consistently maintain a more negative MTC throughout the cycle.

- Reduced corrosion: Eliminating soluble boron from the primary coolant mitigates the risk of boric acid corrosion. Boric acid, especially at high temperatures and pressures and in areas of stagnant flow or crevices, can become corrosive to reactor pressure vessel (RPV) components, internal structures, and piping (Crane and Cullen, 2004). This corrosion can lead to material degradation, cracking, and the accumulation of corrosion products, which can become activated and contribute to radiation fields. By removing boron, the primary coolant chemistry is simplified, reducing the potential for such corrosion mechanisms, extending the lifespan of critical components, and consequently reducing maintenance requirements and associated costs.
- Less liquid waste: The absence of soluble boron reduces the volume of radioactive liquid waste generated. Ecomatrix discovered that 90% of tritium produced in a typical PWR primary-coolant results from the neutron activation with the soluble boron (Ecomatrix, 2009). Since tritium is known to be very mobile radioactive nuclide (IAEA, 1981), the radioactive liquid waste in decommissioning processes is reduced by eliminating the soluble boron from the primary coolant.
- Simplified system: In traditional PWRs, the Chemical and Volume Control System (CVCS) is a multi-component system responsible for maintaining coolant chemistry, controlling boron concentration, purifying the coolant, and managing coolant inventory. Its removal in SBF designs leads to a significant simplification of the overall reactor plant (Alam, et al., 2019). This simplification translates into a smaller plant footprint, reduced capital costs, fewer components to maintain, and lower operational complexity, all contributing to improved economics and reliability.

Driven by thesis advantages, academic and industrial entities worldwide are pursuing the development and deployment of various SBF SMR designs.

- RITM-400 (Russia) (TAGIROVA, 2025): The elimination of the CVCS in SBF SMRs significantly reduces system complexity, volume and weight, rendering them ideal for onboard applications. In Russia, onbeard SMR technology has evolved through multiple generations. Early operations relied on the OK-150 and OK-900 series, which are now largely decommissioned (Bukharin, 2006); followed by the KLT-40 family, which presently powers shallow-draft icebreakers and the floating power unit Akademik Lomonosov. Currently, the focus has shifted to the RITM series: the RITM-200 (175MW) is operational in the latest icebreaker fleet, while the high-capacity RITM-400 (315MW) is under development to support increased power demands. The RITM series incorporates hybrid active-passive safety systems capable of maintaining cooling for at least 72

hours during blackouts, alongside severe accident management features to retain core melt and limit radioactive releases.

- i-SMR (South Korea) (Kang, et al., 2024): This integral PWR, under development in South Korea, features a core of 69 fuel assemblies. Each is a 2.4-meter high, 17x17 square array of UO_2 (under 5% enrichment) mixed with gadolinia as the burnable poison. The refueling cycle is 24 months. An In-Vessel Control Element Drive Mechanism (IV-CEDM) eliminates control element ejection accidents, further boosting safety for this boron-free design. Beyond i-SMR, multiple conceptual SBF SMRs are also being actively explored by various research groups within South Korea. Several innovative BA designs are developed to decrease the reactivity swing while extending the cycle length. For example, studies by (Nguyen, et al., 2021) and (Yahya, et al., 2015) introduced conceptual BA designs to effectively suppress the reactivity swing across the long cycle. Similarly, (Kim D. , 2020) demonstrated that using the enriched gadolinia enabled a long-cycle operation with a discharge burnup of 21.8 GWD/MTU. Further advancing cycle length, (Kim and al, 2024) utilized Solid Pyrex to achieve a 4.8-year cycle length with excess reactivity below 5000 pcm. In addition, (Lee, et al., 2025) focused on the elevated risk of pellet-cladding interaction in SBF SMRs, demanding optimized fuel loading patterns to mitigate peak cladding stress.
- Rolls-Royce SMR (UK) (SMR, 2024): This SMR design avoids soluble boron for reactivity control during both power operations and shutdown. While it retains the functionality to inject boron in faulted situations following a scram failure, it is not used in normal operation. The core contains 121 fuel assemblies in 17x17 square lattices, with a 3.66-meter core height. The UO_2 fuel enrichment is less than 5%, and gadolinium serves as the burnable absorber. It operates on an 18-month (1.5-year) refueling cycle, with 44 fuel assemblies replaced per refueling.
- PRATIC (France): PRATIC is a conceptual design from France's CEA that explores a simplified, compact, and inherently safe soluble-boron-free SMR. (Serviere, 2023) (Vuiart, et al., 2024). The core contains 57 fuel assemblies, using various ^{235}U enrichments (2.5 wt% central, 3.5 wt% internal, and 5.0 wt% external) and varying numbers of burnable absorber rods (8, 28 and 36). It can reach a cycle length of 692EFPD (1.895 years) in a 2-batch equilibrium cycle.
- LDR-50 SMR (VTT, Finland): It is a 50MWth integrated PWR, developed by VTT since 2020 (Leppänen J. , et al., 2021) and commercialized by Steady Energy (Ikonen, et al., 2025). Designed for low-temperature district heating, it operates on natural circulation and is notably boron-free. The reactor incorporates in-vessel control rods, self-pressurization, and a passive decay heat removal system.

1.2.3 Challenges and Solutions in SBF Core Design

Despite the compelling advantages offered by soluble-boron-free designs, their implementation in SMR cores presents specific challenges compared to conventional boron-based cores. These challenges primarily

revolve around reactivity control, power distribution management, and ensuring adequate shutdown margins without the flexibility provided by soluble boron.

- Excess reactivity control and power distribution management. Without soluble boron for reactivity control, SBF cores inherently require a greater number of burnable absorbers (BAs) and control rods (CRs) to manage the excess reactivity present at the beginning of the fuel cycle and to compensate for fuel burnup over the cycle. However, relying solely on fixed BAs and movable CRs for reactivity management introduces complexities, particularly an increase in power distribution heterogeneity within the core: Radially, the smaller core size of SMR leads to a steeper power gradient; and axially, the local power peaks become strongly dependent on the specific placement and insertion depth of control rods due to the elimination of soluble boron. If not carefully managed, these higher local peak powers can result in a higher linear heat generation rate (LHGR) in individual fuel rods, which increases the risk of fuel rod failure, potentially exceeding thermal limits or inducing pellet-cladding interaction. Due to the limitations in available positions for control rods in a small-sized core, the compensation of excess reactivity and the maintenance of flat power distribution in a SBF SMR core is more challenging, requiring sophisticated core design and fuel management strategies.
- Safety Considerations. Any reactor core must be equipped with two independent and redundant shutdown systems. The primary system, which comprises the safety control rods, must be capable of shutting down the reactor under all anticipated operational occurrences. It must also include sufficient margin to accommodate potential malfunctions, such as a single stuck control rod. (U.S.NRC, 2021) In a SBF core, to ensure sufficient shutdown margin across all operational and design-basis accident states, the total control rod worth is significantly higher than in a boron-based core. This introduces a safety constraint: during a postulated rod ejection accident, the highest worth of the potentially ejected rod must be kept moderate. An excessively high worth for any individual control rod could result in a rapid power transient that challenges the core cooling capabilities.

Consequently, a larger number of BAs and CRs, along with a more complex and heterogeneous core design, must be applied for SBF reactor cores to satisfy all safety criteria during operation. These peculiarities pose significant challenges for the core design and optimization for SBF SMRs. To tackle these inherent challenges, several innovative strategies have been adopted in the state-of-the-art development of SBF SMR cores. Consequently, international developments are focus on the innovation of BA types, axial heterogeneous composition, and radial multiple zones across the core.

- Examples of these innovative BA types include the slow burnable absorber (Muth, 2016) design consists of inner and outer layers of Al_2O_3-B_4C, the centrally-shielded BA combined with disk-type BA (Nguyen, et al., 2021), or BA materials coated on the surface of control rod guide tubes (Yahya, et al., 2015) or on the outside of UO_2 pellets (Cho, et al., 2025). The goal of these innovative BA

designs is to ensure the BA depletion rate closely matches the fissile material depletion, thereby providing a flatter reactivity curve over the cycle and minimizing the need for control rod movement. While these designs have shown good neutronic performance, their mechanical properties, manufacturability, and overall safety still require further consideration before they can be deployed in commercial reactors.

- Regarding axial compositions, some designs utilize heterogeneous axial fuel assembly designs, featuring varying fuel enrichment and BA loading in different axial zones, to decrease the axial power shift (Lee D. , 2024) (Mart, et al., 2014) (Muth, 2016) (Alzaben Y. I., 2019).
- The multi-zones radial patterns have been adopted in many SBF SMR core designs. In general, the fresh fuel assemblies in both the fresh and equilibrium cores are radially divided into more than three zones to avoid the radial peak power. (Wang and al, 2021) (Muth, 2016)
- In addition, several other core design aspects have been explored in SBF SMR cores. To enhance the neutron moderation and fuel utilization, the pin pitch is increased to improve the hydrogen-to-uranium ratio (Nguyen, et al., 2021) (KEPCO and KHNP, 2014). Furthermore, the number of control rods within one fuel assembly is increased to enhance the CR worth (Vuiart, et al., 2024).

Furthermore, the core design and optimization process of a SBF SMR is a multi-objective problem, aiming to achieve:

- Sufficient cycle length: maximizing the time between fuel cycles for economic efficiency.
- Adequate safety margins during operation under critical condition: including acceptable Power peaking factors, power axial offset, negative moderator temperature coefficient, etc.
- Sufficient shutdown margin: guaranteeing the ability to shut down the reactor under all conditions with control rods.

The optimization requires advanced computational tools to identify optimal solutions that balance these conflicting objectives while strictly respecting safety criteria. In the previous PWR core design, several established software platforms have integrated multi-cycle core design capabilities and have been validated in PWR applications with high accuracy, such as TORCH V2.0 (Zhang, et al., 2022) and COCO (LU Hao-liang, 2017) developed in China, the APOLLO2 (Santamarina, et al., 2009) developed in France, and the ANC developed in USA (Westinghouse, 2013). Therefore, given the challenges associated with SBF SMR core design, the development of an in-house tool is proposed to automate the core design process and efficiently address the multi-objective problem.

1.2.4 Numerical Tools Application in SBF SMR Core Simulations

The global interest of SBF SMR concepts necessitates the evaluation of numerical core-physics tools. These codes, such as APOLLO3 (Vidal, et al., 2021), WIMS (Lindley, et al., 2017), DRAGON5 (Zain, et al.,

2021), SIMULATE5 (Tatsuya and Tomohiro, 2021), were originally developed and benchmarked for conventional large PWRs and BWRs.

The inherent differences in SBF SMRs, specifically the elimination of soluble boron and the core compactness, result in notable fluctuations in the core's neutron flux during normal cycle operation (R. Vuiart, 2024). These features may challenge the applicability and accuracy of the established numerical tools.

Consequently, validating and verifying these numerical tools for SBF SMR applications is important. For instance, modelling the PRATIC SMR using CASMO5/SIMULATE5 showed the discrepancies exceed 1000pcm at lattice level with control rod worth differences up to 2278 pcm at core level with inappropriate nuclear data compared to the APOLLO2/CRONOS2 scheme. At the core level, the control rod anti-reactivity showed a discrepancy up to 2278 pcm. Conversely, WIMS showed good agreement in k_{eff} values when verified against Monte-Carlo code SERPENT and hybrid MC code MONK for micro-heterogeneous duplex fuel (Alam, et al., 2020). Differences in k_{eff} were below 200 pcm using the same nuclear data file and around 450 pcm when different data files were employed. Therefore, the numerical core-physics codes need comprehensive assessment against high-fidelity codes and experimental data to confirm their simulating accuracy in SBF SMR cores.

1.2.5 Brief Description of the Objective Core

This section provides an overview of the objective SBF-SMR core, which builds on the academic KSMR-core design (Alzaben Y. I., 2019). It outlines the core's key geometric parameters, operational conditions, assembly configurations as well as the reflector design. The objective core maintains several reference specifications while introducing several modifications to align with commercial PWR technology.

1.2.5.1 Geometrical Data and Operational Conditions

The core design builds upon the academic KSMR core model (Alzaben Y. I., 2019), which consists of 57 fuel assemblies (Figure 1.2) with an active core height of 2 meters. Certain geometric parameters and operating conditions from (Alzaben Y. I., 2019) are applied for this investigation, as summarized in Table 1-1. The pin types and physical parameters of the fuel assembly are summarized in Table 1-2.

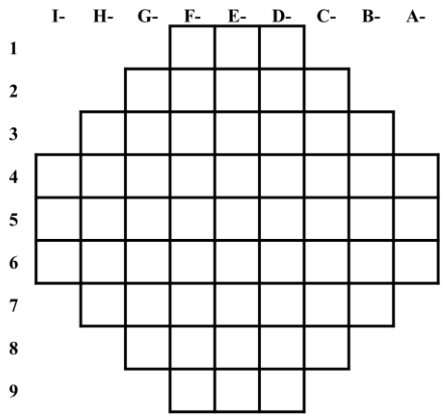

Figure 1.2 Schematic radial representation of 57 fuel assemblies in the core

Table 1-1 Geometrical data and operation conditions of the 3D core model

Fuel assembly parameters	**values**
Pin pitch	1.26 cm
FA pitch	21.504 cm
Active height	200 cm
Spacer grids number	5
Spacer grids material	Inconel-718
Operating conditions	**values**
Batch number	2
Thermal power	330 MW
Core coolant flow rate	2006.4 kg/s
Pressure at core outlet	15.0 MPa
Coolant temperature at the core inlet	296 ℃

Table 1-2 Pin types and physical parameters of the fuel assembly

Pin types	**Section view of rods**	**Regions**	**Structures**	**Materials**	**Density (g/cm^3)**	**Diameters (cm)**
Fuel Pin	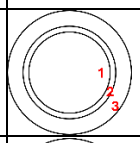	1	Fuel pellet	UO_2	10.4	0.78436
		2	Filled gas in gap	Helium	0.0016	0.80010
		3	Cladding	Zircaloy-4	6.55	0.91440
BA Pin	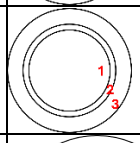	1	Fuel pellet	UO_2-Gd_2O_3	10.4	0.78436
		2	Filled gas in gap	Helium	0.0016	0.80010
		3	Cladding	Zircaloy-4	6.55	0.91440
CR guide tube/ IT tube	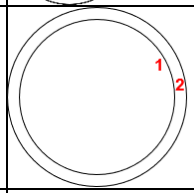	1	moderator	water	Depends on the state	1.12268
		2	Cladding	Zircaloy-4	6.55	1.20396
CR pin	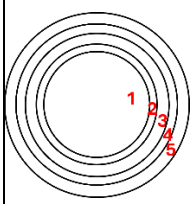	1	Neutron absorption materials	Stainless steel	8.03	0.86620
				Ag-In-Cd	10.16	
		2	Filled gas in gap	Air	0.000616	0.87376
		3	Support structure	Stainless steel	8.03	0.96774
		4	moderator	water	Depends on the state	1.12268
		5	Cladding	Zircaloy-4	6.55	1.20396

1.2.5.2 Fuel Assembly Configurations

Consistent with the reference KSMR core (Alzaben Y. I., 2019) , each FA adopts a 17×17 rod array, comprising 289 positions allocated to fuel rods, burnable absorber (BA) rods, an instrumentation thimble, and 25 control rod guide tubes. The fuel rods are loaded with UO_2 pellets enriched to less than 5 wt% ^{235}U.

Different from the reference core's heterogeneous axial zoning, the fuel assemblies in this investigation are modeled as axially homogeneous to enhance manufacturability. Additionally, whereas the reference core utilizes a double-layered academic BA design, this investigation adopts gadolinium oxide (Gd_2O_3) as the BA material because Gd_2O_3 is a commercial BA material with mature industrial applications. The Gd_2O_3 is incorporated with a Gd loading below 10 wt%.

Control Rods Configurations in Fuel Assemblies

Specific positions within each FA are reserved for control rod insertion, see Figure 1.3. When control rods are fully withdrawn, these guide tubes are flooded with water. The control system is divided into regulating banks and safety banks. Regulating banks manage fine reactivity control and radial power shaping during operation, whereas safety banks, fully withdrawn under normal conditions, are designated for rapid reactor shutdown in emergencies.

In the typical UOX fuel assembly used in a light-water SMR, all 24 guide tubes per assembly are used for Ag-In-Cd rods insertion. However, in the soluble-boron-free core, the limitation of highest control rod worth is important, which is driven by two factors: First, the axial power shape is strongly dependent on control rod positions; Second, to avoid prompt supercriticality in hypothetical REA accident. Therefore, the fuel assembly design adopted a hybrid regulating bank configuration inspired by AP1000 technology (Company, 2011), incorporating both 12 Ag-In-Cd rods and 12 stainless steel (SS) rods, as illustrated in Figure 1.3. Stainless steel has a lower absorption cross-section than Ag-In-Cd, which helps to reduce the overall control rod worth in one assembly. To ensure sufficient shutdown capability despite reducing the regulating bank worth, the safety banks maintained the configuration with 24 Ag-In-Cd rods. Due to the overall control rod worth decrease in the core, the core shutdown capability should be investigated.

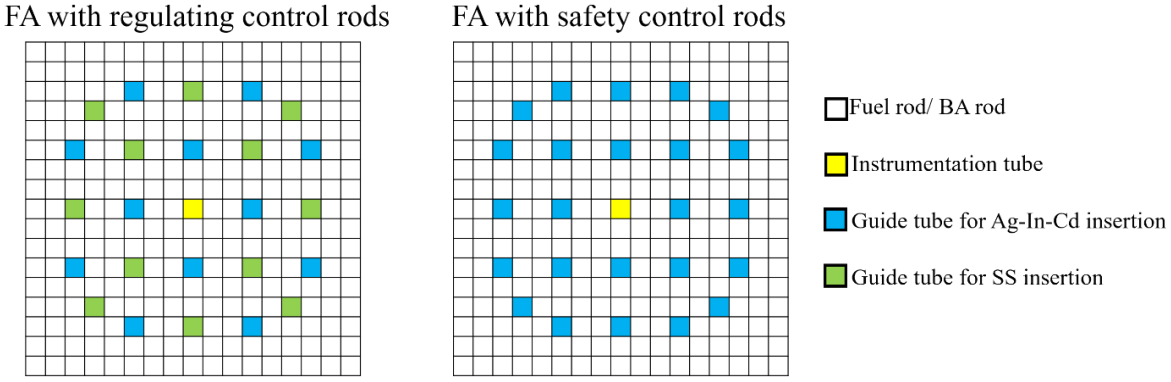

Figure 1.3 Control rod guide tubes in one fuel assembly

Burnable Absorber Configurations in Fuel Assemblies

For a SBF core, achieving an optimal BA burnout rate throughout the cycle is important, which necessitates a careful balance between the fuel enrichment and the total BA loading per assembly. The total BA loading is governed by both the BA-rod number per FA and Gd_2O_3 concentration within the BA rods. Typically, the Gd_2O_3 concentration of FAs in PWR is maintained below 10% by weight (Durazzo and Riella, 2008). In this investigation, various BA rod number per FA are applied for selection, they range from 12 to 40, with an increment of 4. These specific configurations are adapted from studies in (Alzaben Y. I., 2019) (Muth, 2016) and the radial layouts corresponding to these configurations are detailed in Figure 1.4. The optimized BA rod number will be determined during the core design and optimization process.

Figure 1.4 Radial arrangements of the FAs with various BA rods

1.2.5.3 Reflectors

Reflectors are the materials surrounding the active core axially and radially, reflecting the neutrons back into the active fuel region.

Axial Reflectors

The axial reflectors are positioned at the top and bottom of the core. The materials and thickness of axial reflectors are detailed in (Alzaben Y. I., 2019) and they are summarized in Table 1-3.

Table 1-3 Materials and thickness of axial reflectors

	Materials	Thickness (cm)	Description
Top reflector	Water	20.00	Coolant
	SS-304	8.83	Upper nozzle
	Water	3.35	Coolant
	Zircaloy-4 and Inconel-718	6.80	End plug and spacer grid
Bottom reflector	Zircaloy-4 and Inconel-718	5.55	Bottom of fuel rod and spacer gird
	SS-304	15.16	Support plate and lower nozzle
	Water	20.00	Coolant

Radial Reflectors

The radial reflector is a structure installed inside a core barrel. Due to the relatively large neutron leakage effects in SMR cores, a heavy reflector (P. Suk, 2021) is employed radially, which consists of a thick wall of stainless steel, see Figure 1.5. Compared to typical radial reflectors, this heavy reflector has a higher atomic number density, which more efficiently reduces neutron leakage, especially for high-energy neutrons. Given its effectiveness, a heavy reflector made of stainless steel with a thickness of 25 cm is used in this core. The model of radial reflectors in SIMULATE5 is displayed in Figure 1.6.

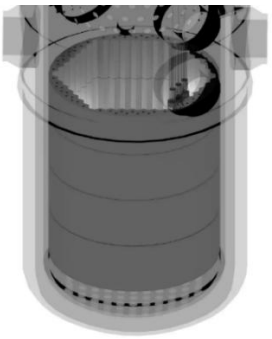

Figure 1.5 An illustrative example of a heavy reflector (power, n.d.)

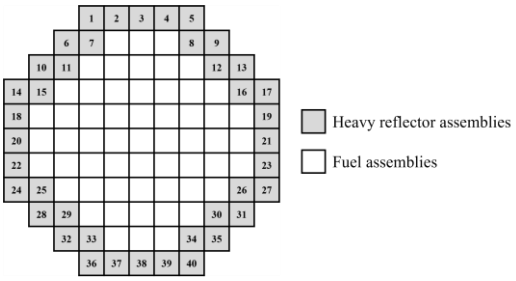

Figure 1.6 Model of radial reflector assemblies in SIMULATE5

1.3 Goals of the Thesis

As described in the preceding discussion, the SBF SMR core design presents several challenges that necessitate careful analysis. The absence of soluble boron, combined with a compact core geometry, leads to steeper power gradients and increased power peaking risk, thereby challenging safety limits. Additionally, the control rod design must achieve a balance between sufficient shutdown margin and acceptable reactivity worth in single assembly. These characteristics underscore the need for reliable numerical tools, which must be assessed before being applied to the specific SBF SMR core.

The study builds on the academic KSMR-core design (Alzaben Y. I., 2019). While previous investigations successfully explored the neutronic performance of fresh KSMR core at beginning of cycle (BOC), the continuous processes of fuel burnup, subsequent refueling strategies and equilibrium states were neglected, which are integral to a reactor's life cycle. The lack of investigation into these long-term features represents a disconnect between current theoretical design and the demands of sustained reactor operation.

In light of these challenges and the identified research gaps, the thesis aims to achieve the following research tasks:

- Simulation Tools Assessment: Assess the core simulation tools CASMO5/SIMULATE5 against a Monte-Carlo code for their application to this specific SBF SMR core design.
- Determination of Core Design Constraints: Define and fix the key physical and operating constraints for the core design process. This task utilizes the established rod, assembly and core dimensions and operating conditions of the academic KSMR-core design (Alzaben Y. I., 2019), leveraging mature PWR technology with UO_2 fuel (enrichment <5%), and Gd_2O_3 as the burnable material (loading $\leqslant$ 10%).
- Identification of Optimization Variables: Based on the largely-fixed core architecture, define the key parameters to be optimized.
- Development of a Core Design Tool: Since the design optimization of an SBF-SMR-core regarding safety criteria and optimal use of resources is a complex, iterative process with a large number of free parameters, the development of a versatile and efficient informatic tool is necessary to overcame the tedious and repetitive manual effort to perform the thousands of simulations using CASMO5 and SIMULATE5 considering parameter combinations. In addition, the preparation of the inputs for a large number of cases, the running of the tools and the extraction of meaningful data from the large output files needs automation using programming languages like Python, Golang, or Perl.
- First-Cycle Core Design and Optimization: Design and optimize the startup core loaded with all fresh fuel assemblies. The optimization goal is to achieve the target cycle length of 2 years while satisfying all requisite safety criteria throughout the cycle.
- Equilibrium-Cycle Core Design and Optimization: Develop a multi-batch refueling strategy that transitions the core from the first operating cycle to the equilibrium cycle. This task involves accurately modelling the core's long-term operational behaviour, with the resulting equilibrium core design reaching the 2-year target cycle length and compliance with all safety criteria.
- Comprehensive Core Performance Evaluation: Perform a comparative analysis of the first and equilibrium cycles. This includes a thorough evaluation of both neutronics physics and safety parameters for the designed SBF-SMR-core.
- Transient Accident Analysis: Conduct a design basis accident, such as rod ejection accident (REA) in the designed first-cycle and equilibrium-cycle SBF-SMR-core. This task will investigate the power surge, the associated reactivity coefficient feedback mechanisms, and other reactor physics parameters during REA. The results will be compared against REA safety limits to evaluate the maintenance of fuel cladding integrity and the core cooling capability, thereby demonstrating the inherent safety features within the optimized cores.

To achieve these technical goals, the dissertation is organized as follows:

- Chapter 2 outlines the theoretical background for core design, covering neutronics, thermal hydraulics, reactor dynamics and reactor safety principles.
- Chapter 3 introduces the related simulation tools and their assessment to ensure their accuracy and reliability in simulating the specific SBF SMR core.
- The core design methodology is detailed in Chapter 4, including the definition of design constraints, the identification of optimization variables, the development of an automated core design tool and the implementation of a multi-stage variable search process.
- The main features of the optimized first-cycle and equilibrium-cycle cores are described and discussed in Chapter 5, with emphasis on their neutronic and safety performance throughout their cycles.
- In Chapter 6, a hypothetical rod ejection accident is investigated for the optimized core designs. The analysis focuses on a comparative evaluation of core behaviour and key safety parameters.

2 Theoretical Background

The comprehensive investigation into reactor core design relies on the theoretical background, which this chapter will detail in five interconnected aspects.

Firstly, the neutron transport equation (NTE) is introduced as the framework for neutron flux distribution and its numerical solutions are briefly reviewed. Detailed derivations of the multi-group spherical harmonics method and diffusion method are provided because they establish the theoretical foundations for the lattice and full-core simulations in this study. Secondly, the time-dependent multi-group diffusion equations are derived and the simplified point reactor kinetics (PRK) model are introduced to analyse core transients. Subsequently, the burnup equations and fuel management strategies in SMRs are explored to address the long-term evolution of core properties. As the core design involves coupled multi-physics, this section incorporates heat transfer principles and definitions of thermal-hydraulics safety limits. Finally, the chapter concludes the relevant safety considerations in core design process, including the safety criteria under normal operating condition and cold shutdown margin with single failure.

2.1 Neutron Transport Equation and Numerical Solutions

This section presents the Neutron Transport Equation (NTE) as the mathematical framework for determining neutron flux distribution within a reactor core. The numerical solutions for NTE are briefly reviewed, contrasting deterministic and stochastic methods. Subsequently, the governing equations of the P_N method are derived in detail because of their application in the lattice physics code adopted in this work. Furthermore, this section deduces the steady-state multi-group diffusion equation from the P_N transport

equations, thereby defining the theoretical foundation for the full-core simulation code employed in this study.

2.1.1 Neutron Transport Equation

NTE describes neutron transport in space, all possible interactions with materials, and neutron production from sources. Solving the NTE yields the neutron distribution in position, energy, and direction, enabling precise determination of key parameters in reactor core design, such as power distribution.

The general form of the NTE describes the angular neutron flux. It accounts for the time rate of change, leakage, collision losses, and source terms. The equation is displayed in (2.1) (Bell and Glasstone, 1970).

$$\frac{1}{v}\cdot\frac{\partial\psi}{\partial t}+\boldsymbol{\Omega}\cdot\nabla\psi+\Sigma_t\psi=\iint\Sigma_s(\boldsymbol{r},E'\to E,\boldsymbol{\Omega}'\to\boldsymbol{\Omega})\psi' dE' d\boldsymbol{\Omega}'+Q(\boldsymbol{r},\boldsymbol{\Omega},E,t) \tag{2.1}$$

Where:

- $\psi=v\cdot N\equiv\psi(\boldsymbol{r},\boldsymbol{\Omega},E,t)$ and $N(\boldsymbol{r},\boldsymbol{E},\Omega,t)$ is the neutron density at position $\boldsymbol{r}$, with energy E, traveling in direction $\boldsymbol{\Omega}$ at time t. ψ is the angular neutron flux, which is the angular neutron density divided by the neutron speed.
- v is the neutron speed.
- $\frac{1}{v}\cdot\frac{\partial\psi}{\partial t}$ represents the time rate of change of the neutron density.
- Σ_t is the macroscopic total cross-section, representing the overall probability that neutrons will interact with all nucleus in the volume.
- $\boldsymbol{\Omega}\cdot\nabla\psi$ represents the neutron leakage out of the volume
- $\Sigma_s(\boldsymbol{r},E'\to E,\boldsymbol{\Omega}'\to\boldsymbol{\Omega})$ is the scattering cross-section, describing the probability of a neutron scattering from energy E' and direction $\boldsymbol{\Omega}'$ to energy E and direction $\boldsymbol{\Omega}$.
- $Q(\boldsymbol{r},\boldsymbol{\Omega},E,t)$ is the source term, including the neutrons generated by fission and external source term. The external source term is neglected in this study.

Solving the NTE presents a significant computational challenge. The NTE is inherently complex due to its high dimensionality, involving seven independent variables: three for spatial coordinates, one for energy, two for angular direction, and one for time. Furthermore, its integro-differential nature adds another layer of difficulty.

Given these complexities, a range of numerical methods have been developed to make these calculations feasible. Broadly, two primary numerical approaches are employed to tackle these challenges: deterministic methods and stochastic methods.

2.1.2 Deterministic Method

Deterministic methods solve a discretized version of the NTE by approximating its continuous variables—space, angle and energy—onto a discrete mesh or through basis function expansions. Angular variables are discretized using methods such as discrete ordinates or spherical harmonics. Spatially, the domain is divided into cells, commonly employing finite difference, finite element, or nodal methods. Energy is typically handled by dividing the continuous domain into energy groups (multigroup approximation). Within each group g, all neutrons are assumed to have representative average properties.

Several approximation methods are applied within the deterministic framework: Method of Characteristics (MOC), Spherical Harmonics Expansion (P_N) and Discrete Ordinates (S_N).

- The MOC method deterministically solves the neutron transport equation by tracking particle propagation along discrete characteristic lines. While geometrically flexible, its accuracy depends on tracking density, and its iterative nature often leads to slow convergence, requiring effective acceleration techniques (Eklund, et al., 2015). Nowadays, the advancements in parallel computing enabling efficient and accurate MOC solutions. Numerous codes leverage MOC for reactor analysis. AGENT enables 2D/3D whole-core neutron transport with flexible geometry modelling (Hernandez, et al., 2013). APOLLO2 and its variant APOLLO2.8 incorporate MOC modules for assembly and core calculations, demonstrating high accuracy in LWR applications (Moreau, et al., 2004). CASMO5 and CRX are other well-established codes applied in rectangular and hexagonal geometries (Ferrer and Rhodes, 2014) (Hong and Cho, 1998).
- P_N method involves expanding the angular neutron flux in a series of Legendre polynomials up to order N (Fletcher, 1983). This expansion converts the integro-differential NTE into a coupled set of differential equations for the Legendre coefficients, which represent moments of the flux. The lowest order approximation, P_1, with further simplifying assumptions, leads to the well-known diffusion equation. While the diffusion equation is significantly simpler to solve, it is less accurate than higher-order transport approximations. It generally provides adequate results for large, weakly absorbing regions but often fails near strong absorbers, system boundaries, or in highly heterogeneous systems. Higher-order P_N methods improve accuracy but at the cost of increased computational complexity. Several reactor physics codes implement the P_N method. SIMULATE5 supports both the diffusion and P_3 transport solutions for core simulation (Bahadir and Grandi, 2021). PARAFISH employs the P_N method with finite elements and has been validated in 3D steady-state Takeda benchmark, showing good agreement in k_{eff} values with Monte-Carlo reference (Duran-Gonzalez, et al., 2022). EVENT offers both diffusion and higher-order P_N solutions, benchmarked against Monte-Carlo results (Ziver, et al., 2005). DIF3D-VARIANT incorporates P_N capability within a nodal framework (Smith, 2022).

- The S_N method discretizes angular, spatial, and energy variables in particle transport equations, converting them into linear systems solved via source iteration. Angular quadrature order N defines discrete directions and weights (Yu, et al., 2025). Variable independence enables flexible discretization and high computational efficiency, especially in deep-penetration problems. Representative codes include TORT, which shows high accuracy in 3D C5G7-MOX benchmarks (Seubert, et al., 2006) and DENOVO, which achieves strong scaling via parallel computing and multigrid pre-conditioning (Slaybaugh, et al., 2013) (Evans, et al., 2010). AMTRAN also demonstrates high parallel efficiency (Compton and Clouse, 2005).

Steady-State Multi-Group P_N Equation

Among these deterministic methods, the one used in this study in CASMO5 is the P_N method. Derived from NTE (2.1), for the steady state, $\frac{\partial \psi}{\partial t} = 0$. Assume the system changes only in one direction x and has the azimuthal symmetry, $\nabla\psi$ can be simplified to $\mu\frac{\partial \psi}{\partial x}$, where $\mu = cos\theta$. With these assumptions, the NTE (2.1) can be expressed in (2.2).

$$\mu\frac{\partial \psi(x,\mu,E)}{\partial x} + \Sigma_t(x,E)\psi(x,\mu,E) = \iint \Sigma_s(x,E' \to E, \boldsymbol{\Omega}' \to \boldsymbol{\Omega})\psi' dE' d\boldsymbol{\Omega}' + Q(x,\mu,E) \tag{2.2}$$

Using the P_N approximation (2.3),

$$\psi(x,\mu,E) = \sum_{m=0}^{\infty} \frac{2m+1}{2}\phi_m(x,E)P_m(\mu) \tag{2.3}$$

Where ϕ_n is the Legendre moments of the neutron flux. Multiply both sides of the equation by $P_n(\mu)$ and integrate over μ from -1 to 1, (2.4) is obtained.

$$\begin{aligned}\int_{-1}^{1} P_n(\mu)\left(\mu\frac{\partial \psi}{\partial x}\right)d\mu + \int_{-1}^{1} P_n(\mu)\Sigma_t(x,E)\psi d\mu \\ = \int_0^{\infty} \Sigma_{s,n}(x,E' \to E)\psi' dE' + \int_{-1}^{1} P_n(\mu)Q(x,\mu,E)d\mu\end{aligned} \tag{2.4}$$

Using the recurrence relation for Legendre polynomials (2.5) and applying the orthogonality property of Legendre polynomials (2.6), and multiplying both sides by $(2n+1)$, the equation can be transformed into (2.7).

$$(2n+1)\mu P_n(\mu) = (n+1)P_{n+1}(\mu) + nP_{n-1}(\mu) \tag{2.5}$$

$$\int_{-1}^{1} P_k(\mu)P_l(\mu)d\mu = \begin{cases} 0 & if\ k \neq l \\ \dfrac{2}{2k+1} & if\ k = l \end{cases} \tag{2.6}$$

$$(n+1)\frac{\partial \phi_{n+1}}{\partial x} + n\frac{\partial \phi_{n-1}}{\partial x} + (2n+1)\Sigma_t(E)\phi_n = (2n+1)\int \Sigma_{s,n}(E' \to E)\phi_n(E')dE' + (2n+1)Q_n(E) \quad (2.7)$$

By integrating the continuous-energy equation (2.7) over each energy interval $E \in [E_{g-1}, E_g]$, the multi-group neutron transport equation (2.8) is obtained. This is the basic equation will be solved in CASMO5.

$$(n+1)\frac{d\phi_{n+1,g}(x)}{dx} + n\frac{d\phi_{n-1,g}(x)}{dx} + (2n+1)\sigma_{n.g}(x)\phi_{n,g}(x) = (2n+1)\sum_{g'=1}^{G}\sigma_{n,g'\to g}(x)\phi_{n,g'}(x) + (2n+1)Q_{n,g}(x) \quad (2.8)$$
$$n = 0,1,2,\dots,N;\ g = ,1,2,\dots,G$$

Where:

- n is the order of the Legendre polynomial expansion
- g is the group index
- $\phi_{n,g}$ is the *n-th* order group flux expansion coefficient
- $\sigma_{n.g}$ is the *n-th* order total group cross section
- $\sigma_{n,g'\to g}$ is the *n-th* order transfer group cross section
- $Q_{n,g}$ is the *n-th* order source moment of the neutron source

2.1.3 Stochastic Method

The stochastic method, more commonly known as the Monte Carlo method, simulates physical processes through statistical sampling. This approach involves launching a large number of virtual neutrons within a core and meticulously tracking the path of each individual neutron. As a neutron interacts with a nucleus, the probabilities of absorption, scattering, or fission are determined based on relevant cross-sections. By simulating the behaviour of a vast number of neutrons, comprehensive statistical information about various parameters can be obtained. While Monte Carlo codes inherently provide uncertainty quantification through their statistical nature, they are particularly adept at handling complex core geometries and material properties without requiring any approximations. The representative codes are MCNP (Thomas E. Booth, 2003), OpenMC (Romano, 2015) and Serpent (Leppänen J. , 2015).

The Monte Carlo simulation process can be broken down into several key steps:

- The simulation begins with neutron birth, where neutrons are "launched" from a defined source distribution. This source could be, for instance, fission sites from a previous generation of neutrons or a specified external source. The initial position, energy, and direction of these newly "born" neutrons are all sampled from appropriate probability distributions.

- Next, each neutron is tracked as it moves through the simulated geometry. The distance to its next potential collision is determined by sampling from an exponential distribution, which is itself governed by the total macroscopic cross-section of the material it's traversing.
- Upon a collision, the type of interaction that occurs is probabilistically determined. This determination is based on the relative values of the microscopic cross-sections of the target nuclide at the neutron's current energy.
- If a neutron encounters a boundary, its fate depends on the defined boundary condition. For example, a vacuum boundary means the neutron leaks out of the system, ending its history, whereas a reflective boundary would cause it to be reflected back into the system.
- Throughout their journey and interactions, various quantities of interest, known as tallies, are meticulously recorded. Finally, by simulating an extremely large number of neutron histories (often ranging from millions to billions) statistical averaging allows for the generation of statistically meaningful estimates of the desired quantities.

Deterministic method is suitable for scenarios demanding detailed flux solutions across the entire phase space, or for problems characterized by relatively simple geometries and moderate transport effects. Once converged, deterministic methods provide a complete solution, detailing the flux distribution everywhere. However, a drawback of deterministic methods is that they introduce approximations regarding space, position, and angle, which can negatively impact accuracy. In contrast, stochastic methods excel at handling extremely complex 3D geometries and material compositions with virtually no geometric approximations. They also have the advantage of being able to utilize continuous-energy cross-section data, thereby avoiding the need for multigroup approximations and their associated errors. The primary disadvantage of Monte Carlo simulations, is their significant computational expense and time consumption, especially in depletion simulations.

To best utilize the strengths of both deterministic and stochastic methods, deterministic method is preferred for long-term core depletion simulations. Furthermore, it is advisable to compare the results from deterministic codes with those obtained from stochastic methods to verify their accuracy for the specific geometries and conditions under consideration.

2.1.4 Steady-State Multi-Group Diffusion Equation

In the nuclear industry, the NTE is typically reserved for assembly-level lattice simulations rather than full-core simulations. This is primarily due to the computational burden associated with the high-dimensional phase space inherent in the direct solution of NTE.

For instance, employing a P_3 approximation for a one-dimensional problem in equation (2.8) necessitates the resolution of four distinct angular moments $(\phi_0, \phi_1, \phi_2, \phi_3)$ for each energy group and spatial mesh grid. The extension of this formulation to three-dimensional geometries results in an exponential escalation

of the required moments. Moreover, the system exhibits stiff coupling where the derivation of $\phi_{n,g}$ in (2.8) depends on both $\phi_{n+1,g}$ and $\phi_{n-1,g}$, leading to inherently slow numerical convergence. Therefore, the use of full-core pin-resolved neutron transport methods to model the reactor requires significant additional computational resources (Gunow, 2018) (Santandrea, et al., 2018), leading to the diffusion method a typical approach adopted for full-core analysis.

To balance computational speed with accuracy, this study employs the industry-standard "two-step" approach. In this scheme, a lattice code first performs transport calculations at the lattice level using P_N method; The discrepancies inherent in the diffusion equation are calculated by the lattice code and passed to the core simulator as correction factors.

The core simulation relies on neutron diffusion theory, which can be regarded as being equivalent to the P_1 equation (Bell and Glasstone, 1970). The Fick's Law is introduced, which postulates a relation between the neutron current density and the flux gradient, as expressed in (2.9).

$$\boldsymbol{J}_g(x) = -D_g(x)\nabla\phi_g(x) \tag{2.9}$$

Where:

- $D_g(x)$ is the diffusion coefficient for group g
- ϕ_g is the scalar neutron flux of energy group g

By substituting Fick's Law, the equation (2.8) can be transformed into a system of second-order partial differential equation. The multi-group diffusion equation is presented in (2.10), which is a Laplacian operator problem.

$$\begin{aligned} -\nabla\cdot(D_g(x)\nabla\phi_g(x)) + \Sigma_{t,g}(x)\phi_g(x) \\ = \sum_{g'=1}^{G}\Sigma_{s,g'\to g}(x)\phi_{g'}(x) + \frac{1}{k_{eff}}\sum_{g'=1}^{G}\nu\Sigma_{f,g'\to g}(x)\phi_{g'}(x) \end{aligned} \tag{2.10}$$

Where:

- $\Sigma_{s,g'\to g}$ is the macroscopic scattering transfer cross-section of neutrons from group g' to g.
- k_{eff} is the effective multiplication factor
- ν is the fission yield, which is the number of neutrons released per fission event
- $\Sigma_{f,g'\to g}$ is the fission production macroscopic cross-section, representing the probability of fission in group g' producing a neutron that appears in group g

2.2 Reactor Kinetics

Focusing on the time-dependent behaviour of the reactor, this section derives the time-dependent multi-group diffusion equations and the simplified point reactor kinetics (PRK) model to analyse core transients

while discussing advanced numerical techniques to resolve the stiffness inherent in kinetic differential PRK equations.

2.2.1 Time-Dependent Multi-Group Diffusion Equation

Nuclear fission produces neutrons through two primary mechanisms:

- Prompt neutrons: A significant portion of neutrons are emitted instantaneously ($< 10^{-14}\ seconds$) during the fission process.
- Delayed neutrons: A smaller fraction of neutrons (approximately 0.65% in thermal reactors) is emitted with a time delay. These delayed neutrons originate from the beta decay of some fission products. These precursors subsequently de-excite by emitting a neutron. The time scales associated with their decay (on the order of seconds) are significantly longer than prompt neutron processes, making them essential for reactor stability.

To capture the neutron transient behaviour, the time-dependent neutron transport equation is coupled with the delayed neutron precursor density. The multi-group time-dependent neutron balance is governed by neutron flux equation (2.11)and the delayed neutron precursor equation (2.12).

$$\frac{1}{v_g}\frac{\partial \phi_g}{\partial t} + \nabla \cdot J_g + \Sigma_{t,g}\phi_g = \sum_{g'=1}^{G} \Sigma_{s,g'\to g}\phi_{g'} + (1-\beta)\chi_g^p \sum_{g'=1}^{G} v\Sigma_{f,g'}\phi_{g'} + \sum_{d=1}^{N_d} \chi_g^d \lambda_d C_d \tag{2.11}$$

$$\frac{\partial C_d}{\partial t} = \beta_d \sum_{g'=1}^{G} v\Sigma_{f,g'}\phi_{g'} - \lambda_d C_d \tag{2.12}$$

Where:

- β: Total delayed neutron fraction
- χ_g^p: Prompt fission spectrum for group g
- χ_g^d: Delayed neutron fission spectrum for group g
- $v\Sigma_{f,g'}$: Fission cross-section times the number of neutrons per fission for group g′
- C_d: Concentration of delayed neutron precursor group d
- λ_d: Decay constant for delayed neutron precursor group d
- β_d: Fraction of fission neutrons appearing in delayed neutron group d

2.2.2 Point Reactor Kinetics (PRK) Model

For the global and rapid analysis of core-wide transients such as rod ejection accident, the point reactor kinetics (PRK) model offers a simplified approach by collapsing the complex partial integro-differential equations (2.11) and (2.12) into a set of ordinary differential equations dependent only on time, as illustrated in (2.13) and (2.14). This is accomplished by treating the entire reactor core as a single "point," thereby separating the time dynamics from the detailed spatial and energy behavior of the neutron flux. These equations can guide what parameters should be investigated during transient simulations.

$$\frac{dn(t)}{dt} = \frac{\rho(t) - \beta}{\Lambda} n(t) + \sum_{i=1}^{6} \lambda_i C_i(t) \tag{2.13}$$

$$\frac{dC_i(t)}{dt} = \frac{\beta_i}{\Lambda} n(t) - \lambda_i C_i(t) \; (i = 1,2, \dots ,6) \tag{2.14}$$

Where:

- $n(t)$ represents the neutron amplitude, which is proportional to power.
- $\rho(t)$ is the reactivity.
- β_i is the fraction of the *i-th* delayed neutron group.
- Λ is the neutron generation time, defined as the ratio of the prompt neutron lifetime l_p to k_{eff}, $\Lambda = l_p / k_{eff}$.
- $C_i(t)$ represents the concentration of the *i-th* delayed neutron precursor group.

2.2.3 Numerical Solutions of PRK

Under highly simplified conditions, such as constant neutron source (Nahla, 2009) and prompt jump approximation (Chen, et al., 2006; Li, et al., 2007), the analytical solutions to PRK ((2.13)and (2.14)) can be derived. However, these analytical methods are limited to qualitative assessment due to their restrictive assumptions (Yamoah, et al., 2013).

For quantitative computations, numerical methods are indispensable. The stiffness of PRK system poses a challenge because various physical phenomena operate on different timescales. The numerical methods for general purpose, such as the explicit Euler, standard Runge-Kutta, or Adams methods, require an extremely small time-step to maintain numerical stability. To overcome this stiffness problem and improve computational efficiency, several specialized numerical techniques have been developed, including:

- Quasi-Static Method (Ott and Madell, 1966), this framework has led to the development of advanced algorithms including the improved Quasi-static Method (IQM) and the Predictor-Corrector Quasi-Static Method (PCQSM) (Dulla, et al., 2008). Modern Multiphysics tools leverage

QSM-based solvers for their efficiency in transient simulations (Zhou, et al., 2024; Kooreman and Griesheimer, 2021).

- Piecewise Polynomial Approaches (Hennart, 1977)
- Various forms of Padé Approximation (Aboanber and Nahla, 2004) (NOBREGA, 1971)
- Spectral deferred correction method (Shen and Kochunas, 2023).

Chebyshev Rational Approximation Method (CRAM) (Pusa, 2011). It is the state-of-the-art method for solving PRK and closely related Bateman equations for nuclide depletion. It is the foundation for many reactor physics codes, with ongoing research focused on its optimization and application (Khoshahval and Akbari, 2020)

2.3 Long-Term Reactivity Changes

This section addresses the long-term evolution of core properties, specifically the phenomena of fuel depletion and the accumulation of fission products. It outlines the governing burnup equations and their numerical solutions. Furthermore, the common nuclear fuel management strategies in SMRs are briefly reviewed in this section, including multi-batch schemes and low-leakage loading patterns.

2.3.1 Depletion Equations and Solutions

A fundamental challenge in reactor design and operation is predicting the evolution of reactor core properties over its lifetime. Knowledge of how core properties change is essential for ensuring safe and efficient operation throughout the fuel cycle. The computational process for modeling these changes is known as burnup calculation.

While the NTE accurately describes neutron population dynamics, it assumes a static material composition. In a real operating reactor, neutron interactions continuously and gradually alter the isotopic inventory, which is known as burnup. This phenomenon modifies key physical parameters, such as reactivity and neutron flux distribution, over operational timeframes typically spanning hours to days.

The two primary effects of burnup are:

- Fuel depletion and generation: Fissile nuclides are consumed, and new fissile isotopes (such as ^{239}Pu) are generated through non-fission capture;
- Fission product accumulation: Fission fragments and their decay daughters accumulate. Many of these act as strong neutron absorbers.

To accurately calculate the variations in isotopic composition during operation, a set of burnup equations must be established. Assuming the chains of fission products are linearized, a specific ordinary differential

equation governing the isotopic evolution can be formulated for each individual nuclide. The general form is expressed in equation (2.15) (Xie, et al., 2010).

Burnup equations are a large, stiff system of coupled ordinary differential equations that govern the time evolution of nuclide concentrations, as shown in (2.15) (Xie, et al., 2010).

$$\frac{dN_i(\boldsymbol{r},t)}{dt} = \beta_{i-1}N_{i-1}(\boldsymbol{r},t) - \left(\lambda_i + \sum_{g=1}^{G}\sigma_{a,g,i}\phi_g(\boldsymbol{r},t)\right)N_i(\boldsymbol{r},t) + F_i \tag{2.15}$$

Where:

The transmutation coefficient β_{i-1} represents the production rate coefficient from the parent nuclide $i-1$ to the daughter nuclide i. The transformation occurs via two primary mechanisms: radioactive decay or neutron capture, as shown in (2.16).

$$\beta_{i-1} = \begin{cases} \lambda_{i-1} \\ \sum_{g=1}^{G}\sigma_{\gamma,g,i-1}\phi_g(\boldsymbol{r},t) \end{cases} \tag{2.16}$$

The fission source term F_i represents the total production rate of nuclide i resulting from the fission of nuclide i'. It is calculated by summing the fission rates of all fissile nuclides weighted by their respective fission yields, as shown in (2.17).

$$F_i = \sum_{g'=1}^{G}\sum_{i'}\gamma_{i,i'}\sigma_{f,g',i'}\phi_{g'}(\boldsymbol{r},t), N_{i'}(\boldsymbol{r},t) \tag{2.17}$$

- $N_{i-1}(\boldsymbol{r},t)$ is the number density of the parent nuclide i-1 as a function of the spatial vector $\boldsymbol{r}$ and time t. In the linearized chain assumption, nuclide $i-1$ is the direct precursor to nuclide i.
- $N_i(\boldsymbol{r},t)$ is the number density of the target nuclide i at location $\boldsymbol{r}$ and time t.
- λ_i is the decay constant of the nuclide i,
- $\sigma_{a,g,i}$ is the microscopic absorption cross section for energy group g of the reaction where nuclide i is absorbed.
- $\phi_g(\boldsymbol{r},t)$ is the neutron flux for energy group g.
- F_i is the total generation rate of nuclide i resulting from the fission reaction. $\sigma_{f,g',i'}\phi_{g'}(\boldsymbol{r},t), N_{i'}(\boldsymbol{r},t)$ represents the fission reaction rate of the fissile nuclide i'. $\gamma_{i,i'}$ is the fission yield, representing the probability that a fission event in nuclide i' will produce nuclide i.

In (2.15), the left term is the time rate of change of nuclide i's concentration. The first term on the right hand represents the total generation rate of nuclide i caused by the decay or neutron absorption of its precursor nuclide *i-1*. The second term on the right hand is the total disappearance rate of nuclide i due to

its own decay or neutron absorption. The third term is the total generation rate resulting from the fission reaction.

The stiffness of (2.15) arises from the difference in half-lives among thousands of nuclides, ranging from fractions of a second to millions of years, which necessitates highly stable and efficient numerical solutions. Therefore, solving the burnup equations requires handling a system of stiff ordinary differential equations. Three primary categories of methods are used in reactor physics:

- Transmutation Trajectory Analysis: Originally proposed by Bateman (Bateman, 1910), this method provides an explicit analytical expression for nuclide densities when the chain involves only decay.
- General ODE Solvers: Since burnup equations are ODEs, standard numerical techniques like Runge-Kutta and linear multi-step methods can be applied.
- Matrix Exponential Method: they are suited for the stiff nature of the equations. For example, Taylor series method with scaling and squaring technique was implemented in the ORIGEN code (Croff, 1980). Others include Quadrature-based rational approximation method (QRAM) (Trefethen, et al., 2006), the Krylov Subspace Method (Yamamoto, et al., 2007), the Chebyshev rational approximation method (CRAM) (Pusa, 2011), the Laguerre polynomial approximation method (LPAM) (She, et al., 2013).

This integrated approach, where the neutronics solution informs the nuclide transformation and the resulting composition feeds back into the transport calculation, is fundamental to high-fidelity core depletion and fuel management analysis.

2.3.2 Nuclear Fuel Management

Nuclear fuel management concerns maximizing the energy extracted from the fuel while strictly adhering to all the operational limits of the reactor. The fuel management requires complex considerations spanning reactor physics, thermal-hydraulics and safety analysis. The scope of this research is limited to in-core fuel management. And the fuel management will be determined with the application of reactor physics principles, but the results will be analysed in reactor physics, thermal-hydraulics and safety analysis (Xie, et al., 2010).

Within this context, fuel management is defined as the determination of the optimal configuration of fresh and previously irradiated fuel assemblies within the objective reactor core. This involves establishing a fuel loading pattern for the start-up core and designing a refuelling strategy to achieve a stable equilibrium cycle, both targeting a cycle length of 20GWd/t.

2.3.2.1 Start-Up Core Loading Pattern

For a start-up SMR core loaded with only fresh FAs, the loading pattern is relatively straightforward. The core is radially divided into multi zones, each zone shares consistent fuel enrichment and burnable absorber

loadings. Fuel assemblies with highest enrichment and lower burnable absorber loading are positioned at the peripheral region. Conversely, assemblies with lower enrichment and higher burnable absorber loadings are placed in the inner region (NuScale, 2016) (Kumar, et al., 2020) (Choi, et al., 2020). This arrangement helps to establish a relatively uniform radial power distribution.

2.3.2.2 In-Core Material Evolution

As the core operates, the material composition of the fuel assemblies undergoes continuous alteration due to neutron interactions, which is referred to as burnup. The resulting balance between fissile material depletion, accumulation of neutron-absorbing nuclides and new fissile isotope production effect the core's reactivity. The fissile material depletion was illustrated in Chapter 2.3.1, the fission products and the fissile isotope production will be introduced here.

Fission Products

In reactors, the fissile material absorbs a thermal neutron, leading to nuclear splitting, releasing energy and neutrons.

$$^{235}U + n \rightarrow Fission\ Products + \nu n + Energy$$

The atomic fragments created during fission, which are referred to as fission products, accumulated as burnup. Some of them possess high thermal neutron absorption cross sections, such as ^{135}Xe and Samarium-149 (^{149}Sm), as displayed in Figure 2.1.

- ^{135}Xe: It is produced via the decay chain of Iodine-135. Figure 2.1 illustrates ^{135}Xe has a high cross section in thermal energy region. Its concentration is highly dependent on the local neutron flux, may leading to power instability (Xenon oscillation) when power changes (Xie, et al., 2010).
- ^{149}Sm: As a stable isotope, it acts as a strong neutron poison. Once produced, its high thermal neutron cross section (Figure 2.1) causes a significant reduction in the core's available thermal neutron flux.

The continuous buildup of these fission products is the primary factor that diminishes the core's excess reactivity over time.

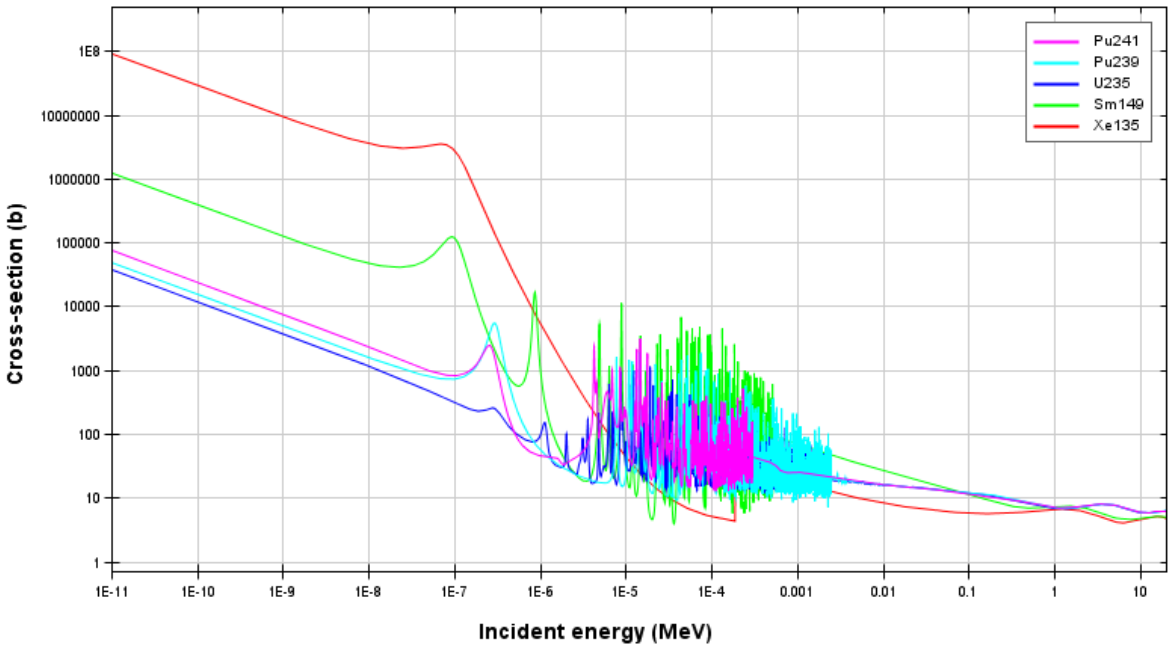

Figure 2.1 Energy dependence of the total microscopic cross section of the isotopes of fissile isotopes and fission products. Source: JANIS (Java-based Nuclear Data Information Software); ENDF/B-VII.1

Fissile Isotope Conversion

The material composition is simultaneously altered by conversion. Uranium-238 (^{238}U) is the dominant fertile isotope in the fuel. It undergoes neutron capture and subsequent beta decay, leading to the production of new fissile materials. The full chain of the nuclear transmutation process of ^{238}U is illustrated in Figure 2.2. As burnup, the production of these new fissile isotopes (^{239}Pu and ^{241}Pu) becomes critical for sustaining the nuclear chain reaction by compensating for the depletion of ^{235}U.

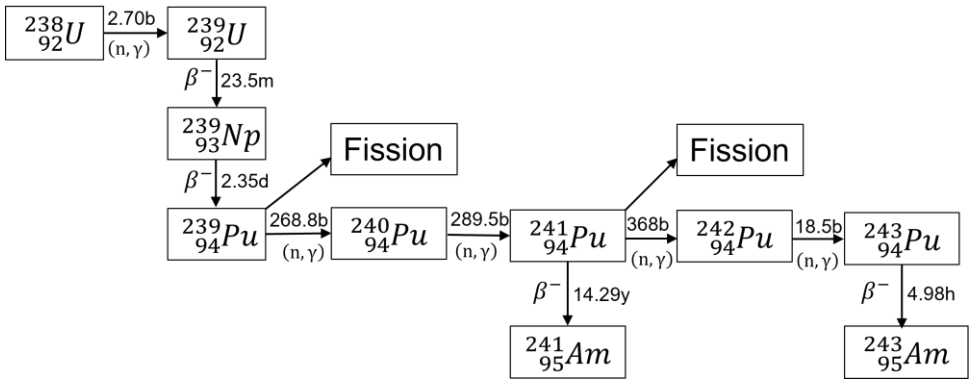

Figure 2.2 Nuclear transmutation process of ^{238}U

2.3.2.3 Refuelling Strategy and Equilibrium Cycle

As discussed in Chapter 2.3.2.2, the fission depletion and the fission products accumulation reduce the excess reactivity of the core. Hence, the reactor must be periodically shutdown for refueling, replacing the spent fuel assemblies with fresh ones so that sufficient excess reactivity is loaded for another operational cycle. The burned FAs are removed by the refueling machine and placed in the on-site spent-fuel pool which

provides a storage capacity of spent FAs for several years. After refueling is completed, the reactor can be restarted, and the power generation cycle continues.

Batch Refuelling Schemes

Refuelling strategies vary among reactors, with some employing full core replacement (Muth, 2016) (Kim D. , 2020). Because of the non-uniform neutron flux distribution (axial and radial) in the reactor core, each fuel assembly exhibits different discharge burnup despite undergoing identical irradiation period. Therefore, some FAs has reached their maximum allowable burnup while other FAs remain significant burnup potential. The partial core replacement can solve this problem: The FA with higher discharge burnup is removed from the core and the FA with lower burnup is moved to other positions in the core for further irradiation cycles until it reaches a certain burnup. Due to the more sufficient fuel utilization, partial core loading pattern is more commonly implemented (Xie, et al., 2010).

By reducing the number of fresh FAs per batch, FAs can remain long in the core, increasing their discharge burnup. However, several material properties degrade with irradiation, limiting maximum FA discharge burnup to ensure the integrity of fuel element. On the other hand, a reduced number of fresh FAs requires increased enrichment of fresh FAs (The current limit of ^{235}U enrichment is 5% (IAEA, 2020)) and increases the radial power gradient. Therefore, two-batch and three-batch refueling schemes (Lamarsh and Baratta, 2001; Duderstadt and Hamilton, 1976) are the most commonly applied, with 1/2 or 1/3 core replaced in each cycle.

Core Loading Patterns

The arrangement of fresh and burned fuel assemblies in refueling is essential for shaping the neutron flux and power distribution.

The conventional PWRs typically apply the “out-in” refueling schemes, moving partially burned FAs out of the core, relocating other burned FAs to the core central region and introducing the fresh FAs at the periphery (Glasstone and Sesonske, 2012). While this generally flattens the radial power distribution, it increases neutron leakage and irradiation damage to peripheral structures (IAEA, 2020) (Lamarsh and Baratta, 2001).

Due to their compact core geometry, SMRs inherently face the challenges of greater neutron leakage of the core and larger power gradient among adjacent FAs compared to conventional PWRs. To address the challenge of high neutron leakage, many SMR designs have adopted “low-leak” loading patterns that limit the number of high-enriched fresh FAs placed at the periphery. For example, Westinghouse SMR (Fetterman, 2011) has 89 FAs and employs a 3-batch fuel management scheme with the cycle length of 24 months. It places 16 fresh and 12 burned FAs at the core periphery. The SMR core for the commercial reactor ACP100 (Wang and al, 2021), featuring a 3-batch, 24-month cycle, houses 57 FAs with 12 fresh and 8 burned FAs in the outermost ring, achieving an average FA discharge burnup of approximately 40 MWd/t. In the ATOM core, (Nguyen, et al., 2021) adopted a 2-batch scheme with 69 FAs, placing only two

fresh FAs at the core periphery. Furthermore, to mitigate the large power gradient across the core, the fresh assemblies are often radially divided into multiple enrichment or burnable absorber zones (Nguyen, et al., 2021) (Kim D. , 2020) (R. Vuiart, 2024).

Equilibrium Cycle

Following several consecutive cycles, where a constant number of burned FAs are removed, reloaded and fresh FAs are added to fixed core positions, the main core characteristics, including FA discharge exposure cycle length and reactivity, stabilize within a small tolerance between cycles (Yamamoto, 1998) (Duderstadt and Hamilton, 1976). At this point, the core reaches a stable state where its performance and behavior are similar between cycles, which is referred to as an equilibrium cycle. The equilibrium cycle is an important core design target and it is considered to be a benchmark for any safety assessment as it represents the repeatable, long-term operational state of the reactor. Therefore, efficient refueling management is essential for achieving an equilibrium cycle which balances the fuel utilization and safety criteria.

2.4 Fundamental Thermal-Hydraulic for Core design and Safety

Reactor core design inherently involves a coupled multi-physics problem where neutronics and thermal-hydraulics are intrinsically linked. As displayed in Figure 2.3, the neutronics simulation dictates the local power distribution, which serves as the input for the thermal-hydraulics model. The temperature and density resulted from the Thermal-hydraulic simulation alter the nuclear cross-sections in turn.

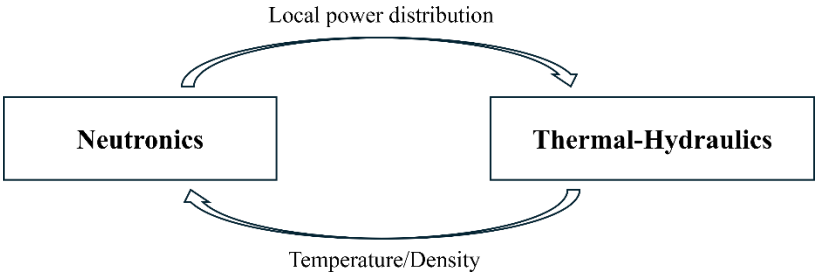

Figure 2.3 The parameters exchange in a coupled multi-physics system

Therefore, to ensure reliable results of core simulations, the neutronics and thermal hydraulics must be coupled to accurately capture these interdependent behaviors. This section introduces the fundamental thermal-hydraulic principles essential for core design and safety analysis. Specifically, it covers the heat transfer mechanisms in fuel elements, the thermal safety limit (Departure from nucleate boiling) and local temperature feedback mechanisms.

2.4.1 Heat Transfer in Fuel Elements

Efficient and safe removal of heat is a fundamental limiting factor in reactor core design. Nuclear fuel operates under extreme thermal conditions, with temperatures at the center of fuel pellets potentially exceeding 1000°C. Therefore, precise modeling of the heat transfer process at the assembly and pin level is important.

In a cylindrical fuel pin, the overall temperature drop considers a series of thermal resistances posed by the fuel, the fuel-cladding gap, the cladding, and the cladding-coolant interface. And the equations of these thermal resistances can be found in (Todreas and Kazimi, 2012). The resultant temperature profile is illustrated schematically in Figure 2.4, which shows a typical distribution within an axial slice of a fuel rod, assuming identical boundary conditions on outside of the cladding (the grey-coloured area).

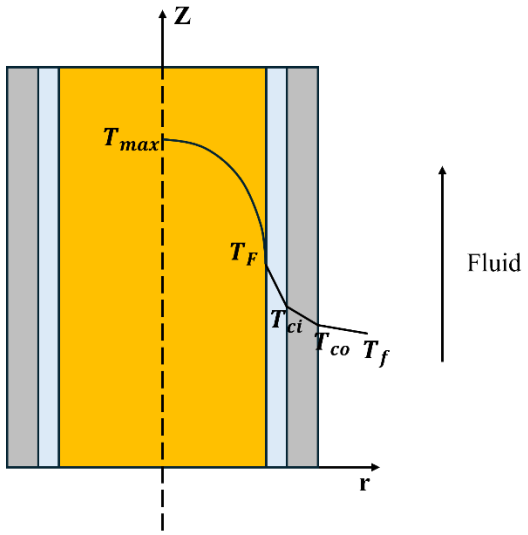

Figure 2.4 Schematic representation of the temperature distribution of a fuel element

The temperature profile exhibits the following distinct characteristics, primarily involves conduction and convection (Lahey, 1993) (Van Uffelen, 2010):

- Fuel pellet: The maximum temperature T_{max} is observed at the fuel centreline. The temperature shows a parabolic decrease in the fuel. Assuming a solid fuel pellet with a constant thermal conductivity $\overline{k_f}$, the temperature difference between the centreline and the pellet surface is given by (2.18).

$$T_{max} - T_F = \frac{q'}{4\pi\overline{k_f}} \tag{2.18}$$

  Where q' is the linear heat rate (give unit), T_{max} is the maximum fuel temperature, T_F is the temperature of surface of fuel pellet.

- Fuel-cladding gap: The heat must then cross the gas-filled gap between the fuel pellet and cladding. The temperature drop across this gap is calculated using an effective gap conductance, as shown in (2.19).

$$T_F - T_{ci} = \frac{q'}{2\pi R_g h_g} \tag{2.19}$$

Where T_{ci} is the temperature of inner surface of fuel cladding, R_g is mean radius in the gap, and h_g is the effective gap conductance. The gap conductance is a complex function of gas composition, pressure, and gap width. Detailed models for gap conductance can be found in (R. and F.E., 1979) (Lassmann and Hohlefeld, 1987) (IAEA, 1998).

- Fuel cladding: The heat then cross the fuel cladding. For a thin cladding, the temperature drop is approximated assuming linear conduction. The difference between the inner and outer cladding surfaces is calculated in (2.20).

$$T_{ci} - T_{co} = \frac{q'}{2\pi R_c k_c / \delta_c} \tag{2.20}$$

Where R_c is the mean radius in the cladding, k_c is the thermal conductivity of fuel cladding, δ_c is the cladding thickness.

- Cladding-coolant interface: The heat is finally transferred to the coolant. The temperature drop between cladding and coolant is calculated with (2.21).

$$T_{co} - T_m = \frac{q'}{2\pi R_{co} h} \tag{2.21}$$

Where R_{co} is the mean radius of the outer surface of cladding, h is the heat transfer coefficient, which is dependent on the coolant flow conditions.

2.4.2 Thermal Safety Limit: Departure from Nucleate Boiling

In a water-cooled reactor, two-phase flow boiling is a primary heat transfer mechanism during normal operation. A key thermal-hydraulic safety limit is the departure from nucleate boiling (DNB). The general boiling curve in Figure 2.5 plots the heat flux (q') as a function of the wall superheat $\Delta T_{sat} = T_{wall} - T_{sat}$, which is the difference between the wall temperature and the saturation temperature.

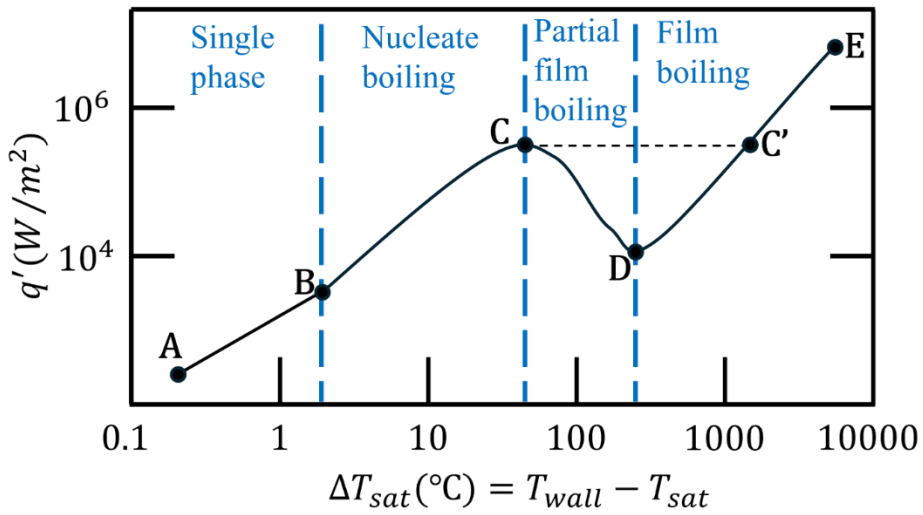

Figure 2.5 Typical boiling curve for water under atmospheric pressure

The curve can be divided into several regimes:

- A to B (Single-Phase Forced Convection): Heat is removed by convective flow without vapor formation
- B to C (Nucleate Boiling): Starting at point B, the formation of bubbles leads to significantly more effective heat transfer. This is the primary and efficient heat transfer regime during normal operation.
- Point C (Critical Heat Flux - CHF): Point C defines the Critical Heat Flux (q'_{cr}) or the start of DNB condition. It is the point at which the heat transfer rapidly decreases due to the insulating effect of a steam blanket that forms on the rod surface when the temperature continues to increase.
- C to D (Partial Film Boiling): An unstable, partial vapor film forms on the fuel cladding. This film drastically reduces heat transfer, causing the fuel and cladding to overheat and potentially leading to fuel rod failure.
- D to E (Stable Film Boiling): At point D, the minimum stable film boiling temperature is reached. Beyond this point, a continuous, stable vapor film fully insulates the cladding surface.

Therefore, Reactor core design must ensure that the operating local heat flux (q'_{local}) never exceeds the CHF at any point in the core during normal operation or anticipated transients. To assess the margin to this boiling crisis, the departure from nucleate boiling ratio (DNBR) is employed. Defined as the ratio of the CHF (q'_{cr}) at a specific location to the operating local heat flux (q'_{local}) (see (*2.22*)), the DNBR must remain above a specified safety limit for safe operation.

$$DNBR = \frac{q'_{cr}}{q'_{local}} \tag{2.22}$$

2.4.3 Local Thermal-Hydraulic Feedback Mechanisms

The core's local thermal-hydraulic feedback directly affects the local neutron flux. Two main feedback mechanisms are Fuel and Moderator Temperature coefficient (FTC and MTC).

Fuel Temperature Coefficient

The heat is generated within the fuel. When reactor power increases, the fuel temperature rises almost instantaneously, causing the FTC to manifest immediately. Therefore, the FTC is considered a prompt temperature coefficient.

FTC is driven by the Doppler effect, which relates to the resonance absorption of neutrons by fuel nuclei. As illustrated in Figure 2.6, at low temperatures, the ^{238}U resonances appear at sharp peaks in the neutron scattering cross section curve. Due to the high absorption probability, neutrons with energies near the resonances are likely to be captured before they can penetrate deeper into the fuel. This phenomenon is known as spatial self-shielding, where the outer layers of fuel absorb most resonant neutrons, shielding the inner regions from further absorption. Figure 2.6 also illustrated that as the fuel temperature increases, the thermal motion of the nuclei intensifies, broadening the resonance peaks range and reducing their peak cross-sections. As a result, neutrons that would have been fully absorbed in the outer fuel layers at low temperatures can penetrate deeper before being captured. This phenomenon weakens the self-shielding effect in resonance absorption, thereby increasing the effective resonance integral and decreasing the probability of neutrons escaping resonance capture. According to the six-factor formula (Duderstadt and Hamilton, 1976), these changes result in a reduction of k_{eff}, contributing to a negative temperature feedback mechanism. This negative feedback enhances reactor stability by suppressing power increases.

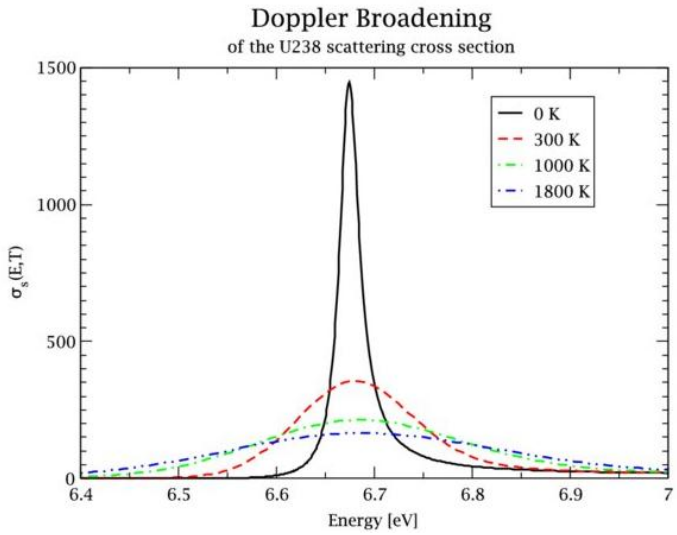

Figure 2.6 Doppler effect widening of the 6.67eV resonance scattering cross section (Becker, 2010)

Moderator Temperature Coefficient

Since heat is generated within the fuel pellet and it takes time to be transferred to the coolant, the moderator temperature change is inherently delayed compared to the fuel temperature change. Consequently, the MTC is also delayed compared to FTC, thus classified as a delayed temperature coefficient.

An increase in moderator temperature can lead to two opposing effects due to the resulting decrease in moderator density:

- Positive effect: The reduction in moderator density leads to less neutron absorption by the moderator, thereby increasing the thermal utilization. Therefore, this results in an increase in k_{eff}, introducing a positive contribution to MTC.
- Negative effect: Concurrently, the decrease in moderator density directly reduces the probability of collision between neutrons and the hydrogen nuclei in the water. This reduced collision frequency impairs the moderation of fast neutrons, leading to a "hardening" of the neutron spectrum. This harder spectrum decreases the number of thermal neutrons available to cause fission and increases resonance absorption. These effects contribute to a reduction in k_{eff}.

In conclusion, whether the MTC is positive or negative is determined by these two competing factors. If soluble boron is present in the moderator, an increase in temperature can further reduce its dissolved concentration, thereby enhancing the positive effect. This can potentially lead to a positive MTC, especially at the beginning of cycle when the boron concentration is high. Therefore, soluble-boron-free designs are beneficial as they eliminate this potential risk.

2.5 Reactor Safety Considerations for Core Design

Nuclear reactor safety relies on the defense-in-depth (DiD) principle, a multi-layered approach to ensure structures, systems and components operate within strict safety margins, as detailed in Table 2-1. DiD prevents and mitigates accidents involving radiation or hazardous material release by employing independent, redundant barriers to account for human or mechanical failures. No single layer is solely relied upon, even if highly robust.

As outlined in IAEA Safety Fundamentals (IAEA, 2006), the primary goal is to protect workers, the public and the environment from ionizing radiation throughout a facility's lifecycle, from design to decommissioning. This is achieved through four fundamental safety functions: (a) Core reactivity control; (b) Reactor core cooling; (c) Radioactive material confinement; (d) Limitation of radioactive releases.

The DiD principle is built upon two strategies:

- Accident prevention. It is of highest priority to prevent accidents from occurring.
- Consequence mitigation: If prevention fails, the second strategy is to mitigate the potential consequences of an accident and prevent its escalation to more severe conditions.

These strategies apply across all states, including normal operation, anticipated transients and accident scenarios (IAEA,1996). Post-Fukushima, (Western European Nuclear Regulators Association, 2013) reinforced DiD's hierarchical protection levels, emphasizing divers and redundant safeguards to prevent escalation.

Table 2-1 The successive level of the DiD as proposed by WENRA (Western European Nuclear Regulators Association, 2013)

DiD level	Defense Layer	Objective
1	Normal operation	Ensure normal operation and avoid abnormal operation
2	Anticipated operational occurrences (AOO)	Control abnormal operation and avoid incidents
3a	Postulated single initiating event with single failure	Control design basis accidents and prevent multiple failures of engineered safety features
3b	Postulated single initiating event with multiple failures	Control events involving an anticipated transient without scram (ATWS)
4	Postulated core melt accidents	Control events with multiple failures of safety systems to prevent accidents with severe fuel assembly damage
5	Significant release	Provide mitigative measures for accidents involving severe fuel assembly damages to maintain containment integrity and limit radioactive releases

2.5.1 Safety Criteria under Normal Operating Conditions

In core design, the primary goal is to ensure normal reactor operation and avoid abnormal operation, which directly corresponds to DiD level 1 in Table 2-1.

This goal can be achieved by monitoring several safety parameters, including power peaking factors, axial power offset, reactivity temperature coefficients, rod and assembly discharge burnup. Strict adherence to these criteria is applied for maintaining the fuel's integrity and preventing any deviations from safe operating parameters.

2.5.1.1 Radial Power Peaking Factors

Excessive local power can lead to fuel overheating, cladding failure, or even fuel melting. It may also cause a departure from nucleate boiling (DNB), significantly reducing heat transfer efficiency and further increasing fuel overheating. Therefore, maintaining the peak power factors within safety limits is crucial.

Two key parameters are monitored:

1) 3D peak pin power factor (F_q): also referred to as peak pin linear power factor. It is the ratio of the maximum local linear pin power density to the core-average pin power density.
2) 2D peak pin power factor ($F_{\Delta H}$): also referred to as nuclear enthalpy hot channel factor. It is the ratio of the integrated power along the hottest fuel rod to the average rod power.

The calculations of F_q and $F_{\Delta H}$ are defined in (2.23) and (2.24), where $P^{PIN}(x,y,z)$ is the 3D pin power, and V and S represent core volume and cross-sectional area.

$$F_q = \frac{\max\limits_{x,y,z}[P^{PIN}(x,y,z)]}{\frac{1}{V}\iiint P^{PIN}(x,y,z)dxdydz} \tag{2.23}$$

$$F_{\Delta H} = \frac{\max\limits_{x,y}[P_z^{PIN}(x,y)]}{\frac{1}{S}\iint P_z^{PIN}(x,y)dxdy} \tag{2.24}$$

Where $P_z^{PIN}(x,y) = \int_z^{\square} P^{PIN}(x,y,z)dz$

In accordance with US NRC guidelines (AREVA NP, 2013), the conservative limit for peak linear power is 44.49kW/m under normal conditions. To enhance safety margins, this study adopts the more restrictive Westinghouse limit of 35.76 kW/m (Corporation, 2005). The corresponding F_q safety limit at full power is calculated to be 3.26 by (2.25).

$$max\ F_q = \frac{peak\ power}{average\ power} = \frac{35.76kW/m}{\frac{P_{th}}{Active\ height}} = \frac{35.76kW/m}{10.964kW/m} = 3.26 \tag{2.25}$$

Where the P_{th} is 330MW and the active height is calculated as $57\text{FAs} \times \frac{264rods}{FA} \times \frac{2m}{rod} = 30096m$,.

In a PWR system, the coolant is maintained under high pressure to prevent bulk boiling (Breeze, 2014). While localized subcooled nucleate boiling may occur in high-heat-flux channels, the bulk coolant temperature throughout the primary loop must remain below the saturation temperature. Therefore, the maximum $F_{\Delta H}$ is derived using (2.26), involving the core thermal power P_{th}, primary coolant flow rate $\dot{m}$, specific heat capacity C_P ($5774.313\,^{J}/_{kg \cdot K}$ for water at 310.15℃ and 150bar (Steam, 2024)), and coolant temperatures $T_{mod,sat}$ and $T_{mod,inlet}$.

$$max\ F_{\Delta H} = \frac{\dot{m} \cdot C_P}{P_{th}}\left(T_{mod,sat} - T_{mod,inlet}\right) = \frac{2006.4kg/s \times 5774.313\,^{J}/_{kg \cdot K}}{330 \times 10^6 W} \times (615.31K - 569.15K) = 1.62 \tag{2.26}$$

In summary, the maximum limits of 3D and 2D peak pin power factors are 3.26 and 1.62, respectively.

2.5.1.2 Axial Power Offset

Axial power offset (AO) quantifies how much the reactor's axial power profile deviates from the core's midpoint. It is an important safety parameter in a SBF core as the absence of soluble boron increases the sensitivity of the peak axial power to control rod positions. Significant positive or negative AO values can elevate the risk of power excursions, which must be avoided. AO is calculated using (2.27) as:

$$AO = \frac{P_B - P_T}{P_B + P_T} \tag{2.27}$$

where P_B and P_T are the powers of the bottom and top halves of the core, respectively. The acceptable range for AO is -0.4<AO<0.4 based on SMR design considerations (Mart J. , 2013).

2.5.1.3 Temperature Reactivity Coefficients

Negative reactivity temperature coefficients provide an inherent self-stabilizing effect of a reactor core, ensuring that as temperature rises, reactivity decreases, thereby enhancing operational and transient safety. The most significant contributions are Moderator Temperature Coefficient of the reactivity and Fuel Temperature Coefficient of the reactivity.

These are calculated by the reactivity differences between two core states at different temperatures, as shown in (2.28) and (2.29).

$$MTC = \frac{\rho_{(T_M+\Delta T_M)} - \rho_{T_M}}{\Delta T_M} \tag{2.28}$$

$$FTC = \frac{\rho_{(T_F+\Delta T_F)} - \rho_{T_F}}{\Delta T_F} \tag{2.29}$$

For the self-stabilizing safety, MTC and FTC of the core must be negative. Due to the elimination of soluble boron, the MTC of a SBF core is anticipated to be less negative compared to boron-based designs (Abdelhameed, et al., 2020).

2.5.1.4 Maximum Rod and Assembly Discharge Burnup

The discharge exposure, which is the burnup depth of fuel removed from the reactor core, ideally should be as high as possible to maximize economic efficiency. However, the maximum allowable discharge exposure is constrained by the material performance of the fuel elements. This refers to the fuel element's stability under irradiation and high-temperature conditions. Consequently, to maintain the long-term integrity of these materials, UO_2 fuel has an established exposure limit of 62 GWd/t for rod average exposure and 55 GWd/t for assembly average exposure (IAEA, 2019).

2.5.2 Cold Shutdown Margin with Single Failure

Nuclear safety regulations require reactor shutdown systems to maintain core subcriticality under all operational scenarios, including postulated single failures. The Cold Zero Power (CZP) condition represents the most conservative basis for shutdown margin evaluation as it requires maximum control rod reactivity worth compared to Hot Zero Power (HZP) and Hot Full Power (HFP) conditions. To ensure robust safety margins, cold shutdown margin (CSDM) calculations incorporate the conservative single failure condition:

- The control rod with highest reactivity is assumed stuck at the fully withdrawn position
- All other control rods are fully inserted

- System is maintained at cold temperatures

Figure 2.7 illustrates the relative reactivity levels across CZP, HZP and HFP conditions. It also shows a representation of the CSDM under the single failure assumption, indicating how the shutdown margin is evaluated in the most conservative state.

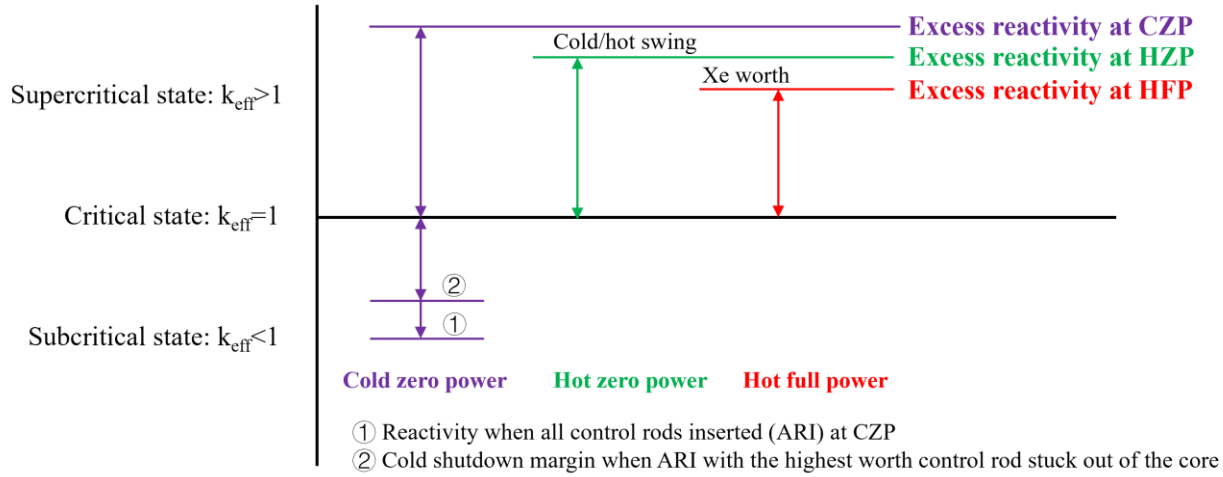

Figure 2.7 Schematic representation of reactivity difference under HFP/HZP/CZP and CSDM with single failure

This calculation supports DiD level 2 requirements in Table 2-1, ensuring reliable shutdown capability during anticipated operational occurrences with single component failure. According to (KTA, 2012), the CSDM must be at least 1000 pcm under this assumption.

In conclusion, the current safety criteria under operating condition and single control rod failure are summarized in Table 2-2.

Table 2-2 Summary of current safety criteria under operating condition and single control rod failure

DiD levels	Safety parameters	Safety ranges
1	3D pin power factor (F_q)	≤3.26
	2D pin power factor ($F_{\Delta H}$)	≤1.62
	Axial offset (AO)	-0.4≤AO≤0.4
	Moderator temperature coefficient (MTC)	< 0
	Fuel temperature coefficient (FTC)	< 0
	Rod discharge burnup	≤62GWd/t
	Assembly discharge burnup	≤55GWd/t
2	Cold shutdown margin with single failure	> 1000 pcm

3 Simulation Tools

Simulating an entire nuclear reactor core at a pin-by-pin level presents significant computational challenges due to the complexity of the NTE and burnup equations. To overcome the computational hurdles, the

nuclear industry widely adopts a “two-step” approach for core analysis, which is also applied in this study. Deterministic codes CASMO5 and SIMULATE5 are chosen for the simulations in the different steps. First, CASMO5 performs detailed 2D lattice physics calculations for each fuel assembly type in the frame of branch calculations to generate homogenized and condensed macroscopic cross section sets (libraries) taking into account different values for the state parameters such as fuel and coolant temperature, boron concentration and control rod positions for later use by SIMULATE5 and SIMULATE5-K. In this step, different burnup steps are also considered. The core simulator SIMULATE5 conducts static 3D nodal diffusion calculations in a multigroup approach as well as thermal hydraulic simulations (1D parallel channels). Before the diffusion equation is solved, SIMULATE5 perform an update of the nodal cross sections stored in the library for the actual thermal hydraulic parameters predicted by the internal TH-module and considering the actual control rod positions and burnup step. For multi-cycle operation, SIMULATE5 simulates each cycle sequentially. The state-points including isotopic inventories and material properties for first cycle are stored in *.res files. The simulation of cycle 2 is initialized by reading the necessary data from the final state-point of first-cycle’s *.res file. For the subsequent cycles, the same method is applied.

The simulation of core transients is conducted with the transient code SIMULATE5-K following the similar approach as the static ones. Prior to the application of CASMO5/SIMULATE5 for core design and optimization, a code assessment is performed. The capability and accuracy of this methodology within the specific SBF SMR core are established by comparing the benchmark results against reference calculations performed by the high-fidelity Monte-Carlo code SERPENT2.

The workflow of these simulation tools is shown in Figure 3.1. Hereafter, the selected simulation tools will be described and their main features will be highlighted.

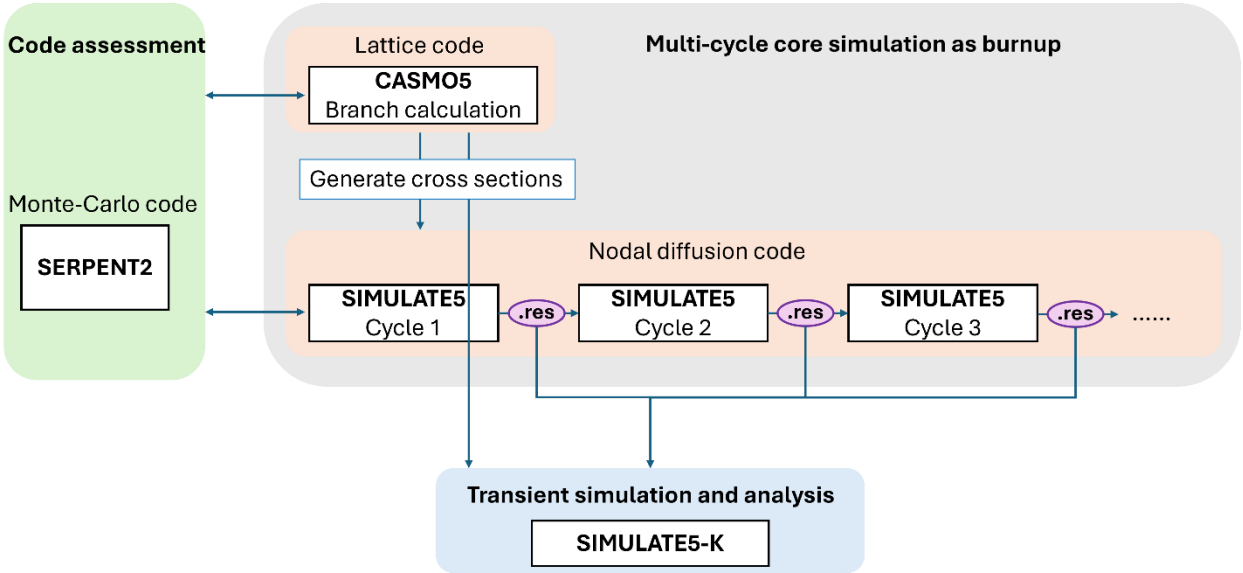

Figure 3.1 Workflow of simulation tools for code assessment, multi-cycle core simulation and transient analysis

3.1 Lattice Code CASMO5

CASMO5, SIMULATE5 and SIMULATE5-K are developed by Studsvik. CASMO5 is a two-dimensional lattice physics code for the heterogeneous transport calculations of square and hexagonal nuclear fuel assemblies. The overall methodologies of CASMO5 are outlined below (Ferrer R. M., 2022):

Multi-Group Neutron Transport Equation

CASMO5 solve the multi-group neutron transport equation using Method of Characteristics, combined with a linear source approximation.

Method of Characteristics (MOC) (Ferrer and Rhodes, 2014)

CASMO calculates the eigenvalue of (3.11) and the associated flux distribution by transforming the equation into a system of ordinary differential equations along characteristic curves. The spatial discretization involves a quadrature sphere (Figure 3.2), where $\varphi_a$is the azimuthal angle, $\theta_p$is the polar angle and the directional vectors Ω_m passes through each subdivision. Typical simulation settings include an MOC ray spacing of 0.05cm, 64 azimuthal angles and 3 polar angles.

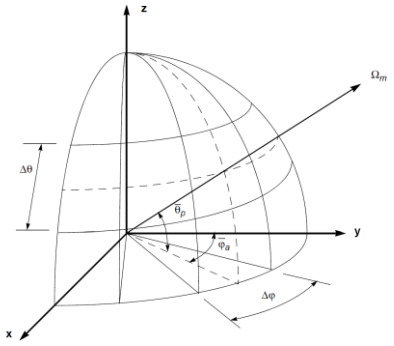

Figure 3.2 Quadrature Sphere of MOC in CASMO5 (Ferrer R. M., 2022)

Self-Shielding Method

The CASMO5 resonance treatment handles neutron energies between 10 eV and 9118 eV using an explicit approach. Resonance absorption above 111.09 keV is considered unshielded. Shielded resonance integrals are pre-tabulated in CASMO5 neutron data libraries as functions of background cross section and temperature for nuclides identified as resonance absorbers, typically 4 to 10 temperatures and up to 18 background cross section sets (Ferrer R. M., 2022). The interaction effects due to the presence of several nuclides in the same material are addressed by the inclusion of a first-order resonance interference model (Carlvik, 1965).

The spatially dependent self-shielding method in CASMO5 is a generalization of the Optimum Two-Term Rational method to fuel regions with annular subdivisions (Ferrer and Hykes, 2019) (Ferrer and Hykes, 2021). The computation of fuel-to-fuel collision probability of an annular region is derived by combining

the rational approximation of individual probabilities from four fuel lump components, where the Stoker-Weiss coefficients (Stoker and Weiss, 1996) are applied and the Nelder-Mead simplex method (O'Neill, 1971) is used.

P_N Scattering Method (Rhodes, 2005)

Neutron scattering is an anisotropic process, meaning that the probability of a neutron scattering into a particular direction depends on its incoming direction. The scattering-in term in the NTE accounts for this directional dependence. By default, CASMO5 assumes isotropic scattering, which simplifies the calculations but can introduce inaccuracies, especially in the regions with strong neutron absorbers.

To address anisotropic scattering, CASMO5 implements the P_N method, which expands the scattering source using spherical harmonics and Legendre polynomials. The order of the P_N approximation (N) determines the level of anisotropy considered. A P_0 approximation corresponds to isotropic scattering, while higher orders (P_1, P_2, P_3, etc.) progressively account for more complex angular dependencies.

CASMO5 utilizes different quadrature sets for the polar angle integration depending on the requested P_N order: For P_N orders up to and including 3, the Tchebychev-Yang optimum quadrature (Tabuchi, et al., 2005) is employed; For P_N orders greater than 3, the Gauss-Legendre quadrature set is used.

Energy Group Structure

CASMO5 offers several options for energy group discretization, supporting up to 586 energy groups. The 586 energy groups contain 128 fast groups (20 MeV to 9.118 keV), 41 resonance groups (9.118 keV to 10 eV), 375 fine groups (10 eV to 0.625 eV), and 42 thermal groups (below 0.625 eV) (Ferrer and Rhodes, 2021). To decrease execution time, a reduced number of energy groups can be selected depending of the energy spectrum of the core. For core loadings with UO_2 fuel, the default setting uses 19 energy groups.

Spatial Discretization (Ferrer R. M., 2022)

CASMO5 offers flexible spatial discretization options to model the heterogeneous geometry of fuel assemblies. For fuel pins containing burnable poisons like gadolinium, which exhibit strong self-shielding effects due to high neutron absorption, CASMO5's default setting subdivides the fuel pellet into 10 radial rings. In contrast, other regions within the fuel assembly, such as the cladding and moderator, are typically modelled with a single radial ring, as the neutron flux variations are less pronounced in these areas.

Fuel Depletion

For fuel depletion calculations, CASMO5 employs the Chebyshev Rational Approximation Method (Pusa, 2011). This method provides an efficient and precise solution to the Bateman system of equations, which describes the isotopic changes in nuclear fuel over time.

Branch Calculations (Hykes, 2022)

In CASMO5's 2D lattice simulations, the fuel and coolant temperatures are treated as specific, fixed values. However, for 3D core simulations, the temperatures of all components vary both radially and axially across the core. Therefore, generating accurate cross sections for SIMULATE5 core simulations necessitates performing branch calculations. The CASMO5 branch calculations involve a series of repeated calculations that cover a wide range of scenarios and thermodynamic states, including the following parameters:

- Moderator temperature variation: 293–615 K
- Fuel temperature variation: 293–1500 K
- Different burnup states: ranging from 0 to 80 GWd/t depletion state-points
- Control rod insertions and withdrawals

Nuclear Data Library

The neutron data library used in CASMO5 is primarily based on the ENDF/B-VII.1, supplemented by TENDL-2012 data. The library's structure and scope are extensive:

- It contains 586-energy-group data for 1095 nuclide identifiers.
- The nuclide coverage encompasses 119 heavy nuclides and 491 fission products.
- In full extended mode, the library models up to 2341 nuclear reactions.

The library utilizes ENDF/B-VII.1 data for fission yields, radioactive decay, and delayed neutron data. Furthermore, the implementation of TENDL-2012 data ensures the nuclides previously represented only by yield/decay information now possess at least an absorption-only model, thereby guaranteeing that the neutron absorption effects are considered for all nuclides within the library.

3.2 Core Simulator SIMULATE5

The branch calculations performed by CASMO5 generate detailed data files from 2D individual FA models and 1D reflector models, covering a broad range of operational scenarios and thermodynamic states. These outputs are then processed by CMSLINK5, which homogenizes and condenses each FA and reflector model into a single segment. All such segments are compiled into a unified "*.lib" library file. This "*.lib" file contains all the necessary data for subsequent 3D core simulation, including neutron physical and kinetic parameters, isotopic, and multigroup sub-mesh cross sections for every segment.

The 3D core simulation is carried out using SIMULATE5. SIMULATE5 (Scott.V, et al., 2021) is a 3D, steady state, multi-group, nodal core simulator for the analysis of both PWRs and Boiling Water Reactors (BWRs). The following methodologies will be described in this section.

The overall 3D neutronics calculation methodology involves implementing the high-speed global 3D solver using analytic nodal method and continuously correcting its input data with the 1D axial homogenization and 2D sub-mesh model. Notably, the cross-section data is continuously corrected by the fuel and moderator

temperature. To achieve a higher spatial accuracy beyond the node-average flux computed by this 3D global solver, the SMX method is used in SIMULATE5 for pin power reconstruction.

Furthermore, the core simulation accounts for changes in fuel composition during burnup. Therefore, the fuel depletion model in SIMULATE5 addresses the task of tracking nuclide concentrations and the resulting microscopic cross sections within each node. To simplify the computational cost, SIMULATE5 employs a hybrid macroscopic/microscopic depletion model for the core depletion simulations.

During operational cycles, control rod axial positions serve as the adjustable parameter to maintain core criticality. To search for control rod critical positions at each burnup state-point, SIMULATE5 involves an iterative searching process.

Finally, SIMULATE5 conducts each cycle sequentially for multi-cycle simulations. The approach is to employ a restart file to ensure proper sequential initialization and data carry-over between cycles.

3.2.1 3D Neutronics Solver

SIMULATE5 solves the 3D multi-group diffusion equation (2.10) iteratively to determine the average neutron flux in every node of the core. To account for fine details in each node, SIMULATE5 requires correction parameters from separate 1D and 2D models provide local detail and corrections to the 3D solver (Bahadir and Grandi, 2021).

The 3D multi-group diffusion equation (2.10) is written into compact matrix form. Since this study considers the problems without a fixed neutron source, the equation simplifies to (3.1) (Bahadir and Grandi, 2021).

$$-\nabla \cdot \boldsymbol{D}\nabla\phi + \boldsymbol{\Sigma}_g\phi = 0 \tag{3.1}$$

Where:

$$\boldsymbol{\Sigma}_g = -\boldsymbol{\Sigma}_{t,g} + \boldsymbol{\Sigma}_{s,g'\to g} + \frac{1}{k_{eff}}\chi_g \nu\boldsymbol{\Sigma}_{f,g'\to g}$$

To derive the nodal balance equation, equation (3.1) is integrated over the volume of node n (V_n).

$$-\int_{V_n} \nabla \cdot (\boldsymbol{D}\nabla\phi)\, dV + \int_{V_n} \boldsymbol{\Sigma}_g\phi dV = 0 \tag{3.2}$$

Applying the Gauss's divergence theorem and substituting (2.9), the volume integral can be converted to an area integral over the surface S_n, as expressed in (*3.3*).

$$\oint_{S_n} \boldsymbol{J}\cdot\boldsymbol{n}dS + \int_{V_n} \boldsymbol{\Sigma}_g\phi dV = 0 \tag{3.3}$$

Since the boundary of node *n* is composed of six surfaces corresponding to the interfaces with the six adjacent neighbouring nodes *m*, the total surface area integral can be written as the summation over these six interface areas, thereby yielding the nodal neutron balance equation (3.4):

$$\sum_{m=1}^{6} \frac{1}{h_{nm}} \bar{\boldsymbol{J}}_{nm} + \boldsymbol{\Sigma}_n \overline{\phi}_n = 0 \tag{3.4}$$

Where $\overline{\phi}_n$ is the node average flux in node *n*, $\bar{\boldsymbol{J}}_{nm}$ is the net average leakage current from node *n* to adjacent node *m*, h_{nm} is the node size in direction from node *n* to *m*, $\sum_{m=1}^{6}$ represents the summation over the six neighbours of node *n*. The unknown parameters are node average flux $\overline{\phi}_n$ and the net average leakage current between adjacent nodes $\bar{\boldsymbol{J}}_{nm}$. The steps are described below:

- 3D to 1D Reduction: The 3D problems is broken down into three independent 1D multi-group problems for directions *u(x,y,z).* The transverse leakage of other two directions is assumed to have a parabolic shape.
- Spectral Analysis: Each 1D multi-group (assuming G energy groups) problem is converted into a system of G independent on-group equations using spectral analysis.
- Deriving the Final Nodal Equation: The $3 \times G$ one-group equations are solved analytically to establish a relationship between the node's interface net current and the node average flux. These relations are then substituted back into the equation (3.4), resulting in the node average flux $\overline{\phi}_n$ only remaining unknown.

The global 3D solver assumes that each node is internally homogeneous. To account for the heterogeneous details, the 1D axial homogenization model and 2D sub-mesh model provide the local detail and corrections for the global 3D solver.

- 1D axial homogenization model: The core is axially non-uniform due to factors such as control rods axial positions and the existence of spacer grids. The model corrects the 3D solver by providing axial discontinuity factors and flux weighting factors.
- 2D sub-mesh model: In each axial slice, a fuel assembly node has complex internal details including fuel rods, burnable absorber rods, control rods and water). The model provides radial discontinuity factors and radially re-homogenized cross sections to correct for non-uniformity in the X-Y plane.

3.2.2 Pin Power Reconstruction

To achieve a higher spatial accuracy beyond the node-average flux computed by the 3D global solver, SIMULATE5 employs two pin power reconstruction techniques: the SMX method and the Fourier flux expansion method. Both methods assume that a node is homogeneous in the axial direction, with axial heterogeneities handled by the 1D axial homogenization model.

The SMX method is used in this thesis for pin power reconstruction, synthesizing the power of individual fuel pins by correcting the nominal CASMO5 power form factor with a ratio derived from the 2D corrected power map and the simplified single-assembly map, which is expressed in (3.5).

$$P_i = \sum_{g'=1}^{G'} \frac{P_{g'i}^{2D}}{P_{g'i}^{SA}} \cdot P_{g'i}^{CAS} \tag{3.5}$$

Where P_i is the in power for pin i, g' is the form factor energy groups and $G'$is the number of form factor energy groups. $P_{g'i}^{CAS}$ is the power form factor computed in the single-assembly lattice model by CASMO5. This nominal form factor is corrected by the ratio of $P_{g'i}^{2D}$ and $P_{g'i}^{SA}$, which are the 2D corrected power map and the simplified single-assembly map. Both maps are calculated by summing over the fine energy groups g of the product of a cross-section term and a neutron flux term, as shown in (3.6) and (3.7).

$$P_{g'i}^{2D} = \sum_{g=G_1}^{G_2} \frac{\kappa}{\langle V \rangle} (\Sigma_{fgs}^{0} + \Delta\Sigma_{fgs}) \cdot \phi_{gi}^{2D} \tag{3.6}$$

$$P_{g'i}^{SA} = \sum_{g=G_1}^{G_2} \frac{\kappa}{\langle V \rangle} \Sigma_{fgs}^{0} \cdot \phi_{gi}^{SA} \tag{3.7}$$

Where κ is the energy conversion factor that converts fission rate to thermal power. $\langle V \rangle$ is the average volume term, Σ_{fgs}^{0} is the macroscopic fission cross-section for energy group *g'*, $\Delta\Sigma_{fgs}$ is the correction term for the fission cross-section. $\phi_{g'i}^{2D}$ and $\phi_{g'i}^{SA}$ are the 2D submesh neutron flux and the simplified submesh neutron flux for pin *i* and group *g'*.

3.2.3 Fuel Depletion Modelling in SIMULATE5

Due to the depletion during core simulation, the fuel depletion model is introduced here. As we mentioned in Chapter 2, the neutron flux is obtained from Boltzmann transport equation, and burnup equations use these as input to track the nuclide concentrations. The fuel depletion model in SIMULATE5 addresses the task of tracking nuclide concentrations and the resulting microscopic cross sections within each node. These parameters are strongly influenced by local conditions, such as coolant density, control rod insertion, and operational history. Therefore, tracking numerous isotopes at fine geometrical resolutions is too computational-consuming for the full-core analysis. Therefore, SIMULATE5 employs a Hybrid Macroscopic/Microscopic Depletion Model for the core depletion simulations (Bahadir and Grandi, 2021).

The Macroscopic Depletion Model

The Macroscopic Depletion Model serves as a first-order correction for depletion effects. It parameterizes key nodal parameters, including macroscopic cross sections, assembly discontinuity factors, and pin form

factors, as pre-calculated functions of History Variables (HVs). These HVs encapsulate the operating history of each node, accounting for factors such as moderator temperature and control rod insertion.

A distinguishing feature of this model is the use of a weighting function (w), which emphasizes recent operational history, thereby ensuring that cross sections are more sensitive to recent changes in state parameters. In depleting sub-node from exposure E_n to $E_n + \Delta E_n$, the HV is updated according to the following expression in (*3.8*):

$$HV(E_n + \Delta E_n) = \frac{HV(E_n) \cdot E_n + w \cdot V(E_{n-1}) \cdot \Delta E_n}{E_n + w\Delta E_n} \tag{3.8}$$

Here, w is the weighting function that controls the influence of recent history.

Nodal exposure is updated via a standard predictor/corrector depletion method. The final end-of-step exposure ΔE_n is determined by weighting the predicted and corrected exposure increments ΔE_n^{pred} and ΔE_n^{corr} using a factor w_i, which allows the user to select depletion based on Beginning-of-Step (BOS), End-of-Step (EOS), or an average approach.

The Microscopic Depletion Model

For a more detailed representation of fuel evolution, the microscopic depletion model explicitly tracks the time-dependent number densities of key nuclides, including heavy nuclide, fission product, and burnable absorber. The general burnup equation for the number density of isotope-*i* in a linearized chain is expressed in (*3.9*).

$$\frac{dN_i(t)}{dt} = y_i + g_{i-1}N_{i-1} - l_iN_i(t) \tag{3.9}$$

Where y_i is the total fission yield, $g_{i-1}$is the production rate of isotope *i* due to capture and decay of predecessor of isotope *i-1*, and l_i is the removal rate of *i* due to absorption or decay of isotope *i*.

This model solves a system of the ordinary differential equations (3.9) that describe nuclide production and destruction. To maintain computational efficiency without compromising accuracy, SIMULATE5 applies a linearized chain approximation. The system of equations is solved analytically using Laplace transformation and back substitution (Stammler and Abbate, 1983), providing a non-iterative and robust solution for number densities between time steps. The overall calculation is implemented using the standard predictor/corrector depletion method, where the final number density at step n+1 is derived as a weighted average, see (3.10).

$$N_{n+1} = w_i \cdot N_{n+1}^P + (1 - w_i) \cdot N_{n+1}^C \tag{3.10}$$

Where N^P and N^C are the predictor and corrector number densities, and w_i is the weighting factor, typically 0.5 for balanced depletion.

Additionally, an iterative flux scaling technique is employed to ensure that the computed burnup increment $\Delta E'$ matches the user-defined step size ΔE. This is particularly important due to the rapid evolution of the fissile inventory over time.

Two depletion chains receive specialized treatment:

- Iodine-135/Xenon-135 ($^{135}I/^{135}Xe$): Given the significant absorption cross section of ^{135}Xe and its impact on core criticality, this chain is solved independently using a dedicated analytical time-dependent integration (SIMULATE-3 Speed-up Models, SSP-97/10). The method assumes linear time dependence for flux and iodine concentration, while modelling xenon concentration as a quadratic function of time, thereby accurately capturing transient behaviour.
- Burnable absorbers (Gd in this study): To address the strong spatial self-shielding of gadolinium isotopes, SIMULATE5 can replace individual Gd chains with an effective isotope (Weiss, 1990). Due to the rapid variation of the effective cross section with concentration, the model uses small depletion sub-steps (e.g., 0.1 MWd/kg) to update the cross section based on the current number density, ensuring accurate depletion rates.

The microscopic depletion model initializes and corrects number densities using reference data. The process begins with Reference Single-Assembly Number Densities N^SA, which are pre-calculated and tabulated by CASMO5. These reference values are then adjusted to reflect actual fuel assembly specifications. Two primary corrections are applied:

- Heavy Metal Loading Correction: Adjusts the initial heavy metal loading from the CASMO5 model to match the as-built loading in the SIMULATE5 assembly, ensuring the correct starting mass of heavy nuclides in each node.
- As-Built Enrichment Correction (Fresh Fuel): For fresh fuel, the number densities of ^{234}U, ^{235}U, and ^{238}U are scaled according to the ratio of the actual SIMULATE5 ^{235}U enrichment to the reference enrichment used in CASMO5.

SIMULATE5's hybrid depletion modelling strategy effectively combines the computational efficiency of a macroscopic approach with the detailed isotopic tracking of a microscopic model. The macroscopic model provides rapid first-order corrections based on operational history, while the microscopic model delivers high-fidelity depletion analysis for key nuclides. This dual approach allows SIMULATE5 to perform accurate, full-core depletion simulations.

3.2.4 Control Rod Positions Search for Criticality Maintenance During Burnup

To determine the core's critical state, the equation (2.10) is reformulated as an eigenvalue form in (3.11) (Bell and Glasstone, 1970)

$$\alpha\phi_\alpha = \boldsymbol{L}\phi_\alpha \tag{3.11}$$

Where ϕ_α is the neutron flux, α is the eigenvalue, $\boldsymbol{L}$ is the time-independent transport operator. Upon convergence, the eigenvalue α should equal 1 under critical conditions. In SIMULATE5, (*3.11*) is solved using the power iteration method, accelerated by the Chebyshev method.

In this study, where no soluble boron is present in the coolant, control rod position serves as the adjustable parameter to maintain core criticality during burnup.

The program flow involves an iterative process to search for control rod critical positions, as shown in Figure 3.3.

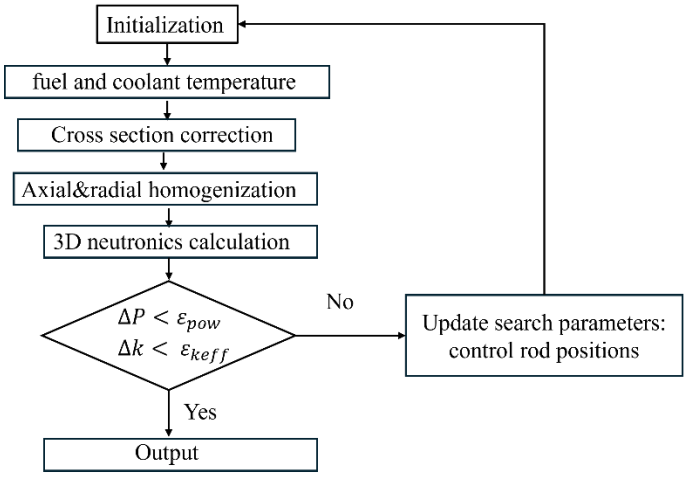

Figure 3.3 Control rod critical positions search in SIMULATE5 (Bahadir and Grandi, 2021)

The main steps are outlined below:

- Initialization: The iteration begins with thermal-hydraulic calculations, including fuel and coolant temperatures necessary for subsequent cross-section calculation.
- Cross-Section Correction: Nuclear cross-sections are updated based on the temperature determined in the initialization step.
- Axial and Radial Homogenization: This procedure is performed to derive the nodal constants need for the 3D neutronics solver.
- 3D Neutronics Calculation: The neutron flux distribution is solved by performing a 3D neutronic calculation, solving the 3D diffusion equation.
- Convergence Check: The program checks if the power/void iteration has converged. The iterative is considered converged only when both the relative power distribution (ΔP) and the effective multiplication constant (Δk) satisfy predefined tolerances (ε_{pow} and ε_{keff}):

$$\begin{cases} \Delta P < \varepsilon_{pow} \\ \Delta k < \varepsilon_{keff} \end{cases}$$

- Output: If the convergence criteria are met, the program outputs the results at this statepoint.

3.2.5 Restart Capabilities

For multi-cycle operation, SIMULATE5 simulates each cycle sequentially. The methodology is to use a restart file to ensure proper sequential initialization and data carry-over between cycles. As displayed in Figure 3.4, all the state-point data of cycle *i* are calculated and generated during depletion simulation and written into a restart file, which contains all necessary data for cycle *i+1* to resume a calculation from a specific depletion state-point of cycle *i*, including previously input data (e.g., core geometry, base conditions, control rod configurations, and fuel designs) and calculated historical nodal data (e.g., exposures, fuel temperature history). For the subsequent cycle *i+1* simulation, the required data is read from one state-point of the restart file. While these data provide the initial conditions, they can be selectively overridden with new input parameters such as fuel assembly relocation and control rod layout changes.

Additionally, restart files generated by SIMULATE5 can be used in S5K to perform transient analysis initiated from a specific depletion state-point.

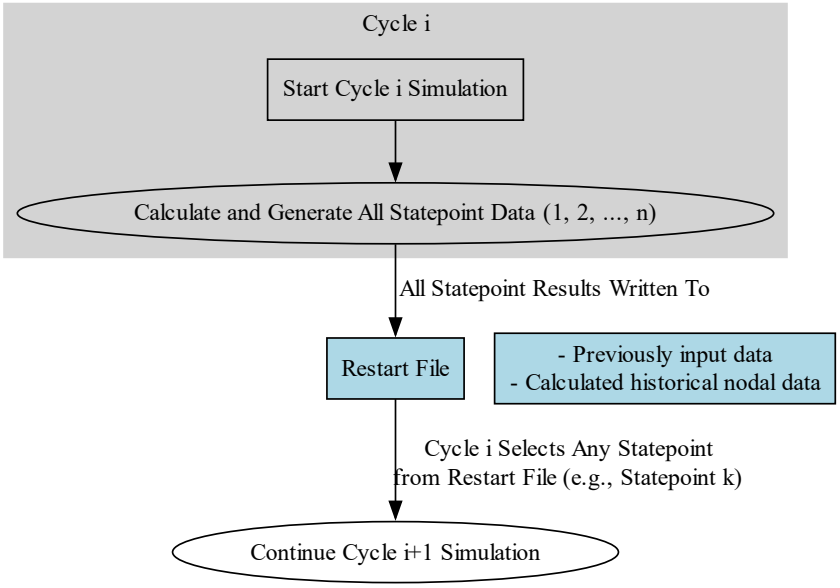

Figure 3.4 Multi-cycle simulation methodology with restart file in SIMULATE5

3.3 Transient Code SIMULATE5-K

SIMULATE5-K (S5K) is a transient nodal reactor analysis tool developed by Studsvik and is fundamentally an extension of the steady-state code SIMULATE5 (S5) (G. and Tamer, 2023). This ensures model consistency between steady-state and transient calculations. This consistency is achieved because S5K solves the time-dependent diffusion equation using a nodal method that is consistent with the one

implemented in S5. Furthermore, both S5 and S5K share the same analytical nodal model, advanced axial and radial homogenization models, and cross-section libraries. The details of the S5K methodology are outlined in (Bahadir, 2022).

S5K solves the time-dependent multi-group diffusion equations (2.11) and (2.12) with two steps: spatial integration and temporal integration.

Spatial Integration

The time-dependent diffusion equation is converted to a pseudo-static diffusion equation by introducing the dynamic frequencies of the neutron flux and delayed neutron precursor concentrations. The neutron flux and precursor concentration are assumed to have an exponential behavior during the time interval Δt, from times step t_p to t_{p+1}:

$$\phi_g(r,t) = e^{\omega_g(t-t_p)}\phi_g(r,t_p)$$

$$C_d(r,t) = e^{\omega_d(t-t_p)}C_d(r,t_p)$$

Substituting them into the balance equations (2.11) and (2.12) and eliminating C_d yields the static-like equation (3.12).

$$\nabla \cdot J_g + \tilde{\Sigma}_{tg}\phi_g = \sum_{g'=1}^{G}\left(\tilde{\chi}_g \nu\Sigma_{f,g'\to g} + \Sigma_{s,g'\to g}\right)\phi_{g'} \tag{3.12}$$

Where $\tilde{\Sigma}_{tg}$ is the effective fission spectrum, which merges the contributions of prompt and delayed neutrons.

This equation is solved with the existing steady-state nodal method of SIMULATE5.

Temporal Integration

S5K employs the frequency transformation method for temporal integration. The neutron flux is assumed to be separated into two parts:

$$\phi_g(r,t) = e^{\omega_g(t-t_p)}\psi_g(r,t) \qquad t_p \le t \le t_{p+1}$$

Through mathematical rearrangement and implicit time integration, the equation takes the compact form in (3.13).

$$\phi_n^{p+1} = \sum_{m=1}^{6} A_{nm}\phi_m^{p+1} + b_n \tag{3.13}$$

- The term on the left side, ϕ_n^{p+1}, represents the neutron flux at the new time step *p+1*.
- The first term on the right side represents the neutron current/flow from the adjacent nodes m into node n.

- The second term on the right side is the Fixed Source Term. It contains all the known information from the previous time step p, including known fluxes and precursor information, as well as the known source terms generated during the transient.

Since b_n is treated as a constant during the iterative solution for the current time step, the entire transient problem is effectively transformed into a series of solvable, spatially coupled static problems. The final compact form of the equation is solved with the existing S5 fixed-source solver, which uses Gauss-Seidel iteration accelerated by the Cyclic Chebyshev Semi Iteration method.

3.4 Monte-Carlo Code SERPENT2

SERPENT2 (Leppänen J. , et al., 2025) is a 3D continuous-energy Monte-Carlo neutron and photon transport code, developed at VTT Technical Research Centre of Finland. The key features of SERPENT2 are outlined below:

- Continuous-energy physics: It tracks individual neutron histories and their interactions within material in defined geometries. it utilizes continuous-energy cross-section data from standard ACE-format nuclear data libraries, such as ENDF/B-VII.1, JEFF-3.2, JENDL-4.0 and FENDL-3.0, to represent neutron interactions without multi-group condensation approximations.
- Doppler treatment: The code achieves consistent neutronic feedback using Target motion sampling for on-the-fly, continuous-energy doppler broadening based on local fuel temperatures (Viitanen, 2015).
- Depletion method: SERPENT2 can perform static, burnup, and transient analysis. It includes a modern depletion solver, which primarily uses CRAM within predictor-corrector schemes (Leppänen J. , 2015).
- Particle tracking: The particle transport efficiency is optimized via a hybrid algorithm combining conventional ray tracing with Woodcock delta-tracking (Woodcock, et al., 1965).
- Coupling interface: SERPENT2 is designed for multi-physics simulations, featuring a built-in interface that exchanges data with external solvers (Leppänen J. , et al., 2025).
- Domain decomposition: To manage the high computational cost and memory requirements of Monte Carlo simulations (a minimum of 3GB is recommended for full-cycle analysis (Leppänen J. , 2015)), SERPENT2 employs a collision-based decomposition method, assigning domains based on material type rather than fixed geometry boundaries. Neutrons are transferred to a foreign node only when a collision occurs within a material belonging to that domain (Leppänen J. , et al., 2025).
- code uses memory-efficient domain decomposition and a hybrid parallelization technique (MPI and OpenMP), enabling pin-resolved full-core simulations on high-performance computing platforms.

3.5 Assessment of CASMO5/SIMULATE5 Simulations using SERPENT2

Given the inherent approximations of deterministic codes, CASMO5 and SIMULATE5 will be verified before their application in the core design process. This chapter details the neutron-physics assessment of CASMO5 and SIMULATE5, using Monte-Carlo code SERPENT2 as the reference. The assessment will utilize benchmarks including different fuel assembly and core configurations under distinct operating states. The basic geometric data of pins, fuel assemblies and core are summarized in Section 1.2.5.

The assessment is structured into two main phases:

- First, a parametric study is conducted with CASMO5 against SERPENT2 to determine the optimal parameter settings for cross-section generation, including energy group number and order of P_N scattering approximation. This step is important because the accuracy of SIMULATE5 core simulation is highly dependent on the precision of the cross-section generated by CASMO5. The parametric study is conducted under hot full power condition (HFP in Table 3-1). For the lattice-level assessment, three different fuel assembly configurations are considered, featuring different fuel enrichments, gadolinium concentrations and the presence or absence of control rods (please give the reasons). The primary comparison of this assessment is the infinite multiplication factor (k_{inf}) across varying parameters. The state parameters such as coolant density, fuel and coolant temperatures are kept consistent between CASMO5 and SERPENT2 models. With the optimal P_N scattering order and energy group number, the pin power distribution for these configurations is compared to further confirm the reliability of the assembly-level results.
- Secondly, the optimal CASMO5 settings are applied to generate the branch cross-section data for SIMULATE5 core model, which is assessed against SERPENT2 full-core model. The core model assessment covers a range of operating conditions, including cold zero power (CZP), hot zero power (HZP) and HFP with the coolant density obtained from (Fernández-Prini and Dooley, 1997), as detailed in Table 3-1. And the results comparison for the core model focuses on effective multiplication factor (k_{eff}) and the axially-averaged radial power distribution. This step evaluates the capabilities of the optimal CASMO5 settings for full-core models under a variety of operating states.

Table 3-1 Operating conditions of benchmark models

States	Fuel Temperature (K)	Coolant Temperature (K)	Temperature of other materials (K)	Coolant density (g/cm^3)
CZP	300	300	300	0.99656
HZP	569.15	569.15	569.15	0.73371
HFP without TH	900	590	590	0.68700

3.5.1 CASMO5 Parametric Study for Fuel Assemblies

All neutron and gamma libraries required by SIMULATE5 are generated by CASMO5. These data include the homogenized few-group cross-sections, along with the multi-dimensional look-up tables that describe their dependence on various state parameters (burnup, temperature, etc.). The accuracy of the SIMULATE5 core simulation is therefore directly dependent on the fidelity of the data provided by CASMO5. Therefore, a parametric study will be performed on various fuel assembly configurations under hot full power (HFP) to determine optimal settings in CASMO5 for cross-section generation. This involves comparing CASMO5 and SERPENT2 simulations using identical geometric data and boundary conditions.

The lattice models are performed under CZP, HZP and HFP conditions, using a reflective boundary condition. And the boron concentration is set to 0ppm for all cases. Three different fuel assembly configurations are investigated in the 2D lattice models assessment, as detailed in Table 3-2. Their differences in fuel rods, control rods, and burnable absorber rods layouts of these configurations are displayed in Figure 3.5. These configurations were chosen to encompass a broad range of neutronic conditions in the core model. These configurations span different fuel enrichment (3%, 4.5%), different gadolinium rod number per fuel assembly (16, 24) and different gadolinium loading (4%, 8%). These ensures the assessment covers both high and low fuel enrichment and burnable absorber concentrations, which significantly impact local flux distributions. Additionally, the configurations were chosen to evaluate the modeling of various control rod worth within the 2D lattice models. Configuration 1 represents the fully withdrawn control rod condition, where guide tubes are filled with water. Configuration 2 simulates the safety bank fully inserted state by present 24 Ag-In-Cd rods in one fuel assembly. Configuration 3 models the regulating bank inserted condition by combining 12 Ag-In-Cd and 12 Stainless steel rods in a single fuel assembly. These combinations ensure the effect of different control rod material can be simulated by CASMO5.

Table 3-2 List of all fuel assembly configurations to be investigated in 2D lattice models assessment of CASMO5 against SERPENT2

Configurations	Fuel enrichment (%)	Gd rod number per FA	Gd loading (wt%)	CR present
1	4.5	24	8	No
2	3	16	4	Ag-In-Cd
3	4.5	24	8	Ag-In-Cd+SS

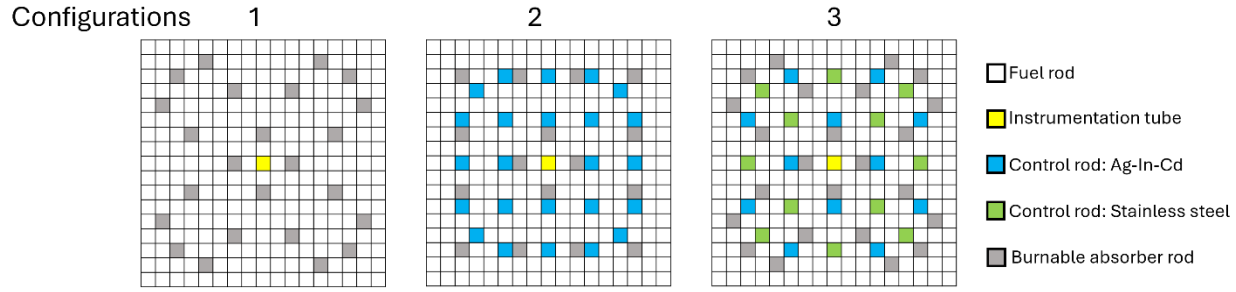

Figure 3.5 Rods layout in selected fuel assembly configurations

Both CASMO5 and Serpent2 simulations are performed and their predicted infinite multiplication factors k_{inf} are compared, with the Serpent2 results serving as the reference. The reactivity difference Δρ is calculated by $\Delta\rho = \rho_{CASMO} - \rho_{SERPENT}$, where $\rho = (1 - \frac{1}{k_{inf}}) \times 10^5$. The Serpent convergence criteria for k_{inf} among these configurations are between 3.3E-5 to 1.0E-4, resulting in a reactivity uncertainty below 5 pcm. All the isotopes and their mass fraction containing in the materials in SERPENT2 models can be found in Appendix A.

In the steady-state multi-group neutron transport equation (2.8), the neutron flux is a function of the energy group g, the direction of neutron travel Ω and the spatial position *r*. For the simulations using the MOC method to resolve the spatial dependence *r*, the accuracy of neutron flux calculation is primarily influenced by the choice of the energy group division g and specific directions Ω.

In CASMO5, the continuous neutron energy spectrum is approximated by a multi-group energy structure. The number of energy groups affects the precision of this approximation: while finer energy group structures yield more accurate results, they require greater computational resources. Therefore, a parametric analysis is conducted on the energy group numbers.

Furthermore, the P_N method is employed in CASMO5 by expanding the scattering term in spherical harmonics. The chosen P_N order determines the level of detail in the angular representation of neutron scattering. Higher-order P_N can better capture anisotropic scattering behaviour but require increased computational time. Hence, the P_N-scattering order in the spherical harmonics, which affects the scattering-in term, is considered in the parametric analysis.

In summary, for consistent comparison of the parametric study with the results, the following CASMO5-parameters are changed while the other parameters are kept remained:

- Number of energy groups: 8, 19, 35, 95, 306, 586
- P_N- scattering approximation: 0, 1, 2, 3, 4, 5

To get a reliable reference solution, SERPENT2 simulations of the selected cases are performed using 100000 neutrons per generation, 1000 and 100 active and inactive cycles.

3.5.1.1 Impact of the Number of Energy Groups in the CASMO5 2D Transport Calculation

In CASMO5, the energy spectrum can be divided into the following energy group (EG) numbers: 2, 3, 4, 8, 19, 35, 95, 306, and 586. For this study, energy group numbers ranging from 8 to 586 were investigated, with the P_N scattering order initially set to 0.

Figure 3.6(a) illustrates the reactivity difference as a function of the energy group number for three FA configurations. For configuration 1 (without control rods), the reactivity difference remained below 200 pcm regardless of energy group numbers. However, for configurations 2&3 (with control rods), energy group numbers of 8, 19 and 35 result in larger errors in reactivity calculations. As the number of energy

groups increases, the continuous spectrum approximation improves, leading to a smaller difference from the reference solution. This suggests that the presence of a control rod, a strong absorber, will decrease the accuracy of CASMO5 if the energy group number is chosen improperly. Notably, beyond 95 energy groups, the reactivity differences for all configurations stabilize and show minimal deviation.

Figure 3.6 (b) presents the calculation time required by CASMO5 increases with the energy group number, especially between 35 and 586 energy groups. Considering the minimal improvement in reactivity accuracy beyond energy group number 95 and the corresponding increase in calculation time, an energy group number of 95 was chosen for subsequent studies. This choice effectively balances the requirement for calculation fidelity with the computational efficiency.

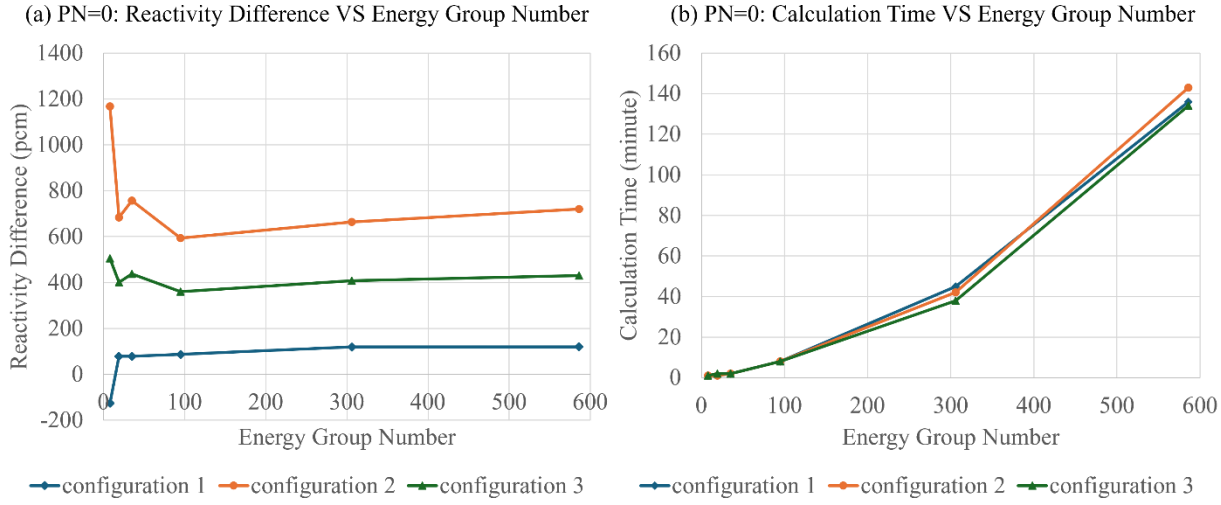

Figure 3.6 P_N=0: Reactivity difference and calculation time change with energy group number for various fuel assembly configurations under HFP

With the optimal 95 energy groups determined, the resulting pin power distributions were subsequently compared against the most energy groups available in CASMO5, 586 energy groups. Figure 3.9 presents the detailed comparison in a heatmap format, displaying the pin power values for 586 energy groups (Top), 95 energy groups (Middle), and their corresponding relative difference (%) (Bottom) for the three configurations, which is calculated with (3.14).

$$Relative\ difference\ (\%) = \left(\frac{Pin\ Power_{586grp} - Pin\ Power_{95grp}}{Pin\ Power_{95grp}}\right) \times 100\% \qquad (3.14)$$

The results demonstrate a remarkable consistency between the two energy groups numbers. For majority of pins, the normalized pin power values are identical when truncated to three decimal places, resulting in a relative difference of 0.00%. Few pins exhibit non-zero differences, highlighted by the black boxes. The largest observed relative difference of pin power across all three configurations is -0.23%, which is found in configuration 3, pin [5,8]. This minimal difference confirms that the selected 95 energy groups provide sufficient accuracy for pin power distribution calculation in the lattice model.

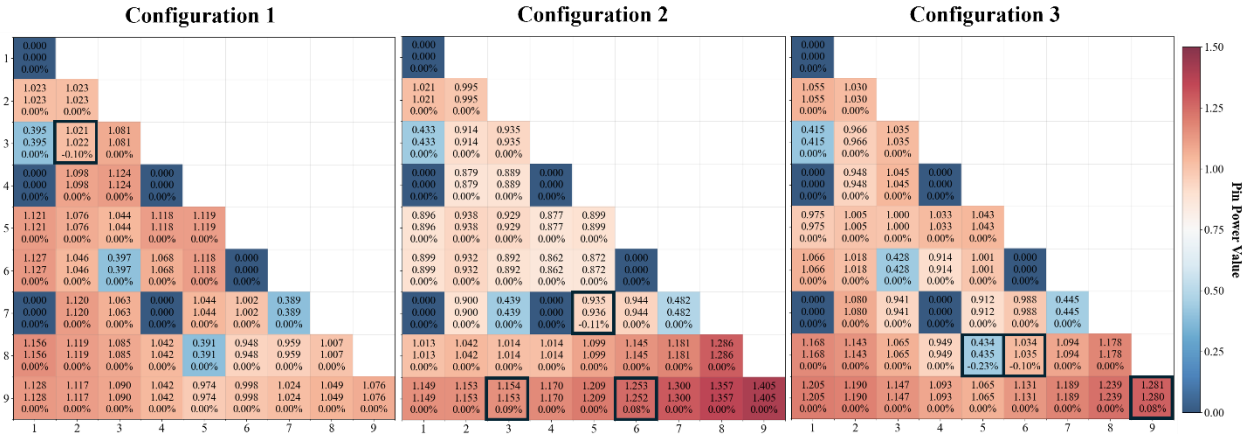

Figure 3.7 Comparison of normalized pin power distributions for three configurations with energy group number of 586 and 95 and relative difference (%)

3.5.1.2 Impact of the P_N-scattering Order in 2D Transport Flux Solution

Following the energy group analysis, the impact of P_N scattering order was investigated. In CASMO5, the P_N-scattering order was changed from 0 to 1, 2, 3, 4, 5 and the default value is 0.

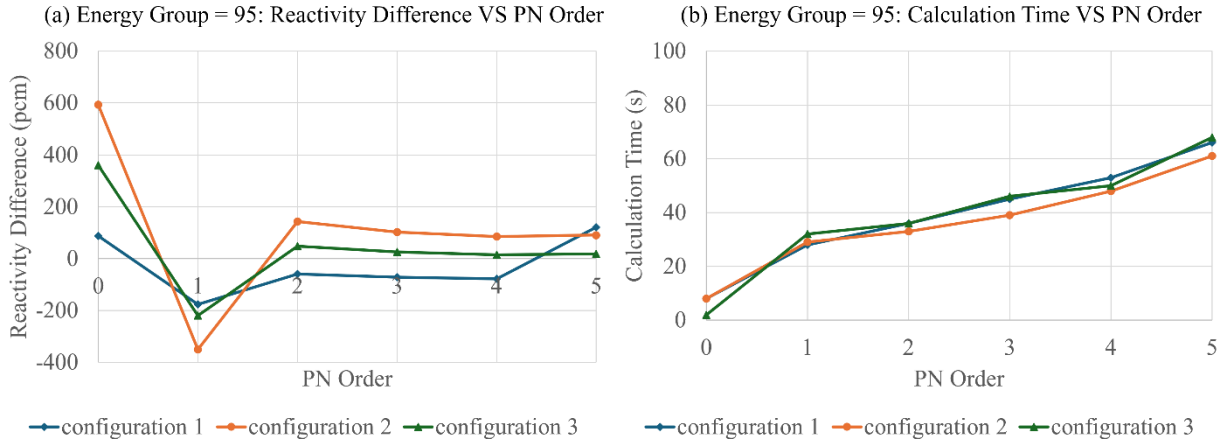

Figure 3.8 Energy group=95: Reactivity difference and calculation time change with P_N scattering order for various fuel assembly configurations under HFP

Figure 3.8(a) illustrates the reactivity difference predicted by CASMO5 and SERPENT2 depending of the P_N-scattering order with the verified 95 energy groups employed. The results clearly demonstrate that the P_N=0 approximation is only accurate for configurations without control rods (Configuration 1). Its limitations become very apparent when the P_N order is low (1 and 2) and control rods are present, leading to large reactivity differences. Beyond a P_N order of 3, the reactivity differences for all configurations stabilize and show minimal further change.

Figure 3.8(b) shows the calculation time required by CASMO5 increases with the P_N scattering order, with calculation time significantly increasing from P_N=0 to P_N=5. Considering the minimal improvement in

reactivity accuracy beyond P_N=3 and the corresponding increase in calculation time, a P_N scattering order of 3 was selected as optimal for cross-section generation.

With the optimal P_N=3 scattering order selected, the resulting pin power distributions were subsequently compared against the highest P_N order available in CASMO5, P_N=5. Figure 3.9 presents the detailed comparison in a heatmap format, displaying the pin power values for P_N=5 (Top), P_N=3 (Middle), and their corresponding relative difference (%) (Bottom) for the three configurations, which is calculated with (*3.15*).

$$Relative\ difference\ (\%) = \left(\frac{Pin\ Power_{PN=5} - Pin\ Power_{PN=3}}{Pin\ Power_{PN=5}}\right) \times 100\% \qquad (3.15)$$

The results demonstrate a remarkable consistency between the two P_N orders. For majority of pins, the normalized pin power values are identical when truncated to three decimal places, resulting in a relative difference of 0.00%. Few pins exhibit non-zero differences, highlighted by the black boxes. The largest observed relative difference of pin power across all three configurations is -0.11%, which is found in configuration 2, pin [6,3]. This minimal difference confirms that the selected P_N scattering order of 3 provides sufficient accuracy for pin power distribution calculation in the lattice model.

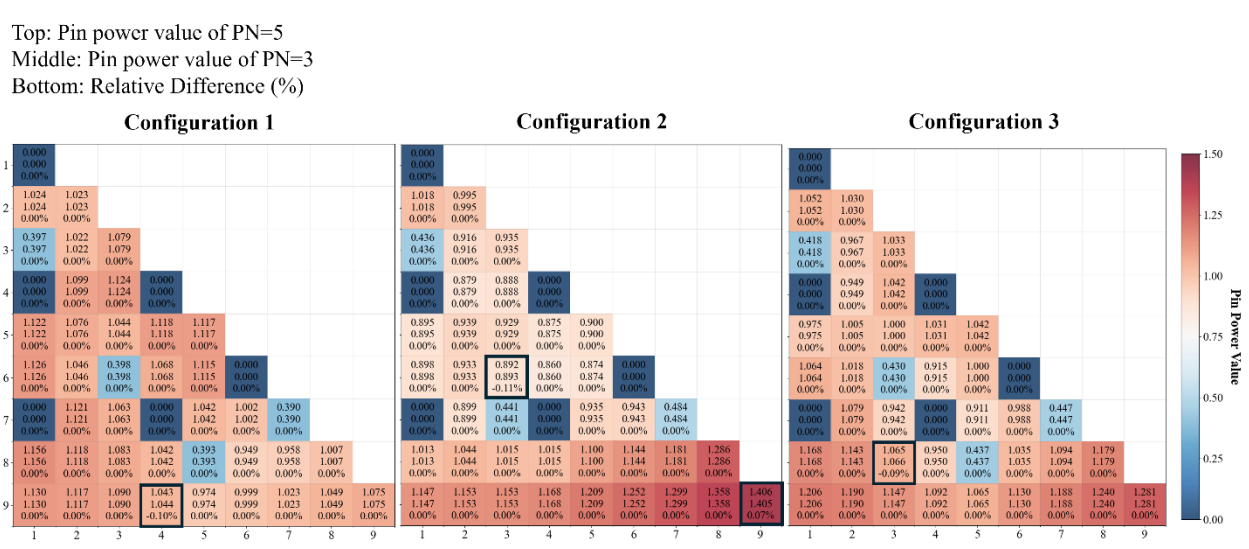

Figure 3.9 Comparison of normalized pin power distributions for three configurations showing P_N=5, P_N=3 and relative difference (%)

Based on the parametric analysis of CASMO5's FA models across the three configurations, results obtained with 95 energy groups and a P_3 scattering order yields an accurate prediction of reactivity, with the resulting reactivity difference falling within an acceptable deviation of ±200 pcm compared to the reference solution. Moreover, this parameter set maintains a comparably short computational time, effectively balancing accuracy with efficiency. Furthermore, the simulated pin power distribution differences are constrained below ±0.23%, confirming the spatial accuracy. Therefore, the parameter combination with 95 energy groups and a P_3 scattering order can be used in the subsequent cross-section generation for core simulation.

3.5.2 Assessment of SIMULATE5 for Core Simulations against SERPENT2

To align with SERPENT2, which is a neutronics code, the TH module is deactivated in SIMULATE5 for this assessment. Instead of dynamic feedback, the average temperatures for fuel and moderator are applied to ensure consistent conditions for comparison.

3.5.2.1 Core Benchmark Description

Following the parametric study in CASMO5, the optimal settings are applied to generate cross sections for SIMULATE5 core simulations. The core loading (Figure 3.10) comprises four types of fuel assemblies with varying fuel enrichment, BA rods number per FA and BA loading. The core also incorporates with control rods, which are composed of either Silver-Indium-Cadmium (Ag-In-Cd) or a hybrid of Ag-In-Cd and stainless steel. In the fuel assemblies without CRs (white blocks), the guide tubes are entirely filled with flowing water. In these simulations, the radial and axial reflectors are assumed as consistent water.

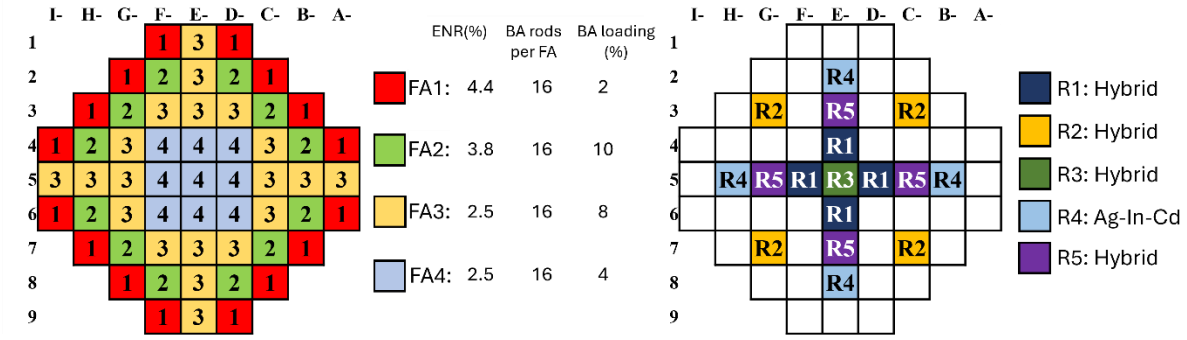

Figure 3.10 Core model benchmark for the assessment of SIMULATE5 against SERPENT

The objective of this assessment is to confirm the effectiveness of SIMULATE5 in core simulations, using SERPENT2 as the reference. The assessment specifically focuses on the core eigenvalue (k_{eff}) and core's radial power distribution.

3.5.2.2 Core Eigenvalue Assessment

As presented in Table 3-3, the reactivity differences between SIMULATE5 and SERPENT2 are within 200 pcm for various states (CZP/HZP/HFP) both when all control rods out (ARO) and when all control rods inserted (ARI), confirming SIMULATE's accuracy in calculating the eigenvalue under various conditions.

Table 3-3 Assessment results of core eigenvalue for CZP/HZP/HFP

States	Control rods in/out	k_{eff} SIMULATE5	k_{eff} SERPENT2	Reactivity difference (pcm)
CZP	ARO	1.15552	1.15733	-135
	ARI	1.10843	1.10977	-109
HZP	ARO	1.07372	1.07355	15
	ARI	1.01494	1.01430	62
HFP	ARO	1.05203	1.05137	60
	ARI	0.99133	0.98970	166

3.5.2.3 Assessment of the Axially-averaged Radial Power Distribution

Figure 3.11 displays a comparison of axially-averaged radial power (RPF) profiles under CZP conditions from SIMULATE5 and SERPENT2, for both ARO and ARI configurations. The colour bar on the right indicates the RPF calculated by SERPENT2, ranging from blue (lowest value 0.0) to red (highest value 1.5). The results demonstrate consistent spatial power distribution. SIMULATE5 accurately captures peak power locations and magnitudes with minor numerical deviations. For ARI condition, SIMULATE5 effectively shows the power suppression in the regions where control rods are inserted, consistent with SERPENT2. This close agreement indicates that SIMULATE5 can capture the spatial power generation and control rod impact within the core.

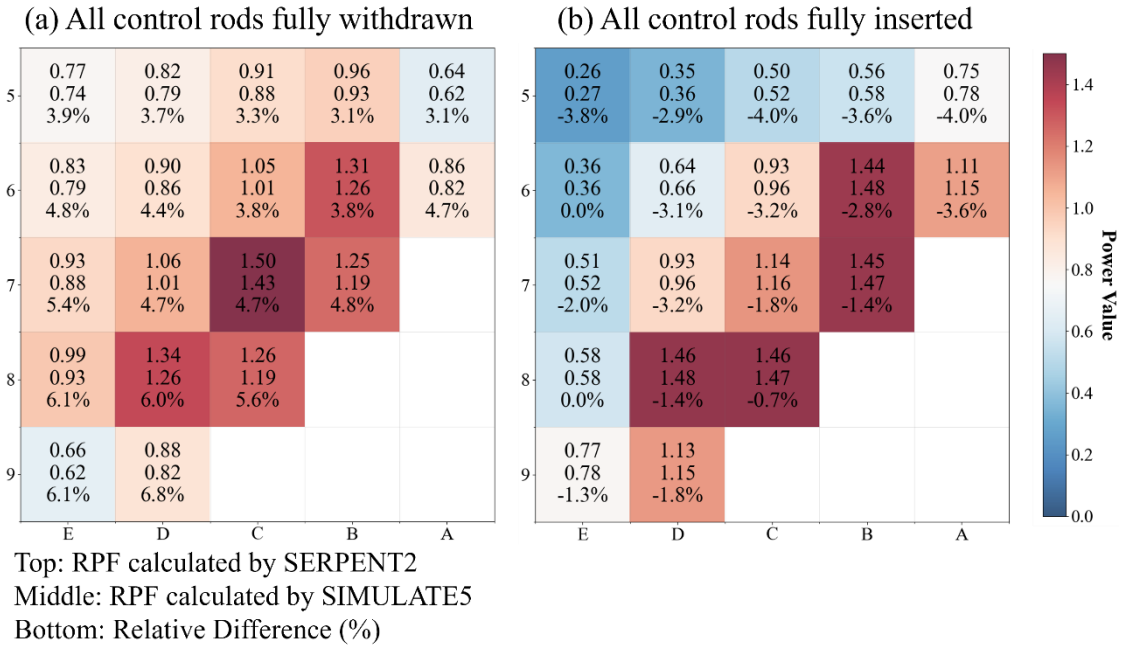

Figure 3.11 Radial power profiles comparison of ARO/ARI under CZP

This consistency observed in both global (k_{eff}) and local (radial power) parameters confirms the effectiveness and reliability of the SIMULATE5 core model for subsequent analyses.

4 Core Design Methodology

The design of an SBF SMR core is a complex task due to many adjustable parameters. To effectively manage this complexity, the methodology begins by identifying and fixing certain parameters. The remaining parameters are then treated as variables within the optimization process. Subsequently, the process involves searching a large variable space and requires extensive repetitive simulations. Therefore, the in-house tool CoreOptimizer is applied to streamline the workflow of CASMO5 and SIMULATE5, minimizing manual errors while efficiently exploring the variable space. Notable, the methodology

distinguishes between two operational phases: the first-cycle and equilibrium-cycle core. Each phase requires different core loading patterns to meet the long-term safety objectives.

4.1 Core Design Constraints

The core design process involves a substantial degree of freedom across various parameters, spanning multiple levels. At the core level, key parameters include the total number of fuel assemblies, the FA radial arrangement (Core loading), the number and radial layout of control rods, and the associated control rod withdrawal strategies. At the fuel assembly level, design variables encompass geometric specifications, such as the number diameters of fuel, burnable absorber, and control rod pins, along with the pin pitch, FA pitch and active fuel length. Furthermore, the material properties must be determined, including the fuel enrichment, the burnable absorber concentration and material, and the control rod material. In addition, the core design involves specifying the material and thickness of reflector components. Finally, the operating conditions must be considered, including thermal power, coolant flow rate, system pressure, and the inlet coolant temperature.

As described in Section 1.2.5, the total fuel assembly number is 57 in the core, as shown in Figure 1.2. However, the FA radial arrangement, control rod number, layout and withdrawn strategy remain as parameters to be determined. At the fuel assembly level, the materials and diameters of all pins are detailed in Table 1-1. Specifically, each assembly contains 24 control rod guide tubes, which can be configured with either 12 Ag-In-Cd pins and 12 stainless-steel pins, or 24 Ag-In-Cd pins. Additionally, *Figure 1.4*illustrates the FA configurations with different burnable absorber pins. The pin pitch, FA pitch and operating conditions are summarized in Table 1-3. However, the fuel enrichment, the burnable absorber concentration and the burnable absorber rod number in each fuel assembly are to be determined.

To manage the complexity and ensure the feasibility of the core design process, certain parameters are further constrained. Although the core loading patterns and control rod withdrawal strategies are variables, including them in the design process introduces excessive computational effort. Consequently, based on established fuel management strategies, the core loading patterns for both the first and equilibrium cycle are fixed. Similarly, specific strategies for control rod withdrawal are applied. This section will introduce the fixed core loading patterns and the established control rod withdrawal strategies.

4.1.1 Core Loading Strategies

Core loading pattern differs between first-cycle (start-up) and equilibrium-cycle cores, with the specific considerations detailed in Section 2.3.2.1 and Section 2.3.2.3, respectively.

The first-cycle core loading pattern in this study is illustrated in Figure 4.1: The core is divided radially into four FA zones. The FA1 zone, located at the periphery, contains fuel with the highest enrichment with relatively low burnable absorber loading. Moving inward from FA1 to FA4, the fuel enrichment is gradually reduced while the BA loading is progressively increased.

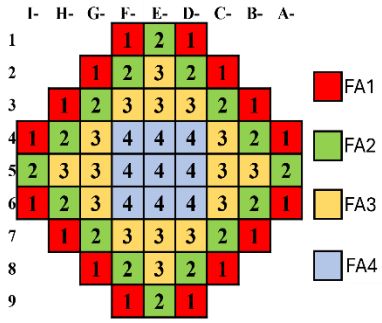

Figure 4.1 Radial fuel loading pattern for the first-cycle core

However, determining the appropriate loading pattern for an equilibrium core is more complex. As discussed in Section 2.3.2.3, 2-batch and 3-batch refueling strategies are the most common choices for light-water SMRs. For the objective core of only 57 FAs, 2-batch refueling scheme involving 29 fresh FAs in each cycle ensures a smaller power gradient compared to a 3-batch scheme, which involves only 19 fresh FAs in each cycle. Therefore, the 2-batch refueling strategy was selected for this study due to the balance of refueling frequency and power distribution uniformity.

Figure 4.2 shows the refueling loading pattern applied in this study, with radial multi-zones. The objective core consists of 29 fresh FAs and 28 once-burned FAs. The refueling strategy contains the following features: The fresh assemblies are radially divided into four zones (FA1, FA2, FA3 and FA4). The outermost layer of the core contains a mixture of 16 fresh and 4 once-burned FAs. The once-burned fuel assemblies are moved to adjacent inner positions during refueling, and their locations in the last cycle is marked in white blocks to track their movement. A key feature of this refueling loading pattern is that all fresh fuel assemblies are not adjacent to each other, mitigating excessive local power peaking. Furthermore, the central fuel assembly FA4 is replaced during each refueling.

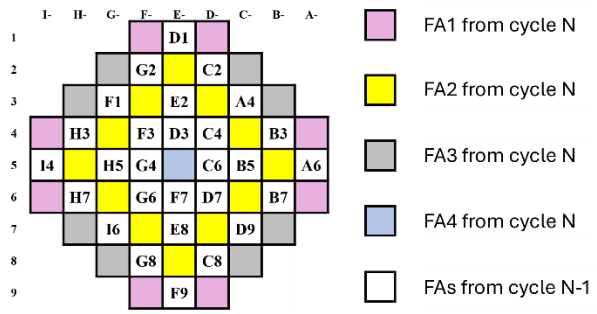

Figure 4.2 Refuelling loading pattern to reach the equilibrium-cycle core

4.1.2 Strategies for Defining the Control Rod Layout

All control rods are axially homogeneous, meaning their composition is uniform along their length. As illustrated in Figure 1.3, the regulating banks are equipped with hybrid rods (Ag-In-Cd and SS) to mitigate axial power peaking during operation; The safety banks are made of Ag-In-Cd rods to ensure sufficient shutdown margin.

The control rod radial layout will be determined during simulations according to the following three factors:

- Power distribution: Control rod movements must maintain a relatively uniform radial and axial core power distribution, keeping the peak power factors within safety limits.
- Excess reactivity control: The regulating banks must compensate the excess reactivity throughout the operational cycle, ensuring the core operates under critical conditions.
- Shutdown margin: The control rod banks should provide a sufficient shutdown margin, ensuring the core can be shut down to a subcritical state under any scenario.

During the simulations, SIMULATE5 searches for the axial positions of the control rods according to the user-defined settings. In this investigation, the control rods are set to move 0.5cm each step. Because the core is 200-cm high, a full insertion or withdrawal requires 400 steps. And the constants overlapping between control rods groups is 50%, which means R2 begins its insertion when R1 is halfway through its maximum insertion; similarly, R3 starts its insertion when R2 is halfway through its maximum insertion; and so on. The convergence criteria for the critical simulations are set to $0.99985 < k_{eff} < 1.00015$, ensuring the core operates under a critical condition with acceptable deviation.

4.2 Parameters to be Determined

With several core parameters and conditions fixed, the focus shifts to the remaining variables to be determined, including the fuel enrichment (ENR), the BA-rod number per assembly and Gd_2O_3 concentration in BA-rod. The approach begins with analyzing individual fuel assemblies (FAs) to evaluate reactivity trends, which then guides the selection of parameter combinations for core design optimization.

4.2.1 Single Fuel Assembly Burnup Analysis with Varying Enrichment

Firstly, single lattice models of the FA-design shown in Figure 1.3 were simulated using CASMO5. These simulations were conducted with varying fuel enrichment and without any burnable absorbers. These 2D lattice simulations were conducted with reflective radial boundary conditions at averaged fuel and coolant temperatures of 900K and 590K, respectively.

Figure 4.3 illustrates the resulting k_{inf} as a function of burnup for different enrichments. As shown, higher fuel enrichment leads to a higher k_{inf}. For all enrichments, k_{inf} decreases as the fuel burns up, and this reduction appears relatively linear.

The data in Figure 4.3 allows for the preliminary determination of the core-average enrichment. To achieve the targeted cycle length of 2 years, corresponding to a cycle burnup of 21GWd/t, the core-average k_{inf} must remain above unity at the end of cycle. Based on the results in Figure 4.3, reaching 21GWd/t with k_{inf} >1.0 necessitates an enrichment of approximately 3.0%. By establishing this narrow range for the core-average enrichment, the enrichment search space is significantly reduced. This approach mitigates the extensive computational effort that would otherwise be required if enrichment were treated as a fully unrestrained variable in the core-level simulation.

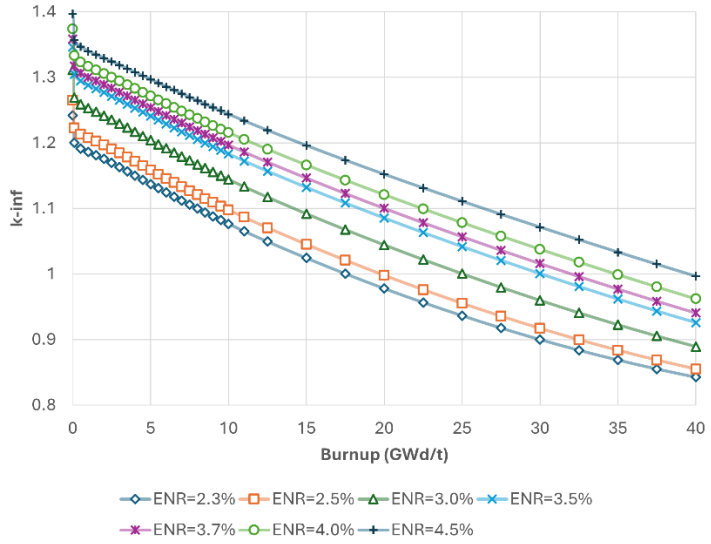

Figure 4.3 k_{inf} changing with burnup in the lattice models

4.2.2 Single Fuel Assembly Burnup Analysis with Various Burnable Absorber Designs

Following an investigation of fuel assembly behaviour without BAs, the depletion behaviour of FAs with different BA rods per FA and BA loading was evaluated using CASMO5.

Figure 4.4(a) illustrates the effect of the number of Gd rods per FA on the k_{inf} as a function of fuel burnup in the assemblies with fixed 3.5% enrichment and fixed Gd_2O_3 weight percentage of 8%. As shown, Gd effectively suppresses the reactivity at beginning of cycle (BOC). A larger number of Gd rod per assembly leads to a stronger initial suppression, resulting in a lower starting point for the k_{inf} curve.

Figure 4.4(b) analyses the effect of Gd_2O_3 concentration in lattice models with a fixed 3.5% ^{235}U enrichment and 16 Gd rods per FA. The results show that a greater the Gd_2O_3 concentration in the BA-rod leads to a larger the decrease in the peak k_{inf} and a shift of the peak to a higher burnup. The underlying mechanism if the spatial self-shielding effect of Gd, which intensifies as the concentration increases. Higher concentration

causes the neutrons to be absorbed by Gd near the surface of the rods, leaving the inner-layer Gd to deplete more slowly due to a lower thermal flux.

The comparison between Figure 4.3 and Figure 4.4 demonstrate that gadolinium (Gd) serves as an effective BA for initial reactivity suppression. The degree of this suppression is highly dependent on three factors: the fuel enrichment, the number of Gd rods, the Gd loading. For instance, the results presented in Figure 4.4 indicates that for a fixed 3.5% enrichment, FA configurations employing 16 Gd rods combined with Gd_2O_3 loading of 8% or 10% are highly favourable because they flatten the reactivity over a longer operational duration. Therefore, the allowable range for these two Gd parameters is narrowed and cantered around these favourable values for the subsequent parameter search process, allowing their ranges to be significantly narrowed. By performing a similar analysis for all relevant enrichment values, the overall complexity of the core design search space is significantly reduced.

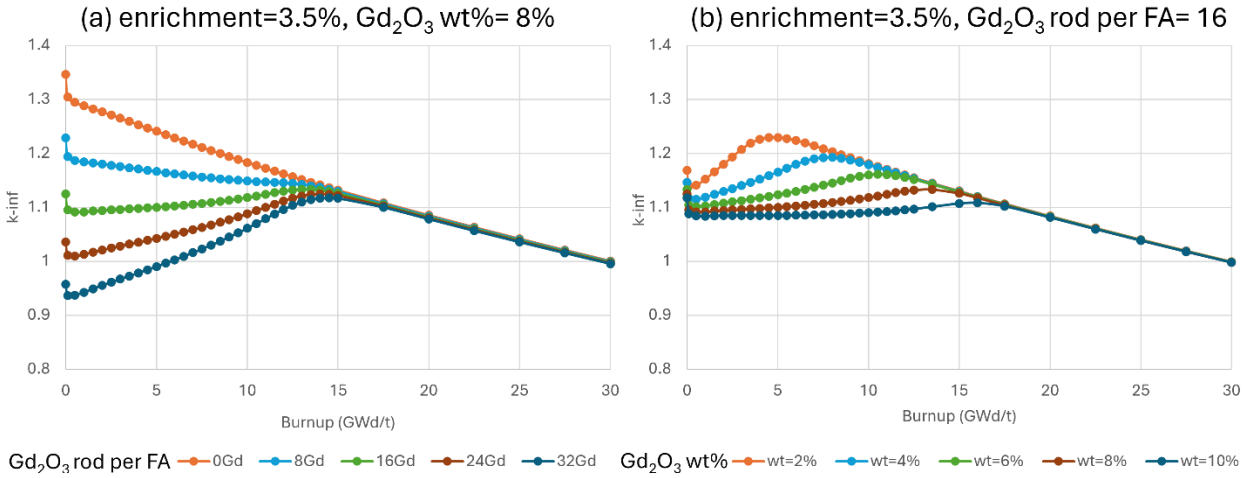

Figure 4.4 k_{inf} evolution versus burnup cycles for single FAs with BA numbers and BA loading

4.2.3 Search Ranges of Parameters for Core Optimization

The single FA simulations established the baseline for parameters search ranges determination, indicating that a core-average fuel enrichment over 3.0% is required to meet the target cycle burnup of 21 GWd/t. Furthermore, the BA parameters, including BA rod number and loading, must be constrained within certain ranges because they are in conjunction with fuel enrichment to manage the reactivity suppression throughout the operational cycle. Due to the ununiform neutron flux distribution within the core, accurately predicting the individual impact of each parameter on core behavior is unrealistic.

Therefore, the discrete search values for the three key parameters (fuel enrichment, BA rod number per FA and BA loading) are defined separately for the first-cycle and equilibrium-cycle cores. Based on the start-up core loading pattern and refueling strategies, the specific search ranges for these three parameters are subsequently determined, as discussed below.

The first-cycle core is a core composed entirely of fresh fuel assemblies. For each of the four FA types (FA1, FA2, FA3, FA4), the ranges of variables are defined with specific intervals, as detailed in *Table 4-1*. To reduce the power peak in core centre, the fuel enrichment decreases from outermost layer toward the innermost layer. Additionally, FA1, which is the outermost layer, is equipped with fewer BA rods per FA. As illustrated in Figure 4.4, to achieve a relatively flattened reactivity suppression for a longer duration, BA loading is fixed to 8% across all FA types.

This systematic combination generates 21 distinct lattice models for individual fuel assemblies. Since the core consists of four FA types, the total number of unique core configurations to be searched is calculated as the product of these combinations, yielding a total of 864 configurations.

Table 4-1 Combinations of discrete search values for the three key parameters of fuel assemblies at first-cycle core

Fresh FA-types	Enrichment (%)	BA rods per FA	BA loading (%)	Combinations
FA1	4.2, 4.4	12, 16	8	4
FA2	3.2, 3.4, 3.6	16, 24	8	6
FA3	2.6, 2.8, 3.0	12, 16, 20	8	9
FA4	2.2, 2.4	12, 16	8	4

For equilibrium core, the combinations of fuel assembly parameters are assigned based on the refueling loading pattern in Figure 4.2: FA1 (pink) and FA3 (grey) are primarily located in the outer-region positions of the core. They are characterized by higher enrichment with fewer BA rods. This strategy compensates for the lower neutron flux in peripheral regions, ensuring relatively uniform power distribution. FA2 (yellow) occupy the inner region. These FAs are assigned lower enrichment and additional BA concentration to control the power peak in the high-flux inner regions. The central assembly FA4 (blue) is assigned the lowest enrichment to minimize the central power peak.

Therefore, the range of variables for the four FAs are defined with specific intervals, as shown in *Table 4-2*. This systematic combination results in 30 lattice models. As the core consists of four FA types, the total number of core configurations is calculated as the product of these combinations, yielding 3456 configurations.

Table 4-2 Combinations of discrete search values for the three key parameters of fuel assemblies at equilibrium-cycle core

Fresh FA-types	Enrichment (%)	BA rods per FA	BA loading (%)	Combinations
FA1	4.8, 4.95	16, 20, 24	4, 8	12
FA2	4.0, 4.2, 4.4	28, 32, 36, 40	10	12
FA3	4.8, 4.95	16, 20, 24	4, 8	12
FA4	1.8	20, 24	8	2

4.3 Parameters Search Process

As previously established, the fundamental constraints have been defined, leaving the key variables to be searched as fuel enrichment, the number of burnable absorber (BA) rods per fuel assembly (FA), and Gd_2O_3 concentration in BA-rod (BA loading). The primary challenge lies in finding the optimized combination of

these variables for the multiple radial FA zones to achieve the target 24-month cycle length (corresponding to a cycle exposure of 20GWd/t) while satisfying all the current safety criteria. Following the determination of the search ranges for these key parameters, this investigation employs an exhaustive search approach. This methodology utilizes CASMO5 to generate the necessary cross-sections and subsequently uses SIMULATE5 to conduct the core simulations for the large number of potential combinations.

To systematically explore these numerous possibilities and identify the most promising core configurations, a brute-force search method was implemented in this investigation and a corresponding tool CoreOptimizer was developed to automate input file generation, simulation execution, output data extraction and results visualization.

4.3.1 Challenges of Traditional Two-Step Approach in Parameters Search Process

The conventional two-step approach requires manual effort for extensive input generation with different parameter combinations, execution of a large number of simulations, and output processing, making the entire workflow both time-consuming and prone to human error.

Consider a multi-cycle equilibrium optimization scenario involving variables such as fuel enrichment (A), the number of burnable absorber rods per fuel assembly (B), and burnable absorber loading (C). Assuming each fuel assembly has the same options and the core radial layout is fixed and the fixed fuel assembly types number is D, the sheer number of possible parameter combinations is $(A \times B \times C)^D$.

The process of achieving equilibrium state requires running each configuration across multi cycles (M). Moreover, each cycle requires a restart file from the previous cycle and a new, manually prepared input SIMULATE5 file. This means the total number of SIMULATE5 input files that must be generated and executed reaches $(A \times B \times C)^D \times M$.

Therefore, this workload involves manually entering parameters, executing commands, and verifying inputs for SIMULATE5 file for $(A \times B \times C)^D \times M$ times, which is not only prohibitively time-consuming but also highly susceptible to human error in parameter transcription and file management. These challenges severely restrict the designer's ability to explore a big core design parameter space.

4.3.2 Functions and Advantages of CoreOptimizer

To overcome these limitations, the CoreOptimizer tool was developed with a Graphical User interface (GUI). It is in Golang programming language to automate the conventional "two-step" approach by managing all phases: input file generation, simulation execution, output data extraction and results visualization.

CASMO5 Integration

Figure 4.5 illustrates the CASMO5 management interface within the GUI of CoreOptimizer. User can define the minimum, maximum, and interval values for target variables, such as fuel enrichment (Enrichment), burnable absorber number per FA(B5), BA loading (B6)). Using a pre-saved template where these variables are left vacant, CoreOptimizer automatically traverses all parameter combinations and generates CASMO5 input files by clicking "Start: create .inp files". Users can then specify the number of concurrent routines (How many CASMO5 input files are executed simultaneously) and execute all the input files by clicking "start: simulation of all .inp files".

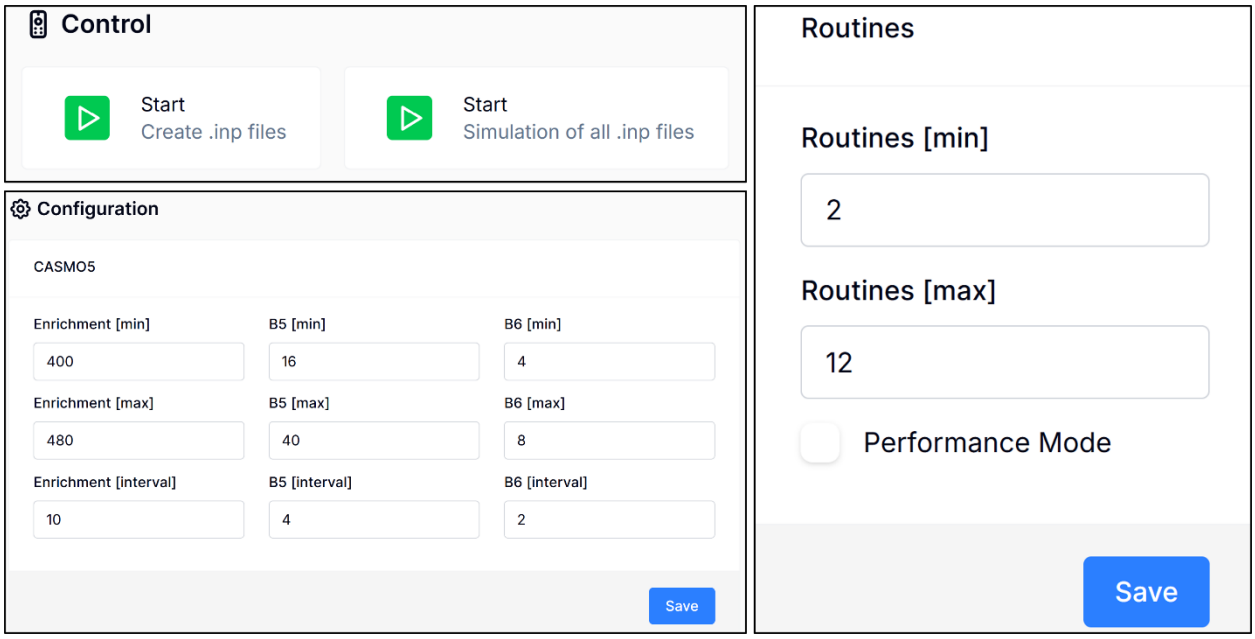

Figure 4.5 CASMO5 management interface within the GUI of CoreOptimizer

CMSLINK5 Integration

It consolidates all processed CASMO5 *.cax files from the specific folder into a unified library for subsequent SIMULATE5 utilization.

SIMULATE5 Integration

The process begins with user create a configuration through the graphic user interface (GUI). A configuration includes the following parameters:

- The cycle index, because SIMULATE5 executes and halts after each cycle, requiring explicit user input for the cycle number
- The fixed cycle length
- The ranges of key variables, specifically fuel enrichment, burnable absorber number per fuel assembly, and burnable absorber loading
- The selection criteria
- The SIMULATE5 input template, which include the boundary conditions, the fuel assembly loading pattern or refueling strategy, and control rod layout and withdrawal sequence.

CoreOptimizer receives these configuration data and generates SIMULATE5 input files with template and all the data. Then it runs SIMULATE5 command and awaits the completion of the simulation.

Upon simulation completion, CoreOptimizer reads SIMULATE5 output files and extracts the needed data, including the 3D and 2D peak pin power and the power axial offset at all the simulated state-points. These extracted data are then checked against the user-defined selection criteria.

A storage protocol is implemented: If all criteria are met, the SIMULATE5 files (*.out, *.sum, *.res) are stored; if not, these SIMULATE5 files are deleted to conserve disk space because each output file can reach 1.4 MB with a restart file up to 350 MB. Crucially, regardless of whether the files are stored or deleted, the job processing statistics are always saved.

To handle the significant computational load associated with the brute-force search, CoreOptimizer incorporates a job scheduler that facilitates concurrent processing. The system contains a job list (j_1, j_2, …, j_n) corresponding to the configurations that require to be processed. The user utilizes the GUI to define the number of concurrent threads that the system uses.

The job scheduler assigns jobs (j_1, j_2, …, j_n) to the available processing cores of the computer, allowing them to execute simultaneously. As each concurrent job is completed, the scheduler immediately processes the output, extracting the user-defined data from output file, and compare them with the selection criteria. This concurrent execution of jobs drastically reduces the overall simulation time required for the exhaustive search.

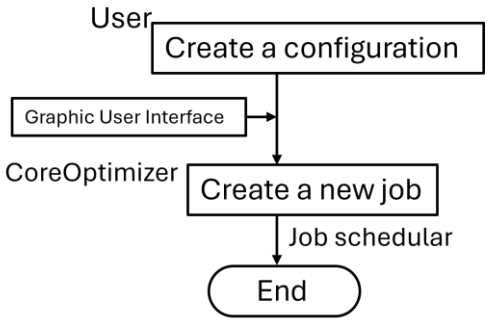

Figure 4.6 Workflow of CoreOptimizer integrated with SIMULATE5

4.3.3 Parameters Search Process of First-Cycle Core

The parameters search process for first-cycle core is accomplished through a multi-stage selection methodology (Y.Song and Sánchez-Espinoza, 2026). The process begins with all control rod out (ARO) simulations to eliminate the influence of control rod movements. The results obtained from ARO simulations subsequently guide the decisions regarding the control rod layout in the core. Following this, the determined control rod movement sequences are applied to all core configurations and these

configurations are re-simulated under critical conditions. This step is to identify the configurations that satisfy all defined safety criteria while maintaining a targeted cycle length.

1) ARO Simulations

Firstly, a total of 864 core configurations were generated and simulated under ARO conditions. The key parameters, including the maximum effective neutron multiplication factor (k_{eff}) and the maximum 3D pin power factor (F_q) throughout the cycle, as well as the longest-reached cycle exposure, were collected for each configuration and are presented in Figure 4.7.

The scatter plot reveals a clear inverse correlation between the maximum k_{eff} and the maximum F_q for the simulated first-cycle core configurations. The Maximum F_q varies across the configurations from 1.98 to 3.39, while the maximum k_{eff} across the configurations range from 1.031 to 1.085. The color difference indicates the longest-reached cycle exposure of each configuration, ranging from very short (0 or 0.1 GWd/t, shown in dark blue) to longer exposures (16 to 20GWd/t, shown in shades of pink and red). The configurations with very short exposures are those with insufficient initial reactivity ($k_{eff} < 0$) to sustain a chain reaction.

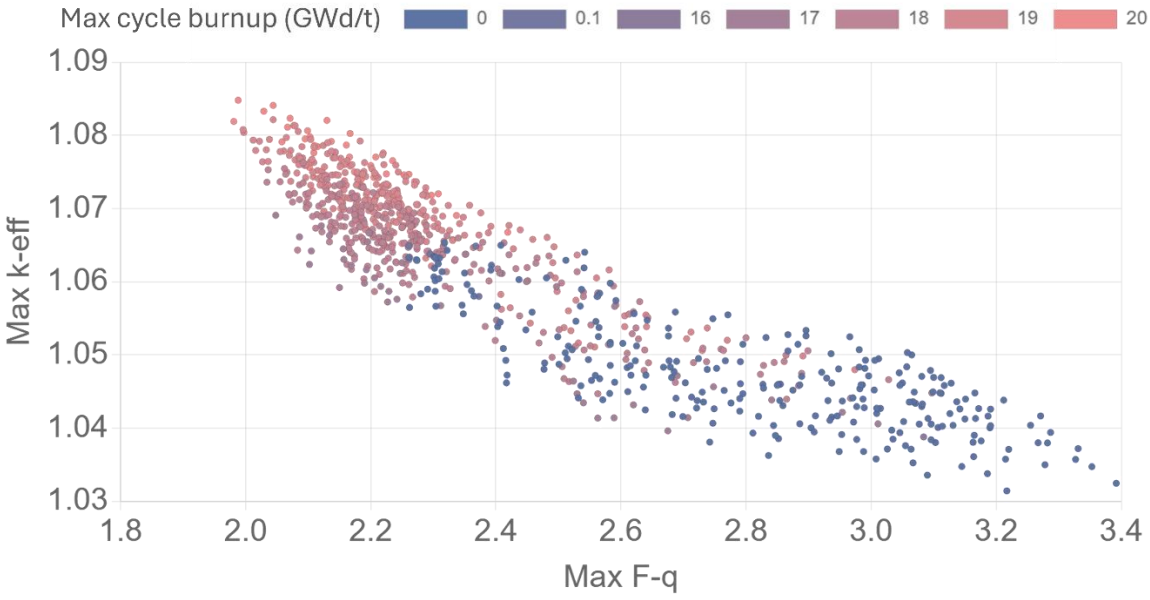

Figure 4.7 Scatter plot of ARO simulation results: Maximum k_{eff} vs. Maximum F_q vs. Cycle burnup

2) Control Rod Layout Determination

CoreOptimizer provides the capability for iterative search repetitions, allowing for evaluation of various CR layouts when the optimal configuration is uncertain. Multiple CR layouts were simulated under critical conditions for the first-cycle configurations, each fixed at 21 GWd/t burnup.

All configurations are assessed against the selection standards derived from the international safety criteria, which was collected in 2.5.1, detailed as follows:

1) $F_q \leq 3.26$

2) $F_{\Delta H} \leq 1.62$

3) -0.4≤Axial offset≤0.4

4) FTC<0

5) MTC<0

Following the application of these constraints, some CR layouts retained no configurations, indicating their unsuitability for this core design. Ultimately, two control rods are selected for further comparison, as illustrated in Figure 4.8. Each layout comprises four regulating banks (R1–R4) and two safety banks (S1, S2). The regulating banks are equipped with hybrid control rods (12 Ag-In-Cd + 12 Stainless Steel) designed to mitigate axial power peaking, see Figure 4.8. The safety banks, conversely, consist solely of Ag-In-Cd rods to ensure sufficient shutdown margin.

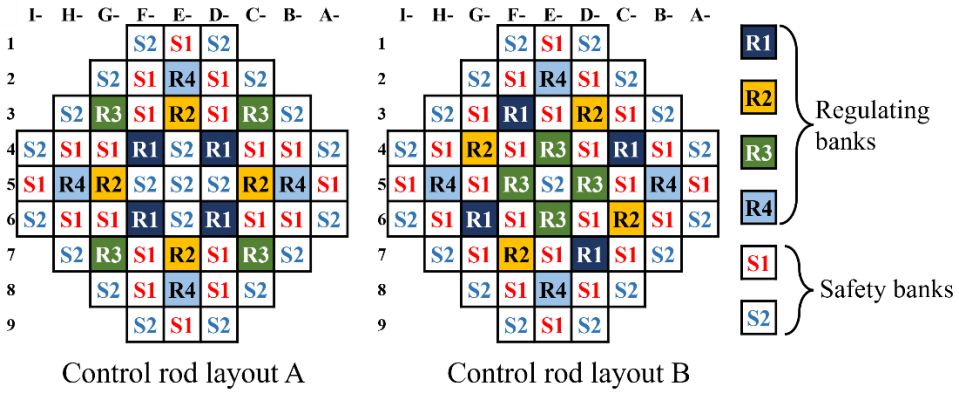

Figure 4.8 Two control rod layouts for first cycle simulations

3) Critical Search

Subsequently, the determined control rod movement sequences are applied to all the core configurations. Each configuration is then re-simulated under critical conditions with a fixed cycle length 21GWd/t. As discussed in Chapter 2.5, the specific set of safety criteria are developed corresponds to DiD level 1 in Table 2-1, to ensure normal reactor operation and avoid abnormal operation. CoreOptimizer collected all the results and these safety criteria were applied over the entire cycle:

1) $F_q \leq 3.26$

2) $F_{\Delta H} \leq 1.62$

3) -0.4≤Axial offset≤0.4

4) FTC<0

5) MTC<0

After applying these selection filters, 66 core configurations remained for regulating banks A (Figure 4.9) and 78 configurations remained for layout B (Figure 4.10). All the remaining configurations satisfy all the current safety criteria during normal operation. The significant reduction of F_q is observed between 6 and 10 GWd/t for most configurations, which can be explained by the control rod movements. As illustrated in

Figure 4.8, four regulating banks are utilized to manage reactivity. For most core configurations, from 0 to 6 GWd/t, two banks are maintained in a partially inserted position while the other banks are either one or two fully inserted. From 6 GWd/t to 10 GWd/t, only one control rod group remains partially inserted, with all other groups fully inserted. This transition induces a significant reduction in the axial peak power, and in turn reduces the 3D peak pin power F_q. This behavior is characteristic of SBF cores, where the power uniformity is highly sensitive to control rod positions and insertion depth.

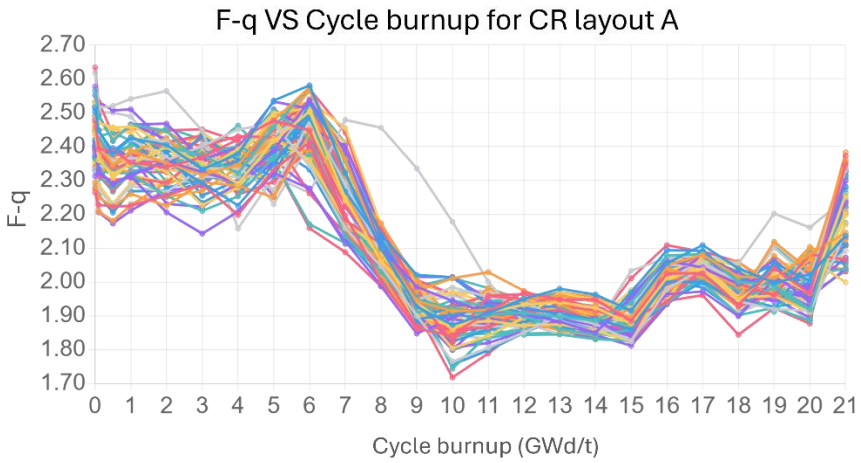

Figure 4.9 F_q throughout the cycle of the remaining configurations after safety selection filter for CR layout A

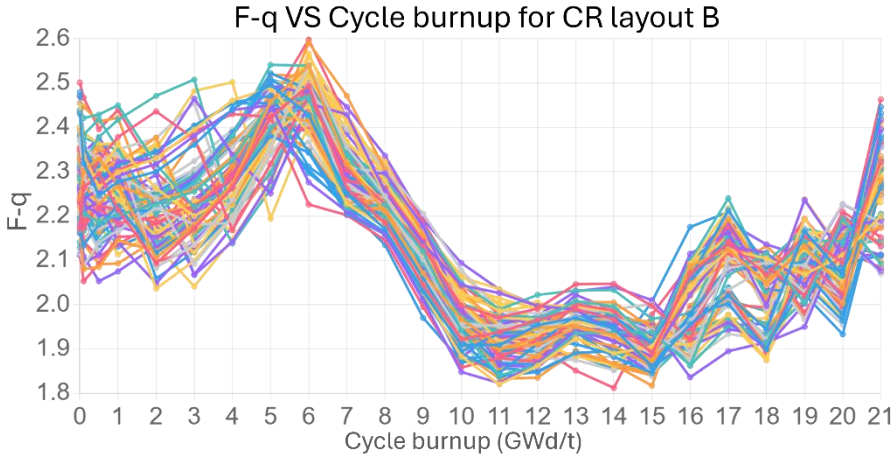

Figure 4.10 F_q throughout the cycle of the remaining configurations after safety selection filter for CR layout B

To better filter the optimized option, a series of stricter selection criteria are applied to the remaining configurations:

1) $F_q \leq 2.5$
2) $F_{\Delta H} \leq 1.50$
3) -0.4≤Axial offset≤0.4
4) FTC<0
5) MTC<0

The F_q for the remaining filtered core configurations throughout the cycle are displayed in Figure 4.11 and Figure 4.12. Among these options, the ones with CR-layout-A and CR-layout-B that exhibit the smallest peak F_q across the entire cycle were ultimately chosen as the optimized first-cycle core configurations for each control rod layout, as listed in Table 4-3. This prioritization of the lowest peak 3D pin power maximizes the operational safety margin, which is important in reactor core safety. The comparison of these two configurations with CR layout A and B will be discussed in the next Chapter.

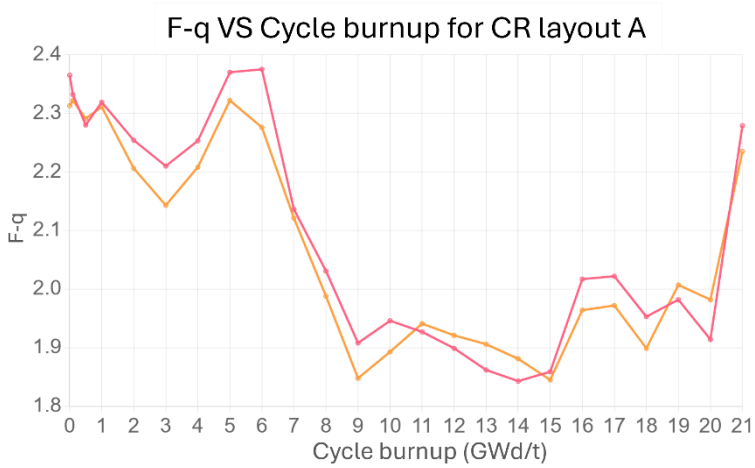

Figure 4.11 F_q throughout the cycle of the remaining configurations after stricter selection filter for CR layout A

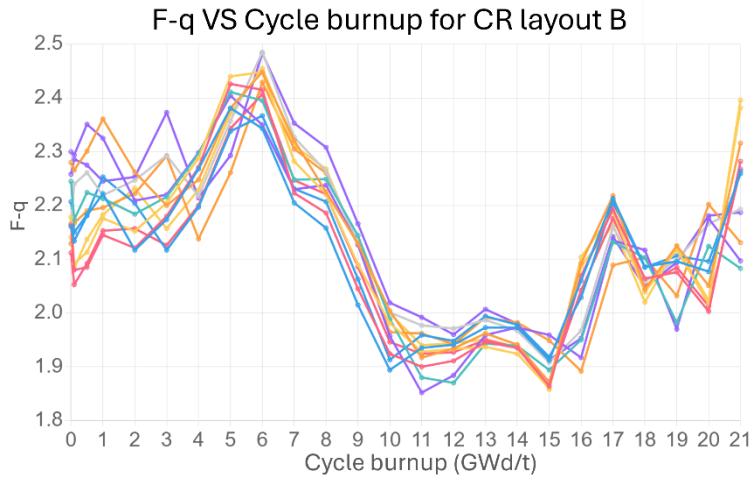

Figure 4.12 F_q throughout the cycle of the remaining configurations after stricter selection filter for CR layout B

Table 4-3 Optimized core configurations for first cycle

Configurations	FAs	Fuel enrichment (%)	BA number per FA	BA loading (%)
CR layout A	FA1	4.2	16	8
	FA2	3.4	20	8
	FA3	3.0	12	8
	FA4	2.4	12	8
CR layout B	FA1	4.2	12	8
	FA2	3.4	20	8
	FA3	3.0	16	8
	FA4	2.4	12	8

The control rod movements for both configurations follow a predetermined sequence throughout the cycle. Specifically, the insertion sequence is defined by banks R1, R2, R3 and R4, while the withdrawal sequence is the reverse R4, R3, R2 and R1. According to this sequence, SIMULATE5 searches for the critical control rod positions at each state-point. For CR layout A and B, the movement trends are similar, as illustrated in Figure 4.13.

- Overall, the control rods are gradually inserted from 0 to 8GWd/t, and then withdrawn from 8 to 21GWd/t.
- R1 remains fully inserted until it begins to be withdrawn at 17GWd/t.
- R2 also stays almost fully inserted until it starts to be withdrawn at 14GWd/t
- For the majority of the cycle, R3 and R4 are partially inserted to prevent significant axial power shifts.

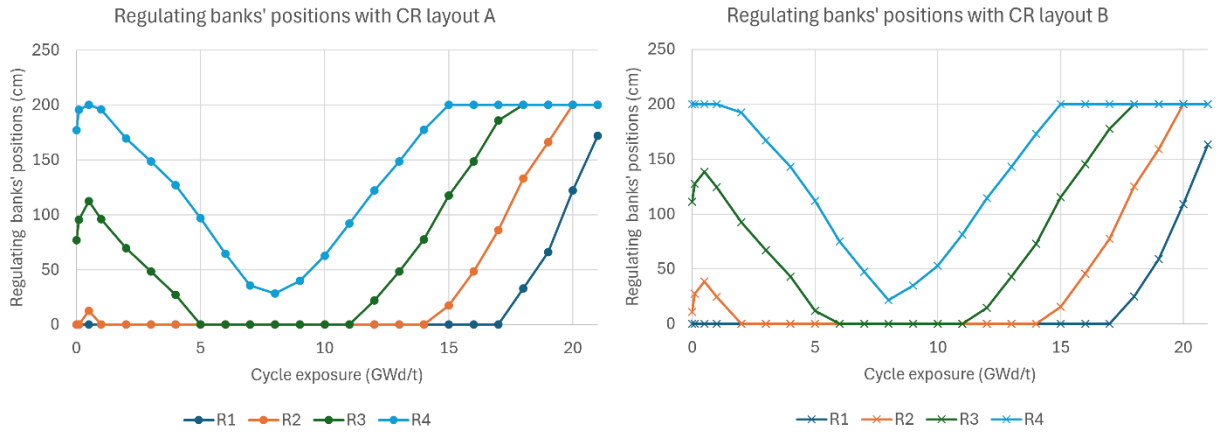

Figure 4.13 Regulating control rod banks' positions throughout the first cycle

4.3.4 Parameters Search Process of Equilibrium-Cycle Core

The design of the equilibrium core utilizes the same brute-force approach as the first-cycle design, employing the CoreOptimizer tool in conjunction with CASMO5 and SIMULATE5 with a multi-stage selection process (Y.Song and Sánchez-Espinoza, 2025). This process also begins with an ARO search to guide the control rod layout decisions. Moreover, the ARO simulations are repeated for multiple cycles with a fixed cycle length until the ARO equilibrium is reached when the k_{eff} difference between adjacent cycles is less than 1%. Once the control rod layout is determined, the simulations then proceed under critical conditions for extra multiple cycles, with each cycle having a fixed cycle length, a consistent refueling strategy, and consistent new fuel assemblies as last cycle. The safety parameters throughout the equilibrium cycle are subsequently compared against the safety criteria to identify the configurations that satisfy all defined safety criteria while maintaining a targeted cycle length.

1) ARO Search

The selected first-cycle core configuration (CR layout B in Table 4-3) is simulated under ARO condition to 21GWd/t. From cycle 2 onward, the core follows the same refueling strategy, with CoreOptimizer generating multiple SIMULATE input files by reading FA segments from the *.lib file. The core radial layout is fixed, applying distinct FA types FA1, FA2, FA3 and FA4. These segments contain data on enrichment, BA rods per FA and BA loading for each cycle.

For cycle 2, 3456 core configurations were generated and evaluated. The selection criterion was set as k_{eff} (BOC)$\geqslant$1.0. A scatter plot illustrating three parameters (cycle exposure, maximum k_{eff} and maximum Fq throughout the cycle) is presented in Figure 4.14. Notably, unlike the first cycle's results, the scatter plot does not show a clear correlation between the maximum k_{eff} and the maximum F_q for second cycle. This difference is attributed to the checkerboard pattern of fresh and burned assemblies, which leads to a more complex neutron distribution in the core.

Configurations that failed to meet the initial k_{eff} criterion were deleted. This failure was due to inappropriate combinations of fuel and burnable absorber concentrations that resulted in insufficient reactivity to start a cycle. The remaining configurations were carried forward to cycle 3.

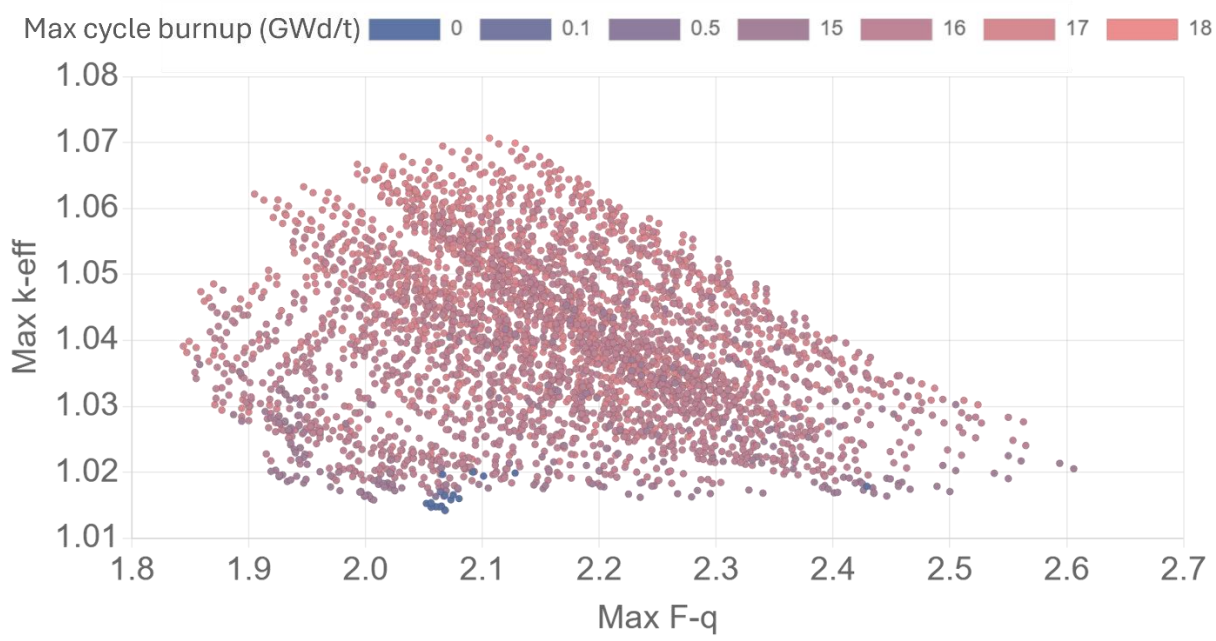

Figure 4.14 Scatter plot of cycle 2 simulation results: Maximum k_{eff} vs. Maximum F_q vs. Cycle burnup

The core simulations were repeated up to cycle 5 under ARO conditions, using the same core configurations from the previous cycle, to ensure the convergence toward an ARO equilibrium core state. This iterative process resulted in 3434 remaining configurations, as depicted in Figure 4.15.

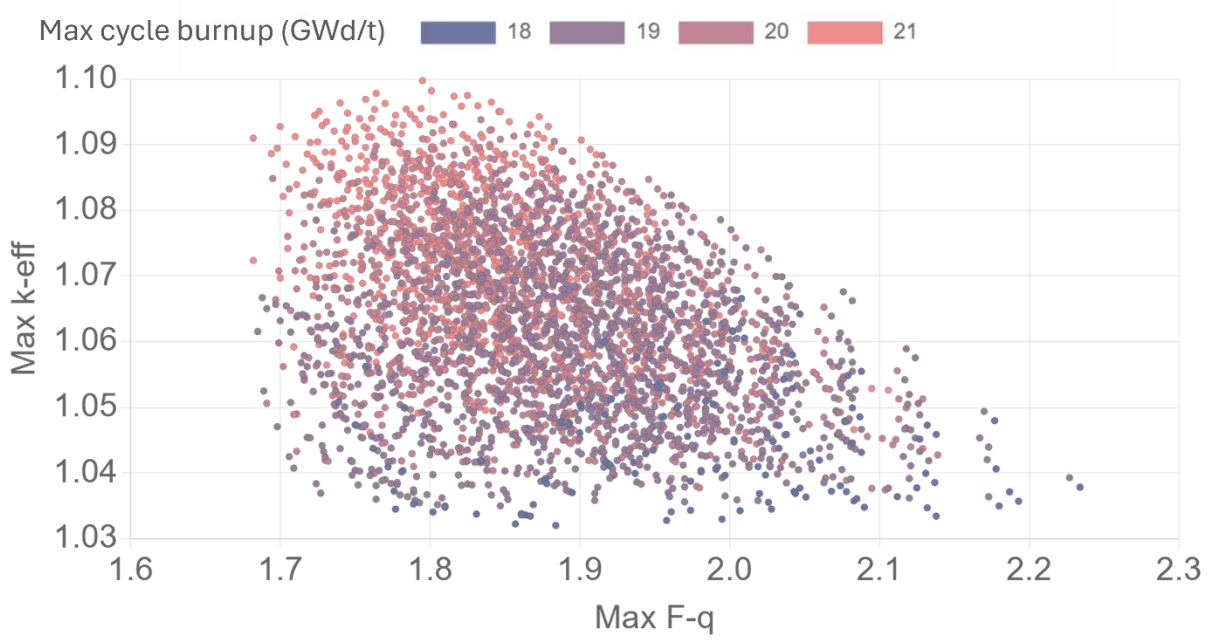

Figure 4.15 Scatter plot of cycle 5 simulation results: Maximum k_{eff} vs. Maximum F_q vs. Cycle burnup

Three random three configurations were selected as shown in *Table 4-4* for determination of ARO equilibrium cycle.

Table 4-4 Three core configurations selected for the determination of equilibrium cycle

Configurations	FAs	Fuel enrichment (%)	BA number per FA	BA loading (%)
Configuration 1	FA1	4.8	20	8
	FA2	4.2	40	10
	FA3	4.8	24	8
	FA4	1.8	20	8
Configuration 2	FA1	4.95	24	8
	FA2	4.4	40	10
	FA3	4.95	24	8
	FA4	1.8	20	8
Configuration 3	FA1	4.95	24	8
	FA2	4.0	32	10
	FA3	4.8	24	8
	FA4	1.8	24	8

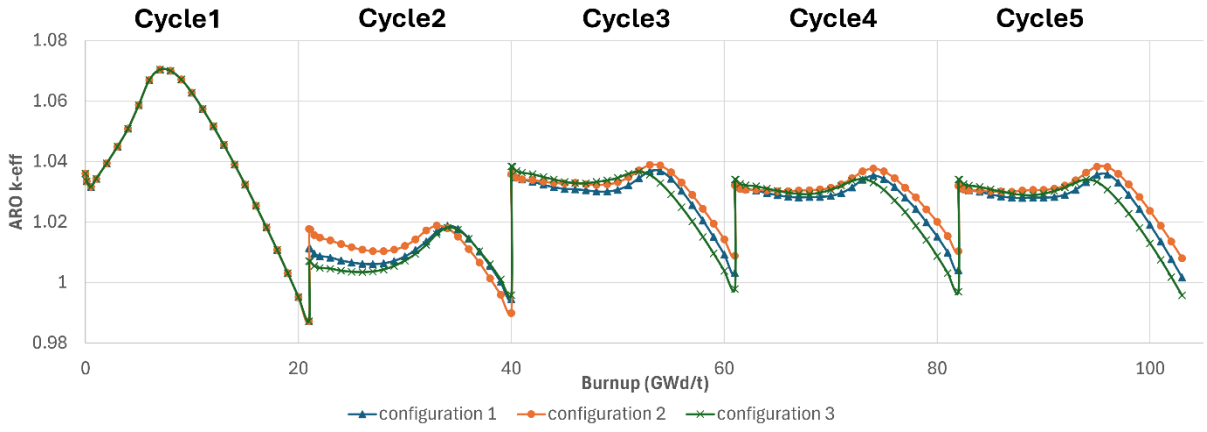

Figure 4.16 k_{eff} *as a function of burnup from cycle 1 to cycle 5 of the three core configurations*

The k_{eff} evolutions across burnup for Cycles 1–5 under ARO conditions for RLP1 and RLP2 are shown in Figure 4.16, differences in k_{eff} between Cycle 4 and Cycle 5 were less than 0.5% for the selected configurations, indicating equilibrium behavior. Therefore, the cycle 4 is considered as the equilibrium cycle and is used to determine the layout of regulating CR banks.

2) Control Rod Layout Determination

To keep consistency with first cycle, reducing the change in control rod layout during refueling, the two control rod layouts are applied to the equilibrium cycle. While these control rod layouts may not be the absolute best design, they are well-established and applicable choice for this first-cycle and equilibrium-cycle core.

3) Critical Search

Subsequently, From Cycle 6 onward, SIMULATE5 was used to simulate core behavior with the determined CR layouts, incrementally adjusting CR positions to maintain criticality (k_{eff} between 0.9990 and 1.0001). Each CR bank movement was modeled in 0.5 cm increments. Cycles 6 to 8 were simulated without eliminating configurations until Cycle 9, where the FA discharge exposure stabilized between cycles. For these critical core simulations, the cycle exposures were set to 21 GWd/t. Specifically, for a given exposure, all cycles from 6 to 9 conducted to the same set exposure. The same safety criteria used for the first-cycle selection were applied to cycle 9:

- $F_q \leq 3.26$
- $F_{\Delta H} \leq 1.62$
- -0.4≤Axial offset≤0.4
- FTC < 0
- MTC < 0

After applying these criteria, 99 configurations remained for CR-A (Figure 4.17) and 47 configurations remained for CR-B (Figure 4.18).

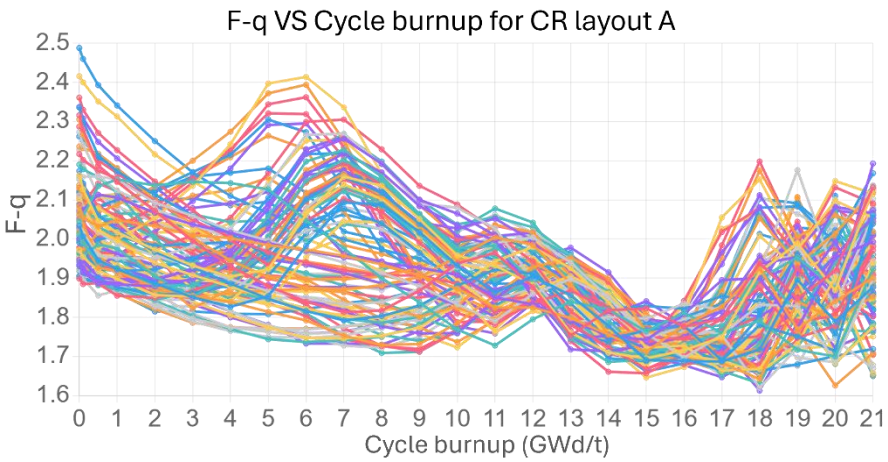

Figure 4.17 F_q throughout equilibrium cycle of the remaining configurations after safety selection filter for CR-A

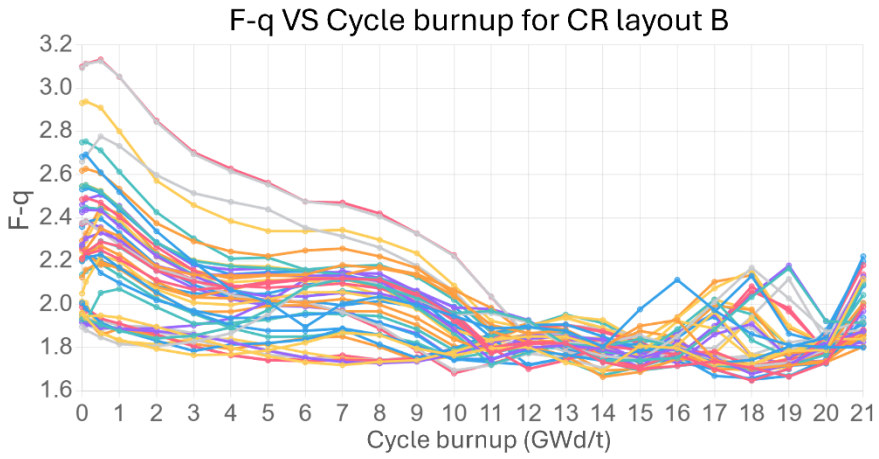

Figure 4.18 F_q throughout equilibrium cycle of the remaining configurations after safety selection filter for CR-B

Similar to the first-cycle core selection, to better filter the optimized option, a series of stricter selection criteria are applied to the remaining configurations:

1) $F_q \leq 2.5$
2) $F_{\Delta H} \leq 1.50$
3) -0.4≤Axial offset≤0.4
4) FTC < 0
5) MTC < 0

After applying these stricter criteria, 8 configurations remained for CR-A and 15 configurations remained for CR-B. The F_q for the remaining filtered core configurations throughout the cycle are displayed in Figure 4.19 and Figure 4.20. Among these options, the ones with CR-layout-A and CR-layout-B that exhibit the smallest peak F_q across the entire cycle were ultimately chosen as the optimized first-cycle core configurations for each control rod layout, see Table 4-5.

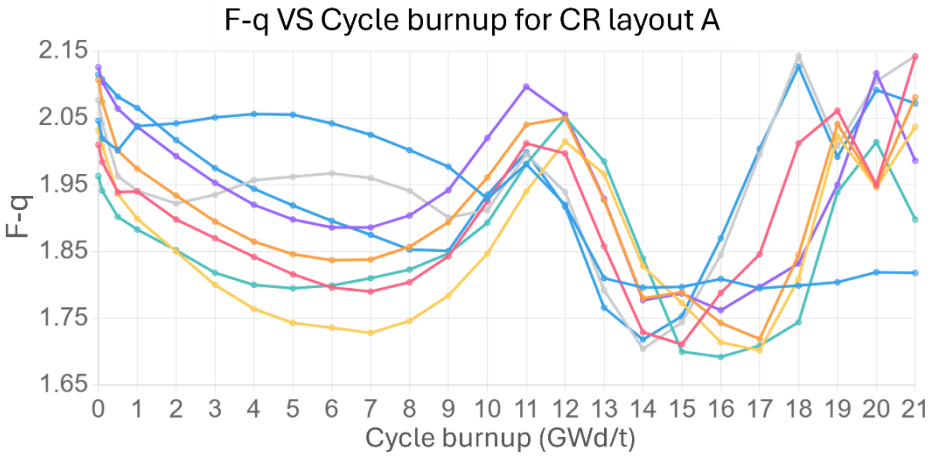

Figure 4.19 F_q throughout equilibrium cycle of the remaining configurations after stricter selection filter for CR-A

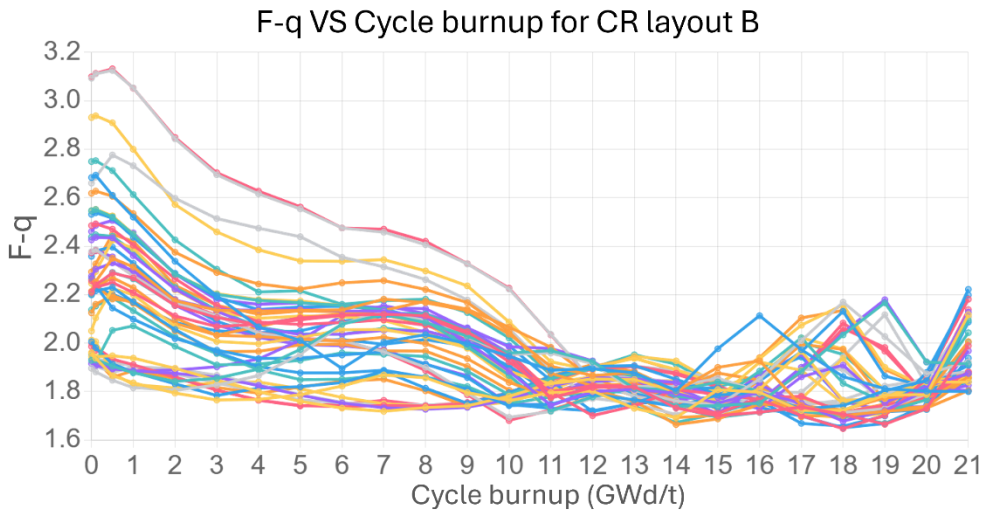

Figure 4.20 F_q throughout equilibrium cycle of the remaining configurations after stricter selection filter for CR-B

Table 4-5 Optimized core configurations for equilibrium cycle

Control rod layouts	FAs	Fuel enrichment (%)	BA number per FA	BA loading (%)
CR layout A	FA1	4.8	24	8
	FA2	4.2	32	10
	FA3	4.8	24	8
	FA4	1.8	20	8
CR layout B	FA1	4.8	24	8
	FA2	4.2	28	10
	FA3	4.8	24	8
	FA4	1.8	20	8

Figure 4.21 illustrates the CR movements for both configurations in an equilibrium cycle, which differ significantly from those of the first cycle. In the equilibrium cycle, CRs are gradually withdrawn throughout the entire cycle. In contrast, during the first cycle, CRs are initially inserted and then gradually withdrawn.

This difference is due to the higher concentration of burnable poisons at BOC in the first cycle, which compensate for the core's excess reactivity, so fewer CRs are need to be inserted at BOC. However, the equilibrium cycle contains some burned FAs with very low residual BA left from last cycle, resulting in a lower initial BA content at the beginning of equilibrium cycle core. Thus, a greater insertion of CRs is required to achieve criticality.

For both configurations, CR banks R1 and R2 are fully inserted at BOC. R2 in CR-B begins to be withdrawn at 13 GWd/t, earlier than the 16GWd/t withdrawal point for CR-A.

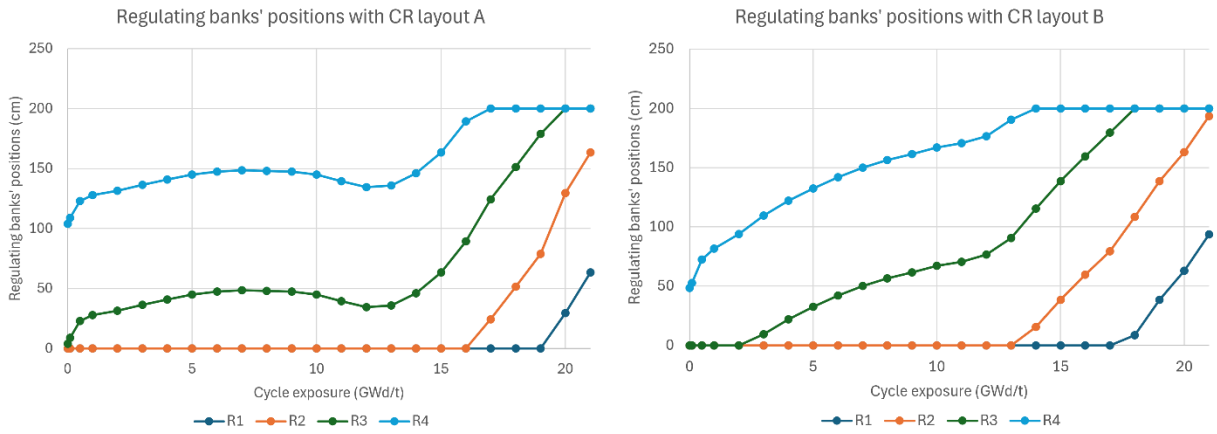

Figure 4.21 Regulating control rod banks' positions throughout the cycle

4.3.5 Saved Simulation Time

Any modification to the fuel assembly configuration necessitates regenerating cross sections via CASMO5 and re-conducting core simulation by SIMULATE5. This is where CoreOptimizer plays a critical role. For example, it automates repetitive CASMO5 input files generation by updating user-defined templates due to the modification of fuel assembly configuration in this work, thereby reducing the risk of human error in manual processes.

CoreOptimizer also integrates with SIMULATE5, managing input templates for both the first cycle with new fuel loading pattern and the equilibrium cycle with new refueling loading pattern. Once templates are modified with updated configurations, the search process can be restarted. With CoreOptimizer, the user initiates the process with a single click per cycle. The automation enables all simulations to be conducted overnight and drastically cuts down the time required for repetitive simulations.

Table 4-6 Comparison of consumed time between Manual effort method and CoreOptimizer

Method	Time Per Cycle	Working Time Per Cycle	Total time (cycle 2-7)
Manual Effort	$= \frac{(3+1+5)\times 3456}{6}$ $= 5184min$	$= \frac{5184min}{8h/day} \approx 10.8days$	$= 10.8days \times 6$ $\approx 65days$
CoreOptimizer	$= \frac{5\times 3456}{6} = 2880min$	$= \frac{2880min}{24h/day} = 2days$	$= 2\times 6 = 12days$

For instance, as shown in Table 4-6, the equilibrium-cycle search process is accelerated using CoreOptimizer under the following conditions:

- Writing an input file for SIMULATE5: 3min;
- Start and execution: 1min;

- Burnup simulation per core: 5min;
- Number of parallel simulations: 6
- Manual working hour: 8h/day
- Program working hour: 24h/day

By using CoreOptimizer, the equilibrium cycle search process is shortened by 53 days—a 81.5% reduction compared to manual efforts.

5 Analysis of the Optimized Cores

This section presents a comprehensive analysis of the optimized core designs, investigating both their first-cycle and equilibrium-cycle characteristics. The analysis focuses on the key neutronics and safety parameters comparisons for the optimized configurations with two control rod layouts under hot-full-power (HFP) operational conditions, and estimations of the shutdown margins under HFP, hot-zero-power (HZP) and cold-zero-power (CZP) scenarios.

5.1 Analysis of the First-Cycle Cores

The optimal core adopted loading pattern is shown in Figure 4.1 and the two radial arrangements of CR banks (CR-A and CR-B) are depicted in Figure 4.8. The optimized core configurations are listed in Table 4-3.

5.1.1 Characterization of the Optimized First-Cycle Cores

5.1.1.1 Power Axial Offsets Throughout the First Cycle

Due to the similar movement of control rods (Figure 4.13), the power axial offset (AO) trend for both CR layouts is remarkably similar. Both start with a negative AO, resulting from the partial insertion of control rods from the top of the core, suppressing power in the upper core and shifting the peak axial power towards the bottom. Thus, the fuel in the bottom half of the core is depleted faster. As the cycle operates (after 8GWd/t), control rods are withdrawn one bank after another. Therefore, the AO shifts gradually to the upper half parts, crossing the zero point around 14GWd/t and continuing to increase. Notably, the AOs for both layouts remain well within the typical safety limits of [-0.4, +0.4] throughout the entire cycle. This demonstrates that the axial power distribution is effectively controlled, ensuring a safe operational state.

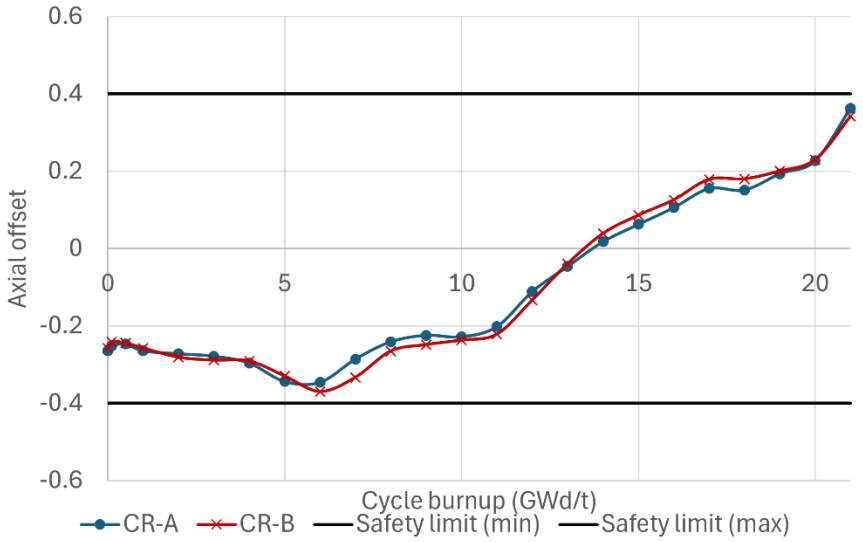

Figure 5.1 Power axial offset throughout the first cycle

5.1.1.2 Control Rod Positions and Radial Power Distribution at BOC/MOC/EOC

The control rod movements of the two proposed CR layouts (CR-A and CR-B) distinctly influence the core's radial power distribution at BOC/MOC/EOC, as shown in Figure 5.2. The color scale ranges from 0.66 (dark blue) to 1.30 (red), indicating the relative power factor. The regulating control rod positions are defined by their height, where 0 signifies a fully inserted bank at the bottom of the core, 200 indicates a fully withdrawn bank at the top of the core, other values are the height of the control rod banks.

BOC:

CR-A: CR banks 1 and 2 are fully inserted while banks 3 and 4 are partially inserted. The peak power occurs in the intermediate region (5B- and 8E-) when the control rods in this location is slightly inserted. The lowest power occurs at 6D- where bank 1 is fully inserted.

CR-B: CR banks 1 is fully inserted, banks 2 and 3 are partially inserted, and bank 4 is fully withdrawn. The radial power appears flatter than CR-A. The highest power factors are also in the intermediate region, but the overall distribution is more uniform. That indicates that CR-B is more suitable for this core at BOC.

MOC:

CR-A: Control rod banks 1, 2, and 3 are fully inserted and bank 4 are mostly inserted. The peak power shifts to the central assembly with a value of 1.26 because there is no control rod placed at this location. In the central and intermediate regions, the assemblies without control rod inserted show higher power factors (1.15-1.20).

CR-B: Control rod banks 1, 2, and 3 are fully inserted and bank 4 are mostly inserted. The peak power occurs in the intermediate region (7C-) with a value of 1.24. The outer region shows higher power factor than inner region.

EOC:

CR-A: Only bank 1 is slightly inserted and other three banks are fully withdrawn. The peak power shifts back to the intermediate region (5C- and 7E-). In the central and intermediate region, the power distribution becomes more uniform and the lowest power exists in the outermost region.

CR-B: Similar to CR-A, the peak power occurs in the intermediate region (6C-) and the power distribution becomes more uniform and the lowest power exists in the outermost region.

In all operational states, the increased insertion depth of regulating banks causes a pronounced local neutron flux depression within the associated fuel assemblies, which directly results in a reduction of the local radial power fraction (RPF). Consequently, the higher RPF shifts to regions where control rods are not inserted.

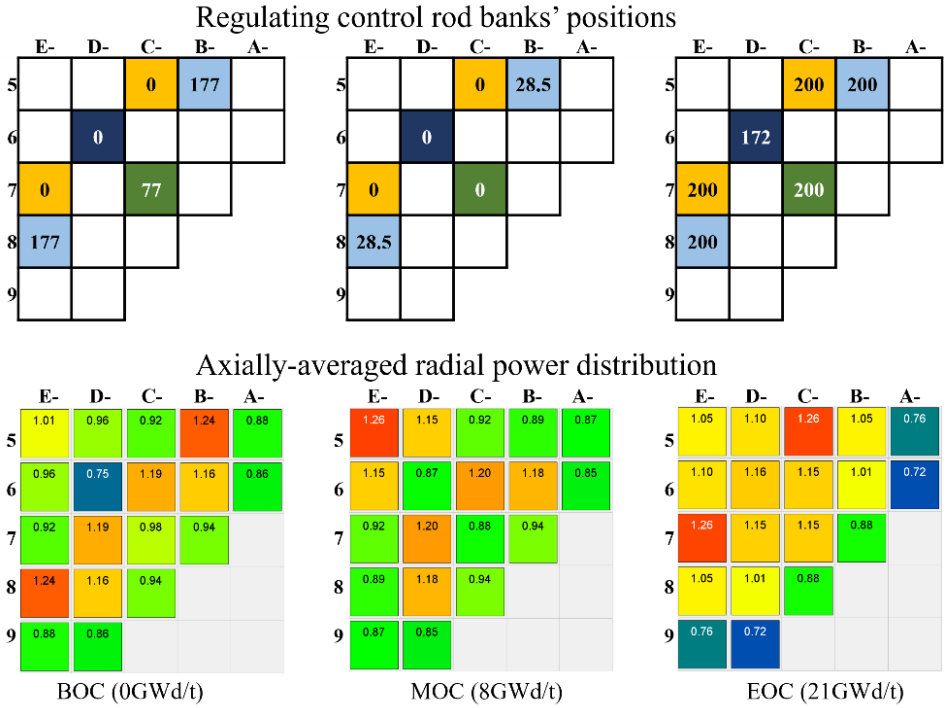

Figure 5.2 Regulating banks' positions and radial power distribution with control rod layout A for BOC/MOC/EOC

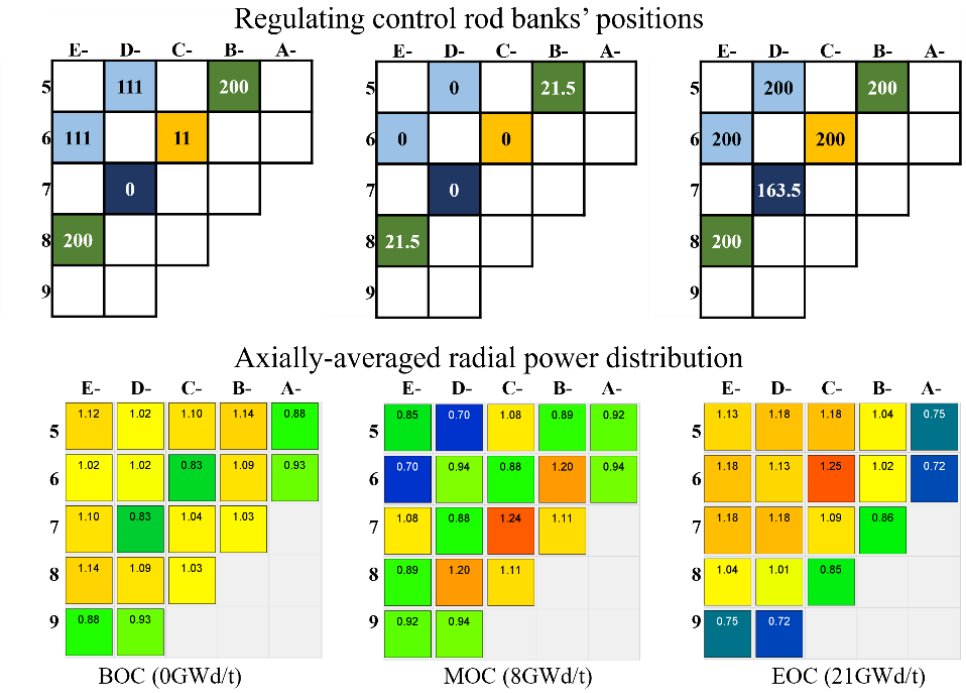

Figure 5.3 Regulating banks' positions and radial power distribution with control rod layout B for BOC/MOC/EOC

5.1.1.3 3D and 2D Pin Power Factors

3D and 2D pin power factors (F_q and $F_{\Delta H}$) demonstrate sufficient safety margins throughout the operational cycle, as displayed in Figure 5.4. The peak F_q values are 2.322 for CR-A and 2.374 for CR-B, with safety margins of 28.8% and 27.4%, respectively. For $F_{\Delta H}$, the peak values are 1.469 for CR-A and 1.425 for CR-B, with safety margins of 9.74% and 9.20%.

The graphs show that both factors for CR-A are slightly higher at the beginning of cycle, but remain relatively low for the rest of the operational cycle. Notably, all values stay well within their respective safety limits.

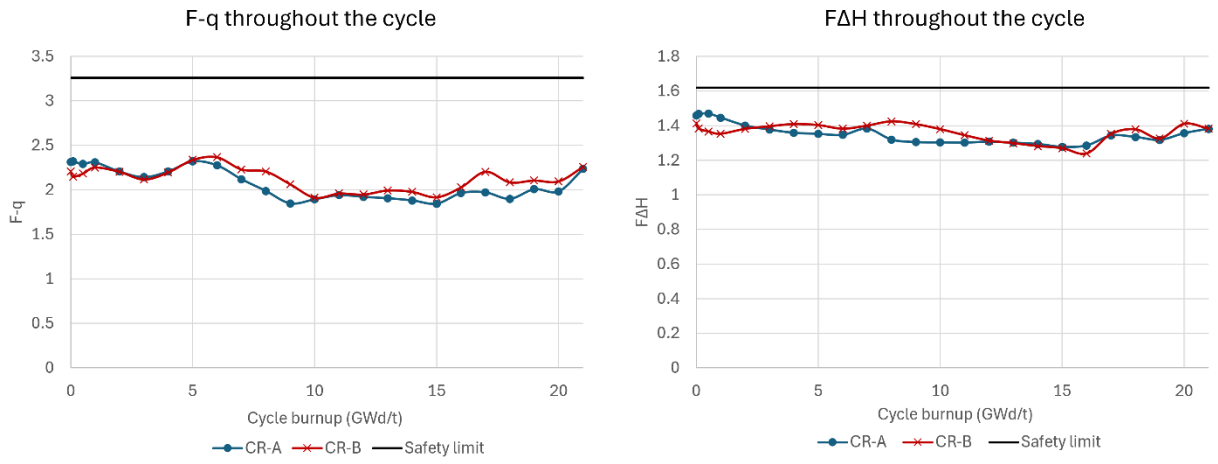

Figure 5.4 3D and 2D pin power factors throughout the operational cycle

5.1.1.4 Reactivity Temperature Coefficients

Table 5-1 depicts the fuel and moderator temperature coefficients at BOC/MOC/EOC for the two core configurations. All coefficients remain negative across the entire cycle, confirming inherent core stability. Notably, the values of MTC are much more negative compared to FTC, remaining below -30 pcm/K.

According to (Edenius, 1976), the typical MTC values for PWRs generally fall within the range of -5 to -30 pcm/K. Some shows less negative values or even slightly positive values such as -4.81 pcm/K in the IPEN/MB-01 research reactor (Silva, et al., 2017) and a range of -1.0 to 1.0 pcm/K for the AP1000 (Pinem, et al., 2018). Compared to boron-based designs, the SBF cores features the more negative MTCs (Abdelhameed, et al., 2018), typically more negative than -30 pcm/K. The designed cores demonstrate this characteristic, resulting in a stronger inherent safety: a rise in moderator temperature leads to a more rapid reduction in reactivity.

Table 5-1 Reactivity temperature coefficients at BOC/MOC/EOC of first cycle

		BOC	MOC	EOC
Fuel temperature coefficient (pcm/K)	CR-A	-1.44	-1.38	-1.47
	CR-B	-1.43	-1.38	-1.48
Moderator temperature coefficient (pcm/K)	CR-A	-37.08	-35.50	-36.36
	CR-B	-36.43	-36.94	-35.78

5.1.1.5 Axial Power and Temperatures Profiles

Figure 5.5 illustrate the axial power distribution and axial temperatures of fuel centreline, fuel cladding and coolant at different stages of their first cycle: BOC, MOC and EOC. The trends of two configurations CR-A and CR-B are closely similar.

Axial power distributions

At BOC and MOC, the axial power distribution is slightly skewed towards the bottom of the core. This arises from the coolant temperature increasing from the bottom to the top. The higher coolant temperature at the core top reduces its density, leading to weaker moderation and lower power generation.

By EOC, the axial power shifts upward, with a peak at 160cm or 170cm. This is a classic characteristic of long-term fuel burnup: Initially, fissile material experiences a higher neutron flux at the core bottom. As it depletes over time, power generation shifts to less depleted regions, which is the core top.

Axial temperature profiles

The fuel centreline temperature closely tracks the axial power distribution as heat generation occurs within the fuel itself. In contrast, the coolant temperature exhibits a steady rise from the core inlet to the outlet.

The coolant enters at a lower temperature at the core inlet and progressively absorbs heat from the fuel rods as it flows upwards, reaching its highest temperature at the core exit. Meanwhile, the fuel cladding temperature remains intermediate between the fuel centreline and the coolant temperatures, reflecting the heat transfer pathway: from the fuel, through the cladding and into the coolant via convection.

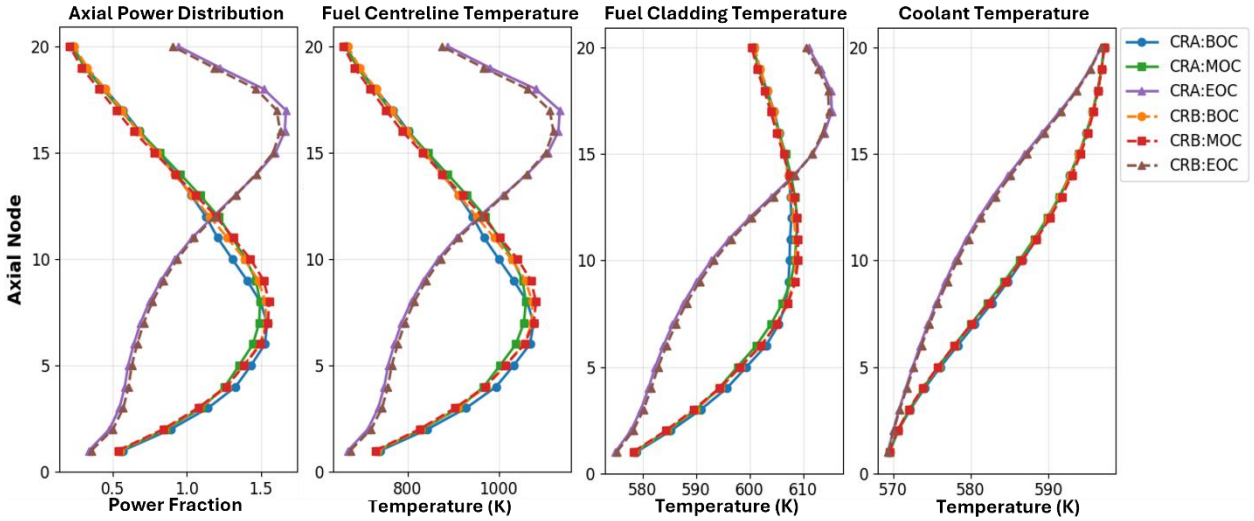

Figure 5.5 Axial power distribution and axial temperature profiles of fuel centreline, fuel cladding and coolant at BOC/MOC/EOC of first cycle

5.1.1.6 Fuel Assembly Exposure at EOC

Figure 5.6 shows the FA exposure distribution at the end of the first cycle. At the end of first cycle, the assembly exposure for CR-A ranges from 16.92 to 24.42 GWd/t, while for CR-B, it ranges from 18.49 to 24.02 GWd/t. The narrower range for CR-B indicates a more uniform assembly exposure compared to CR-A. The lowest burnup values are observed at the positions where control rod banks 1 were inserted (6D- in the left figure and 7D- in the right figure), indicating that control rods at these locations suppress the reactivity for majority of the cycle.

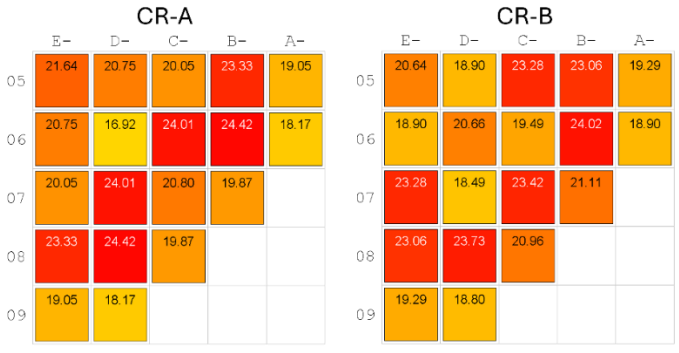

Figure 5.6 Axially-averaged fuel assembly exposure at EOC of the first cycle

5.1.2 Estimation of the Shutdown Margins at HFP/HZP/CZP for BOC/MOC/EOC

Nuclear safety regulations require reactor shutdown systems to maintain core subcriticality under all operational scenarios. Accordingly, k_{eff} is evaluated with all control rods inserted (ARI) under three scenarios:

- Hot Full Power (HFP): operating condition
- Hot Zero Power (HZP): Fuel and coolant temperatures fixed at 569.15K; core power reduced to 1.0×10^{-4} of rated full power
- Cold Zero Power (CZP): Fuel and coolant temperatures fixed at 300K; core power reduced to 1.0×10^{-4} of rated full power

Table 5-2 summarizes the key reactivity effects under HFP/HZP/CZP conditions, along with the cold shutdown margin (CSDM) with a single failure during burnup, as described in Figure 2.7. The specific locations of control-rod assemblies are shown in Figure 4.1. Xenon worth quantifies the reactivity effect due to xenon buildup between HFP and HZP. Cold/hot swing indicates reactivity changes associated with coolant temperature variations. The CSDM is calculated under the assumption of a single failure, where the highest worth control rod is considered to be stuck out.

Table 5-2 Key reactivity effects and shutdown margin at HFP/HZP/CZP during burnup

Reactivities \ States	CR-A			CR-B		
	BOC	MOC	EOC	BOC	MOC	EOC
ARI k_{eff} (HFP)	0.76487	0.77547	0.71780	0.76047	0.77603	0.71968
ARI k_{eff} (HZP)	0.80260	0.81226	0.75945	0.79707	0.81277	0.76197
ARI k_{eff} (CZP)	0.90944	0.89798	0.84483	0.90363	0.89730	0.84627
Xenon worth (pcm)	6146	5841	7640	6038	5825	7712
Cold/hot swing (pcm)	14637	11752	13307	14795	11591	13073
Location of highest-worth CR at CZP	3F-	3F-	3F-	3E-	5G-	3G-
CSDM with single failure (pcm)	4041	5401	12194	5651	5598	11658

Key observations include:

- The ARI k_{eff} for all scenarios (HFP, HZP, CZP) and burnup stages (BOC, MOC, EOC) are well below 1.0 for both core configurations.
- At CZP, the location of the highest-worth CR remains constant for CR-A (at position 3F-) throughout the operational cycle. In contrast, the location varies across the cycle for CR-B.
- For CSDM with a single failure, CR-B shows a larger margin at BOC and MOC compared to CR-A. However, CR-B's margin is smaller than that of CR-A at EOC.
- The xenon worth and cold/hot swing are similar between the two configurations.

5.2 Analysis of the Equilibrium-Cycle Cores

The optimal equilibrium-cycle core configurations adopted refueling loading pattern shown in Figure 4.1 and the two radial arrangements of CR banks (CR-A and CR-B) are depicted in Figure 4.8. The optimized core configurations are listed in Table 4-5.

5.2.1 Characterization of the Optimized Equilibrium-Cycle Cores

5.2.1.1 Power Axial Offset Throughout the Equilibrium Cycle

Due to slight differences in CR movement between these two configurations (Figure 4.21), the AO behavior varies slightly. For CR-A, from 0 to 15 GWd/t, the axial positions of CR banks R3 and R4 maintains relatively stable, causing the AO to remain at an approximately constant value of -0.1. When R2 starts to be withdrawn, AO begins to increase more rapidly at 16GWd/t, reaching a maximum value of 0.207 at 21GWd/t.

At BOC, the deeper insertion of CRs in CR-B results in a more negative initial AO value of -0.156 compared to CR-A. The value then increases gradually and steadily, reaching a maximum value of 0.118.

Overall, the AO range in the equilibrium cycle is significantly smaller compared to the first cycle. Compared to the safety limit, CR-A demonstrates a safety margin of 48.33% while CR-B provides 60.95%.

This demonstrates that the axial power distribution is effectively controlled, ensuring a safe operational state throughout the equilibrium cycle.

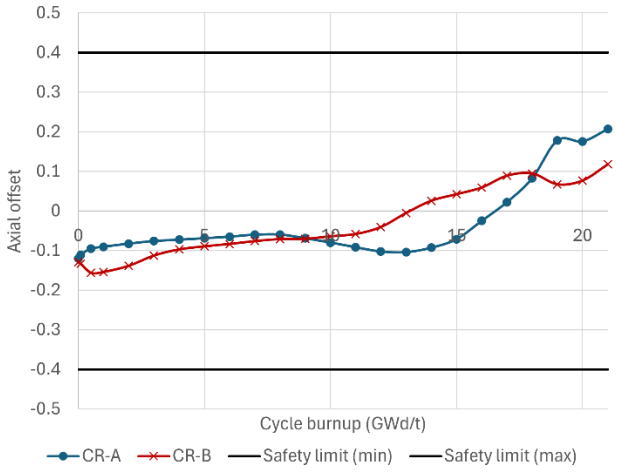

Figure 5.7 Power axial offset along the cycle exposure

5.2.1.2 Control Rod Positions and Radial Power Distribution at BOC/MOC/EOC

The control rod movements of the two proposed CR layouts (Figure 4.8) distinctly influence the core's radial power distribution at BOC/MOC/EOC (Figure 5.8). The color scale ranges from 0.67 (dark blue) to

1.35 (red), indicating the relative radial power factor. Since MOC is the most active state-point, it is 11GWd/t in the equilibrium cycle.

BOC:

CR-A: CR banks 1 and 2 are fully inserted while banks 3 and 4 are partially inserted. The peak power occurs in the intermediate region (6B- and 8D-), where no control rods are present. The lowest power occurs in the central assembly.

CR-B: CR banks 1, 2 and 3 are fully inserted while bank 4 is partially inserted. The radial power appears less flat than in CR-A. The highest power factor is also in the intermediate region (7C-) where no control rods are present.

MOC:

CR-A: The control rods positions are similar to those at BOC. The peak power occurs in the intermediate region (5B- and 8E-) where R4 is partially inserted. And the peak power value is lower than at BOC. The lowest power shifts to assembly 6D- where R1 is fully inserted.

CR-B: CR banks 1 and 2 are fully inserted while banks 3 and 4 are partially inserted. The peak power is located in the intermediate region (6B- and 8D-) with a value of 1.32, while other locations show a relatively uniform power distribution.

EOC:

CR-A: R1 and R2 are partially inserted and R3 and R4 are fully withdrawn. The peak power occurs in the intermediate region (6C- and 7D-).

CR-B: Similar to CR-A, R1 and R2 are inserted, and R3 and R4 are fully withdrawn. The peak power occurs in the intermediate region (6C-) and the power distribution becomes more uniform, with the lowest power existing in the outermost region.

When comparing these two configurations, CR-A has a smaller range of radial power factors. However, the power distribution in CR-B is more uniform except for the peak power assembly.

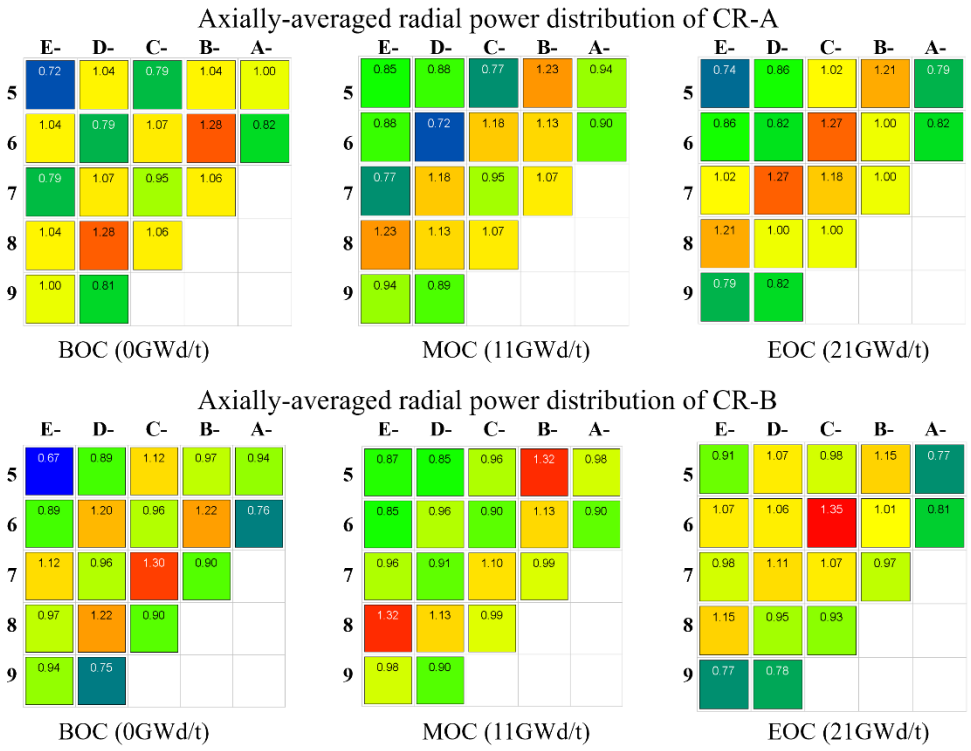

Figure 5.8 Axially-averaged radial power distribution of two configurations at BOC/MOC/EOC

5.2.1.3 3D and 2D Pin Power Factors

3D and 2D pin power factors (F_q and $F_{\Delta H}$) demonstrate sufficient safety margins throughout the equilibrium cycle, as displayed in Figure 5.9. The peak F_q values are 2.038 for CR-A and 2.002 for CR-B, corresponding to safety margins of 37.5% and 38.6%, respectively. For $F_{\Delta H}$, the peak values are 1.462 for CR-A and 1.471 for CR-B, with safety margins of 9.74% and 9.20%. Notably, the $F_{\Delta H}$ values in equilibrium cycle are within a similar range to those in the first cycle. However, the F_q values are much smaller in the equilibrium cycle than in the first cycle.

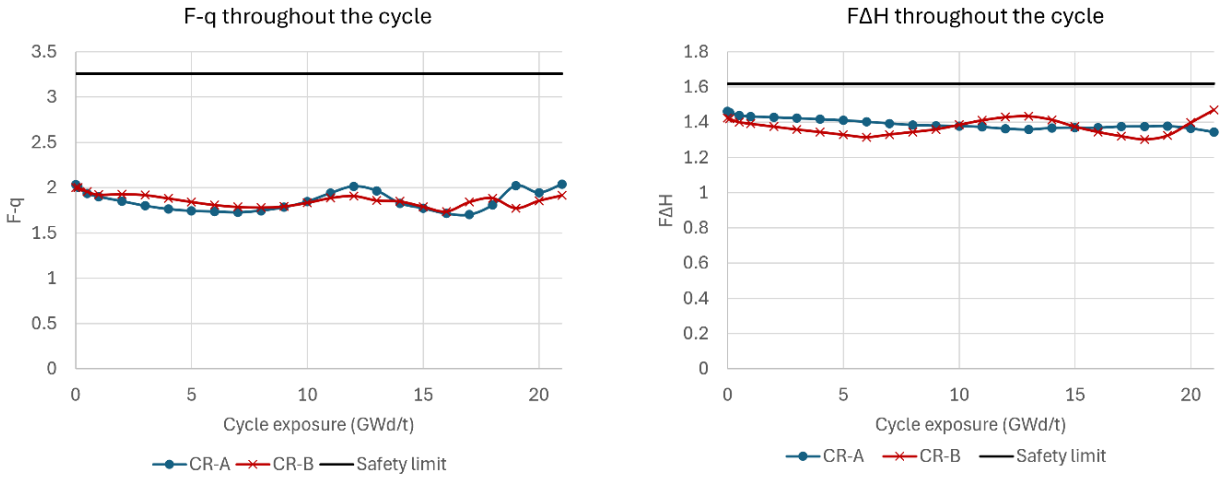

Figure 5.9 3D and 2D pin power factors throughout the equilibrium cycle

5.2.1.4 Reactivity Temperature Coefficients

Table 5-3 depicts the fuel and moderator temperature coefficients at BOC/MOC/EOC of equilibrium cycle for the two core configurations. All coefficients remain negative across the entire cycle, confirming inherent core stability. Furthermore, all MTC and FTC values of the equilibrium cycles are smaller than those of the first cycle.

Table 5-3 Reactivity temperature coefficients at BOC/MOC/EOC of equilibrium cycle

		BOC	MOC	EOC
Fuel temperature coefficient (pcm/K)	CR-A	-1.48	-1.48	-1.55
	CR-B	-1.48	-1.50	-1.55
Moderator temperature coefficient (pcm/K)	CR-A	-41.88	-40.82	-44.18
	CR-B	-42.11	-40.48	-41.90

5.2.1.5 Axial Power and Temperatures Profiles

Figure 5.10 illustrate the axial power distribution and axial temperatures of fuel centreline, fuel cladding and coolant at BOC/MOC/EOC of their equilibrium cycle.

The overall trends in axial power distributions for both configurations (CR-A and CR-B) in the equilibrium cycle are similar to those in the first cycle: At BOC and MOC, the axial power distribution is slightly skewed towards the bottom of the core. By EOC, the axial power shifts upward, with a peak at 160cm to 170cm.

Notably, across all the burnup stages, CR-A consistently shows higher peak power values than CR-B. This indicates that CR-B has better performance in terms of managing the axial power profile, resulting in a flatter axial distribution.

The axial temperature profiles can reflect the heat transfer pathway well, showing the same characteristics as observed in the first cycle. This confirms that heat is consistently transferred from the fuel centreline, through cladding, into the coolant.

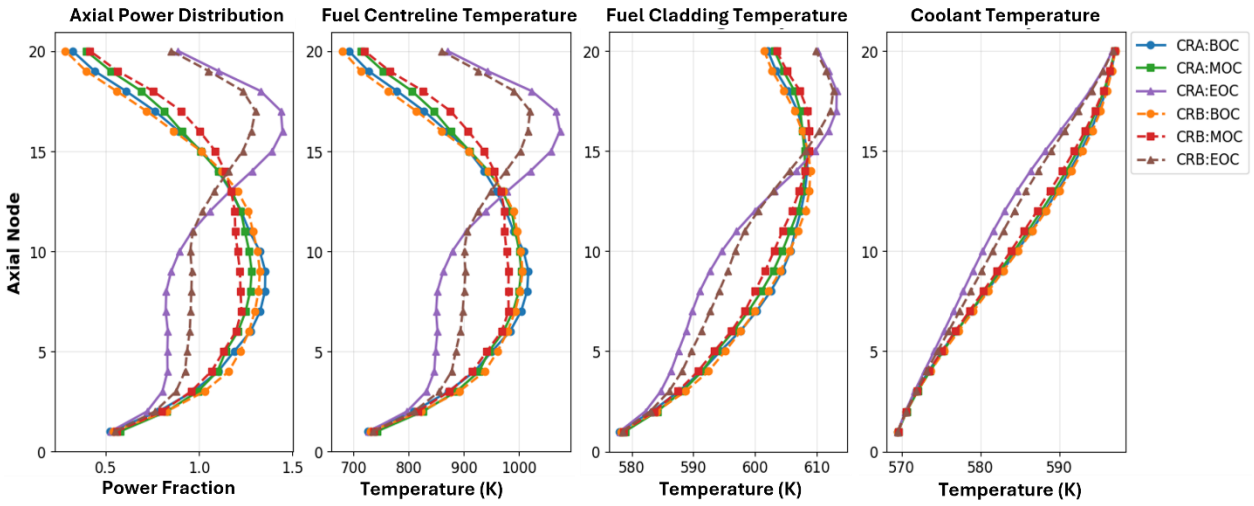

Figure 5.10 Axial power distribution and axial temperature profiles of fuel centreline, fuel cladding and coolant at BOC/MOC/EOC of equilibrium cycle

5.2.1.6 Fuel Assembly Exposure at EOC

Figure 5.11 shows the FA exposure distribution at the end of the equilibrium cycle. At EOC, the discharge assembly exposure for CR-A ranges from 37.80 to 46.11 GWd/t, while for CR-B, it ranges from 37.49 to 46.51 GWd/t.

Excluding the central fuel assembly, the average discharge FA exposures are 42.19 GWd/t and 42.08GWd/t, for CR-A and CR-B, respectively. The highest discharge pin exposures are 52.65 GWd/t and 48.82 GWd/t for CR-A and CR-B. All of these exposure levels remain well below the generally accepted safety limits for UO_2 fuel, which are 62 GWd/t for rod average and 55 GWd/t for assembly average. This demonstrates that long-term material integrity is maintained under both core configurations.

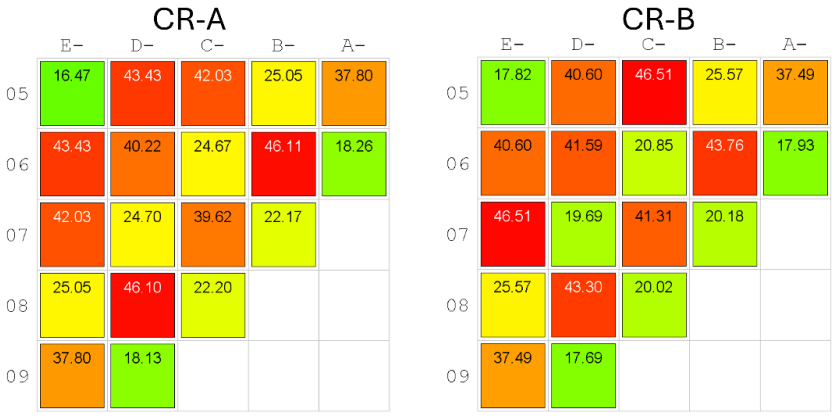

Figure 5.11 Axially-averaged fuel assembly exposure at EOC of the first cycle

5.2.2 Estimation of the Shutdown Margins at HFP/HZP/CZP for BOC/MOC/EOC

Table 5-4 summarizes the key reactivity effects under HFP/HZP/CZP conditions, along with the cold shutdown margin (CSDM) with a single failure during burnup.

Key observations include:

- The ARI k_{eff} for all scenarios (HFP, HZP, CZP) and burnup stages (BOC, MOC, EOC) are well below 1.0 for both core configurations.
- For CSDM with a single failure, CR-A shows a larger margin at BOC and MOC compared to CR-B. However, CR-A's margin is smaller than that of CR-B at EOC.
- The xenon worth and cold/hot swing are similar between the two configurations.

Table 5-4 Key reactivity effects and shutdown margin at HFP/HZP/CZP during burnup

Reactivities \ States	CR-A			CR-B		
	BOC	MOC	EOC	BOC	MOC	EOC
ARI k_{eff} (HFP)	0.79708	0.78169	0.74905	0.80052	0.77742	0.74192
ARI k_{eff} (HZP)	0.81865	0.80458	0.77696	0.82304	0.80042	0.76697
ARI k_{eff} (CZP)	0.90914	0.88941	0.86409	0.91357	0.88781	0.85518
Xenon worth (pcm)	3306	3640	4796	3418	3696	4402
Cold/hot swing (pcm)	12158	11854	12978	12040	12298	13449
Location of highest-worth CR at CZP	4H-	3F-	3F-	6D-	6D-	7C-
CSDM with single failure (pcm)	5039	7860	9682	4403	7762	11601

The comparison between the first cycle and the equilibrium cycle confirms that the equilibrium cycles exhibit better inherent safety features. This is demonstrated by the following findings: In the equilibrium cycles, both control rod layouts yield smaller peak 3D pin power fraction values, which offers larger 3D pin power margins. This feature is result from the fact that the power axial offsets of the equilibrium cycle are remarkably smaller than those in the first cycle. Moreover, the equilibrium cycle possesses much smaller moderator and fuel temperature coefficients compared to the first cycle. Additionally, the shutdown margins for equilibrium cycles are larger.

In conclusion, the optimized first and equilibrium cycle cores demonstrate safety features throughout their operational cycles, fulfilling the level 1 safety criteria in DiD principle. Furthermore, the cores also satisfy level 2 criteria in DiD principle, as confirmed by the cold shutdown margin with single failure.

6 Hypothetical Rod Ejection Accident in the Optimized Core

Once the steady-state core analysis has been completed, a detailed rod ejection accident (REA) analysis is performed to evaluate the safety performance of the optimized core designs under a design-basis accident. To support this evaluation, the analysis begins by outlining the fundamental principles of REA.

Subsequently, a comparison is conducted between the control rod worth and the effective delayed neutron fraction for two control rod layouts to identify the layout that can offer superior safety characteristics. Finally, the selected layout is then used to simulate a hypothetical REA in both the first and equilibrium cycles. The resulted local power response, global power and reactivity responses and safety parameters during REA will be analysed.

6.1 Fundamentals of Rod Ejection Accidents

This section encompasses the theoretical foundations of core performance during reactivity insertion, distinguishing between delayed supercritical and prompt supercritical regimes. Moreover, the initial conditions and modelling assumptions for REA simulations are detailed. Finally, the internationally recognized acceptance criteria and safety limits are reviewed to define the criteria for this investigation.

6.1.1 Introduction to Rod Ejection Accidents

REA is defined as the rapid ejection of the single control rod assembly with the highest reactivity worth in the core at different burnup stages. The reactor's response to REA largely depends on the magnitude of the introduced reactivity (ρ) relative to the effective delayed neutron fraction (β_{eff}). The core behaviour during an REA can be categorized as either delayed supercritical ($\rho < \beta_{eff}$) or prompt supercritical ($\rho > \beta_{eff}$). In this study, only the first 3 seconds for the accident is considered, the subsequent long-term behaviour is not evaluated.

Delayed Supercritical

If $\rho < \beta_{eff}$, the reactor remains delayed supercritical. In this state, the term $\frac{\rho(t)-\beta}{\Lambda} n(t)$ in (2.13) remains negative, meaning the prompt neutron contribution to the rate of neutron flux change is negative. Consequently, the reactor dynamics is primarily governed by the delayed neutrons, leading to a relatively slow and manageable power increase. The prompt power jump can be calculated by the simple analytical expression shown in (6.1) (AREVA, 2015).

$$\frac{P_j}{P_0} = \frac{\beta_{eff}}{\beta_{eff} - \rho} \tag{6.1}$$

Where P_j is the prompt-jump power, and P_0 is the initial power.

Prompt Supercritical

If $\rho > \beta_{eff}$, the reactor becomes prompt critical. Under this condition, the term $\frac{\rho(t)-\beta}{\Lambda} n(t)$ in (2.13) becomes positive. Given that Λ is very short, this prompt term dominates the overall rate of neutron flux change, leading to a rapid increase in reactor power. The magnitude and speed of the power surge are determined

by the prompt neutron lifetime l_p and the amount of ρ exceeding β_{eff}. This power increase occurs approximately exponentially, as shown in (6.2) (Bell and Glasstone, 1970).

$$P(t) \approx P_0 e^{\frac{\rho-\beta_{eff}}{l_p} \cdot t} \tag{6.2}$$

Since l_p is very short (typically on the order of 10^{-5} seconds), power can double within microseconds, leading to a rapid surge in the neutron population. This poses a greater potential threat to the core, and the fuel-clad thermal-mechanical processes become very complex. Due to this complexity, limits are based on tests that measure thermal energy of the fuel during the event (enthalpy-based limits). A simple relationship between energy deposited from a power pulse and other core parameters under prompt-critical condition is shown in (6.3) (AREVA, 2015).

$$E_d = \frac{2 * (\rho - \beta_{eff}) * c_p}{\alpha_D} \tag{6.3}$$

Where E_d is the energy deposited, c_p is the heat capacity of the fuel, α_D is the doppler temperature coefficient. For prompt-critical condition, the power increase is so rapid that the doppler effect is typically the only inherent feedback mechanism to terminate the prompt power excursion. Therefore, it is crucial to monitor the β_{eff} at different state points throughout the core's burnup cycle, as its value can change with fuel composition. This monitoring ensures that any reactivity insertions during REA should allow sufficient time for Doppler feedbacks to mitigate power excursions.

Therefore, in transient analysis, reactivity is often normalized to the effective delayed neutron fraction β_{eff} for better visualization of the relationship between reactivity and β_{eff}. The normalized reactivity is expressed in dollar units ($), see (6.4).

$$\rho(\$) = \frac{\rho}{\beta_{eff}} \tag{6.4}$$

6.1.2 Initial Conditions and Assumptions of REA

The REA simulations were based on a specific set of initial conditions and assumptions designed to represent challenging scenarios. The initial conditions for REA simulations are summarized in Table 6-1.

Table 6-1 Initial conditions of the rod ejection accident

	HFP	HZP
Thermal power	330MW	1.0E-4
Coolant flow rate	2006.4kg/s	2006.4kg/s
Pressure	15.0MPa	15.0MPa
Temperature	Coolant inlet temperature: 296 ℃	Average temperature of fuel and coolant: 296 ℃

For these simulations, the REA was conservatively assumed to be completed within a very short duration of 0.05 seconds, which is half of the typically assumed REA duration for a standard PWR core. The simulations were run for a duration of 3.0 seconds to adequately capture the initial power excursion and the subsequent behaviour of the core. Notably, SCRAM (emergency reactor shutdown) was intentionally not considered in these simulations to represent a bounding, worst-case scenario, focusing solely on the inherent response of the core and fuel design to the reactivity insertion.

Initially, the control rods were positioned to maintain the core in a critical state. The specific control rod positions for the first-cycle core at different states (HFP/HZP and BOC/MOC/EOC) before the REA are provided in Figure 6.1, Figure 6.2, Figure 6.3 and Figure 6.4. The control rod assembly with the highest reactivity worth for ejection is marked with red circles at each state.

The simulations use a fine time step of 1.0×10^{-4} seconds for the initial 0.2 seconds of the transient. A coarser time step of 0.02 seconds was subsequently used for the remaining 2.8 seconds of the 3-second simulations.

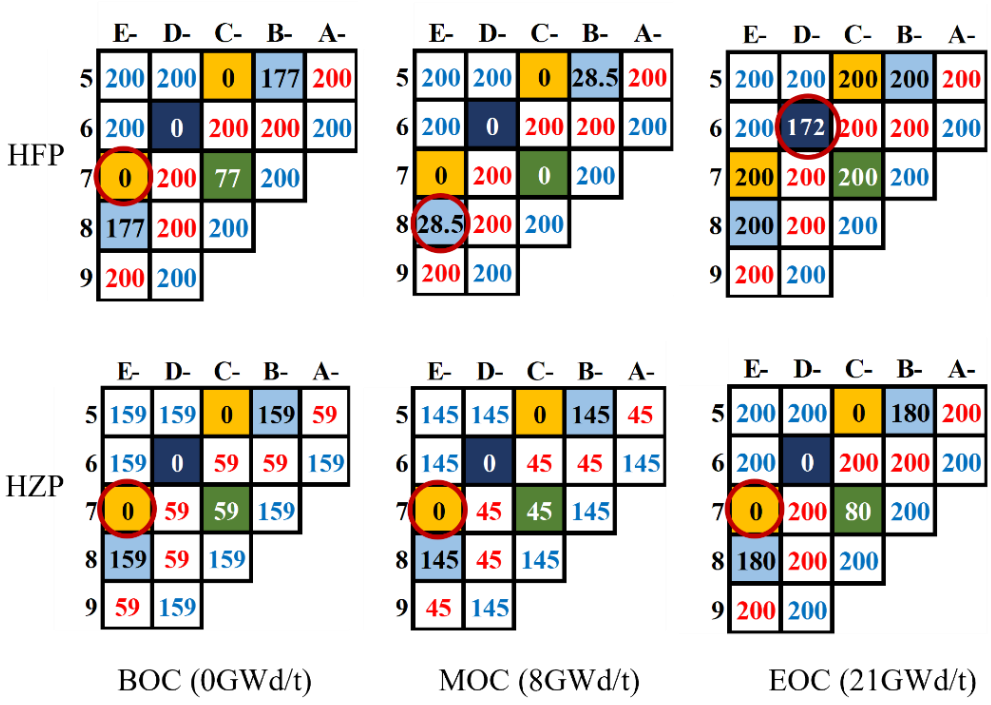

Figure 6.1 Locations of highest control rod worth of CR-A for first cycle

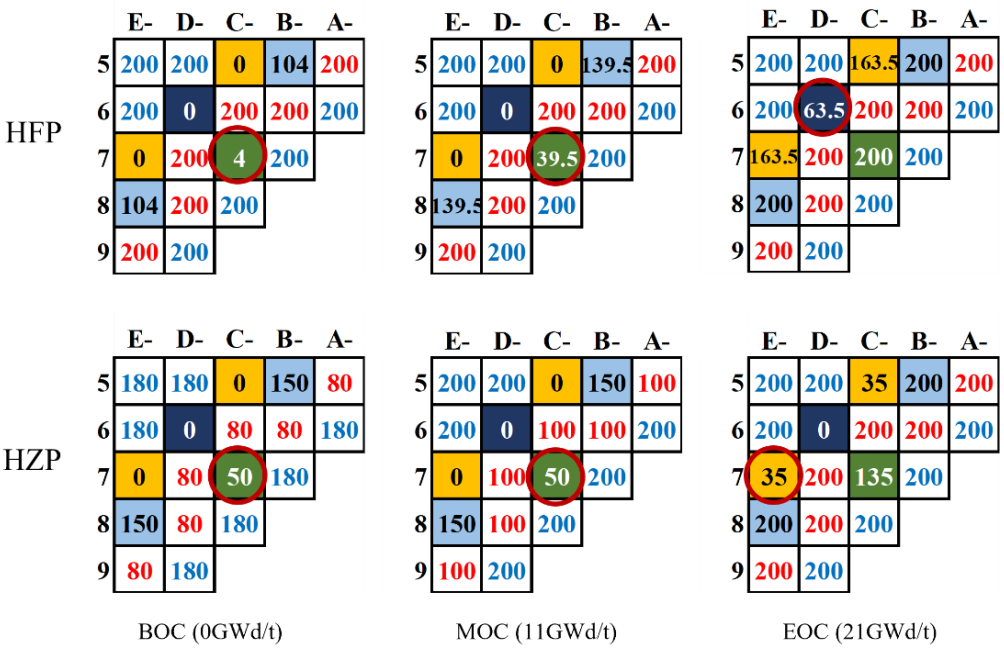

Figure 6.2 Locations of highest control rod worth of CR-A for equilibrium cycle

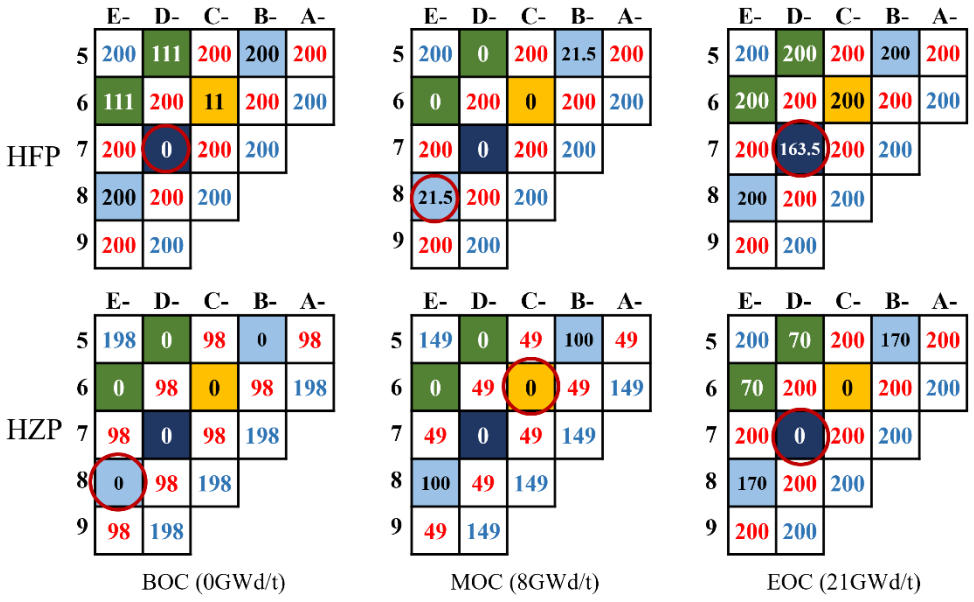

Figure 6.3 Locations of highest control rod worth of CR-B for first cycle

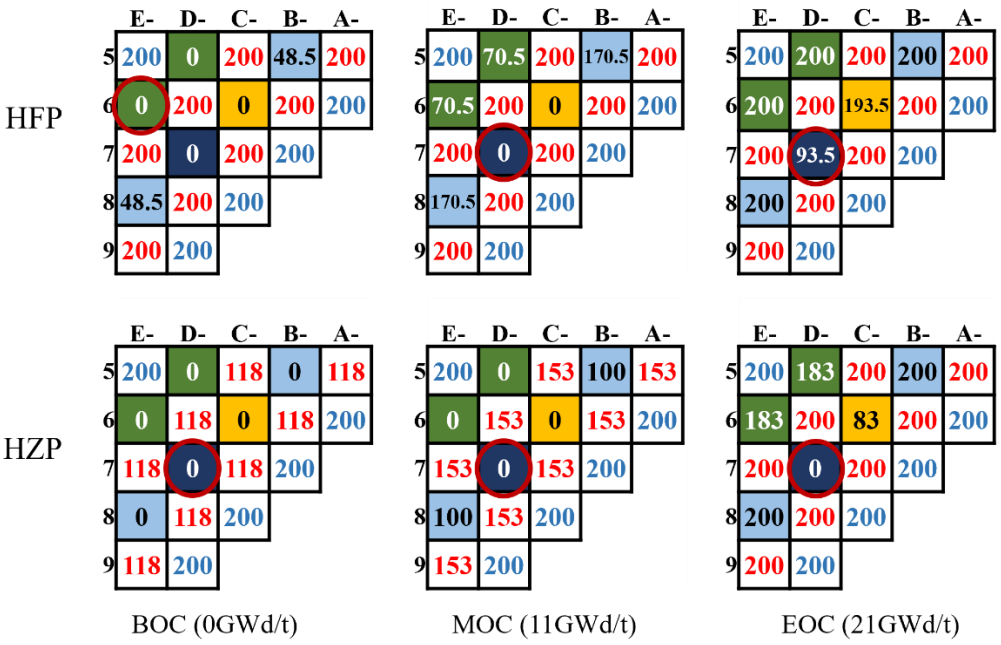

Figure 6.4 Locations of highest control rod worth of CR-B for equilibrium cycle

6.1.3 REA Acceptance Criteria and Safety Limits

An REA is classified as a Level 3a event within the Defense-in-Depth (DiD) framework and is considered a design-basis accident. Therefore, many countries have established their safety criteria. The OECD/NEA report (OECD, 2022) compares regulatory acceptance criteria across 12 member countries. Although criteria vary nationally, the primary safety objectives in REAs remain consistent: to prevent the loss of long-term core coolability and avoid damage to the reactor pressure boundary and core structures due to pressure wave generation. Notably, fuel cladding failure is generally not considered a safety concern (except in Germany). However, REA experimental and modelling efforts have focused extensively on fuel rod failure for several reasons:

- Fuel rod failure is a prerequisite for both the loss of coolable core geometry and the generation of substantial coolant pressure pulses. These complex phenomena exceed the simulation capabilities of standard transient analysis tools such as SIMULATE5-K.
- The mechanisms of fuel failure are more tractable to experimental and analytical investigation than core-wide cooling degradation and structure damage process.

Consequently, the most conservative design criterion is to prevent fuel damage entirely during an REA. If fuel integrity fails, the number of failed rods must be limited to less than 10% of the core inventory to limit the radiological consequence (Stepniewski, et al., 2023).

Specific fuel cladding thresholds during REA (Clifford, 2015) have been established based on different power level:

- Zero Power REA Scenarios: the fuel cladding failure threshold (Figure 6.5) depends on the peak radial average fuel enthalpy and the pressure difference across cladding wall (i.e. internal rod pressure minus reactor pressure). For the radioactive state, a peak fuel enthalpy should be limited within 418.4kJ/kg (100cal/g).

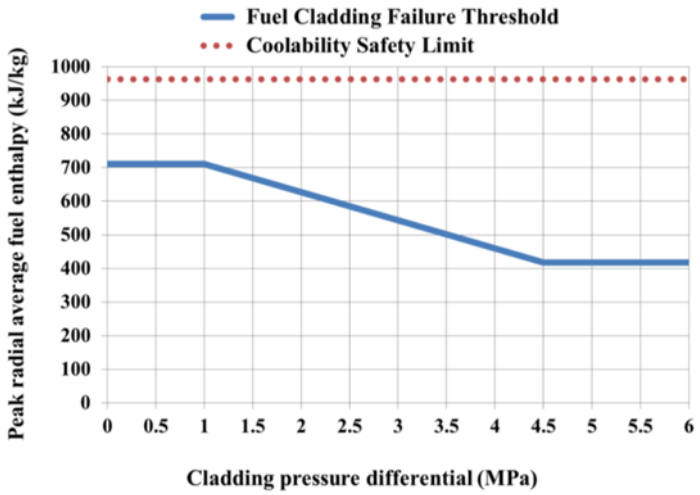

Figure 6.5 REA revised cladding failure threshold and fuel coolability limit (Clifford, 2015), expressed by the peak radial average fuel enthalpy as a function of pressure difference over the fuel cladding (Alzaben Y. I., 2019).

- Intermediate and Full-power Scenarios: Cladding failure is presumed if the local heat flux exceeds the DNB acceptance criterion. The minimum acceptance criterion for the DNB Ratio (DNBR) is 1.3, which is based on a statistical analysis with at least a 95% probability at a 95% confidence level.
- PCMI Failures: This failure mode depends on the peak radial average fuel enthalpy rise and the amount of excess hydrogen uptake in the cladding. Two limits exist based on the cladding's thermal treatment during manufacturing: Fully Recrystallized (RXA) or Stress Relief Annealed (SRA).

The severity of REA is highly dependent on the core's operational state. In typical boron-based light water reactors, the worst case of REA occurs at HZP because more control rods are fully inserted compared to HFP, resulting in a higher ejected CR worth.

However, the characteristics of SBF cores differ from traditional boron-based designs. The elimination of soluble boron means that control rods and burnable absorbers are solely responsible for managing excess reactivity throughout the cycle. This can potentially lead to higher control rod worths in SBF cores compared to boron-based designs. Therefore, for SBF core designs, it becomes essential to investigate REA scenarios originating from both HZP and HFP conditions to comprehensively assess safety parameters against acceptance criteria. The specific core configuration and control rod worth distribution throughout the cycle in an SBF design will determine which operational state presents the most limiting REA scenario.

6.2 Comparison Between Highest-CR-Worth and Delayed Neutron Fraction at HFP/HZP

In this section, the highest control rod worths (ρ_{rod}) and the effective delayed neutron fractions (β-eff) for both CR layouts are compared under HFP/HZP conditions at BOC/MOC/EOC. In the column charts in this section, the orange columns represent the highest CR worths ρ_{rod} at that state, the blue columns are the effective delayed neutron fractions β-eff, and the black lines define the normalized reactivity in dollars: $\rho(\$) = {}^{\rho_{rod}}/_{\beta_{eff}}$.

A negative $\rho(\$)$ indicates an inherent safety margin as it features delayed-supercritical during an REA scenario. Conversely, when $\rho(\$)$ is positive, its value is required to be minimized to ensure the fuel enthalpy below the safety limit to decrease the risk of cladding failure during an REA. By comparing the $\rho(\$)$ for CR-A and CR-B, the better control rod layout will be selected for the further analysis during REA.

6.2.1 Highest-CR-Worth and Delayed Neutron Fraction at First Cycle

The differences between the highest ρ_{rod} and β-eff for CR-A and CR-B at first cycle are summarized in Figure 6.6 and Figure 6.7. For CR-A layout, at HFP,EOC, the highest CR worth is smaller than β-eff, indicating a favourable sub-prompt critical condition. At all states except for HFP,EOC, the highest CR worth exceeds β-eff, leading to prompt critical conditions. The biggest $\rho(\$)$ occurs at HFP,MOC, reaching a value of 1.47$. For CR-B layout, the $\rho(\$)$ is below 1.0 at HFP,BOC/EOC and it is slightly larger than 1.0 at HZP, BOC/MOC. The peak $\rho(\$)$ among all the states occurs at HFP,MOC with a normalized reactivity of 1.64. A consistent observation for both HFP and HZP conditions is that the β-eff decreases as burnup increases.

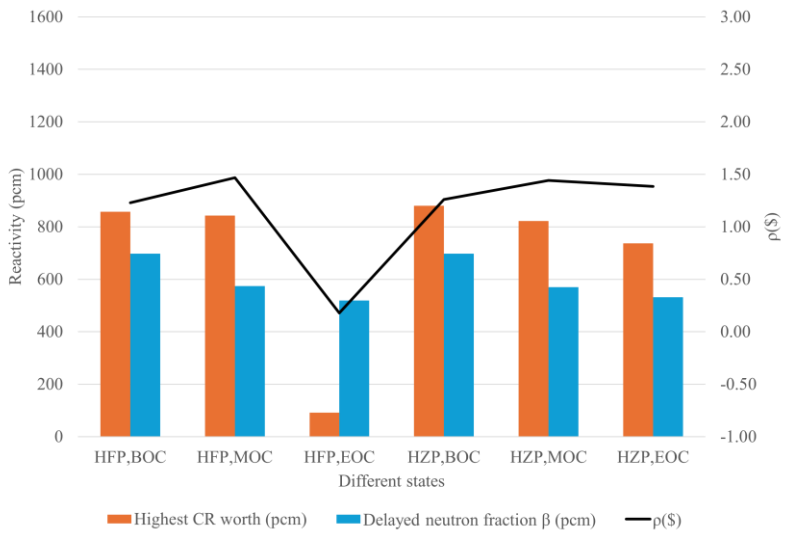

Figure 6.6 The highest-control-rod-worth and delayed neutron fractions at different states for CR-A at first cycle

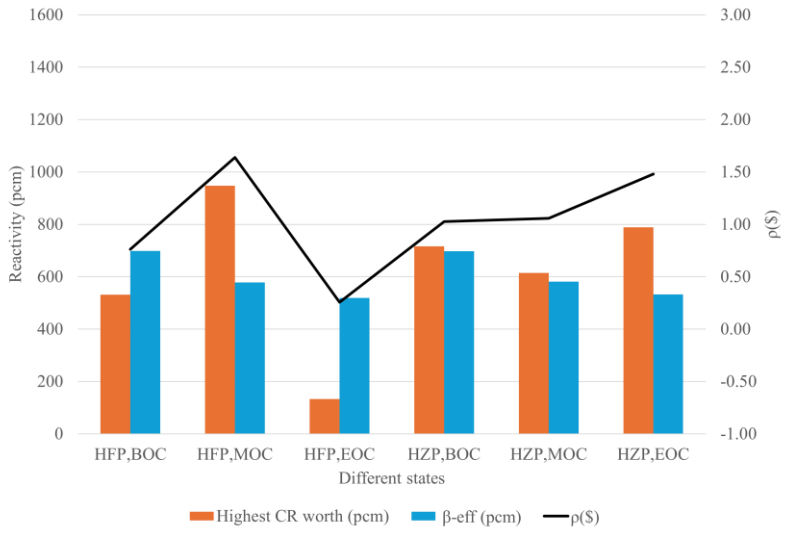

Figure 6.7 The highest-control-rod-worth and delayed neutron fractions at different states for CR-B at first cycle

6.2.2 Highest-CR-Worth and Delayed Neutron Fraction at Equilibrium Cycle

Figure 6.8 and Figure 6.9 summarize the differences between the highest ρ_{rod} and the β-eff for CR-A and CR-B at equilibrium. The equilibrium cycles exhibit significantly smaller peak normalized reactivities than the first cycles. For the CR-A layout, the $\rho(\$)$ is smaller than 1.0 at HFP,EOC and HZP, BOC/MOC, while it is bigger than 1.0 at HFP, BOC/MOC.

For the CR-B layout, $\rho(\$)$ values are confined to a very small range close to 1.0 across all states, peaking at 1.28$ at HZP, EOC. This demonstrates a superior safety margin.

Figure 6.8 The highest-control-rod-worth and delayed neutron fractions at different states for CR-A at equilibrium

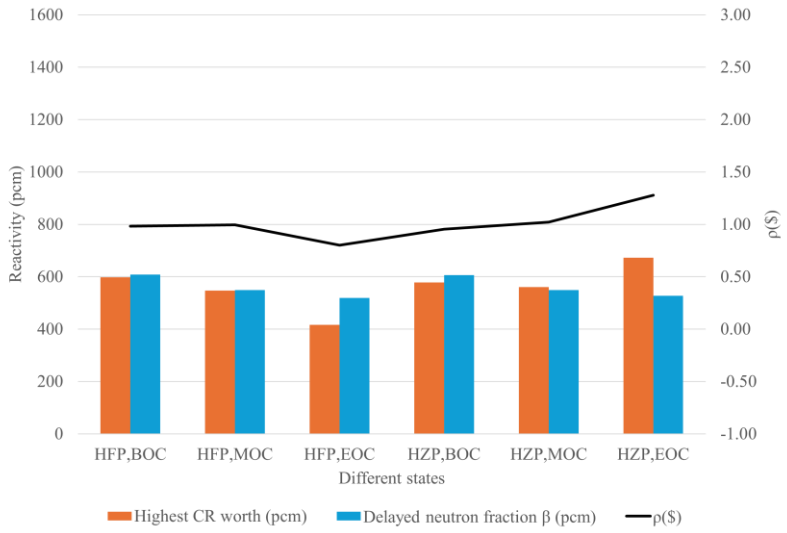

Figure 6.9 The highest-control-rod-worth and delayed neutron fractions at different states for CR-B at equilibrium

Based on the analysis of $\rho(\$)$, the CR-B layout at equilibrium demonstrates a marginally safer performance than CR-A. Therefore, CR-B layout is chosen as the better one among these two control rod layouts. The behavior during REA of CR-B layout in the first and equilibrium cycle will be investigated in detail in the subsequent sections.

6.3 REA Results Analysis in the First-cycle Core

The results analysis is conducted from local and global perspective.

6.3.1 Local Power Response during REA

When a control rod is ejected, the core's radial power distribution changes. Figure 6.10shows the positions of the highest axially-averaged radial power fraction (RPF) for different states, with the circled areas indicating the position of the peak RPF. The peak power fractions are observed at or adjacent to the location of the ejected control rod assemblies for all the states. The reason behind it is that when the control rod is ejected, the localized macroscopic absorption cross-section drops significantly in the assembly. According to the diffusion equation (3.1), a decrease in absorption at the specific location causes a rapid increase in the local neutron flux. Since the local power density is proportional to the fission rate, $P \propto \Sigma_f \cdot \emptyset$, the local flux increase translates into a sharp increase in the local peak RPF.

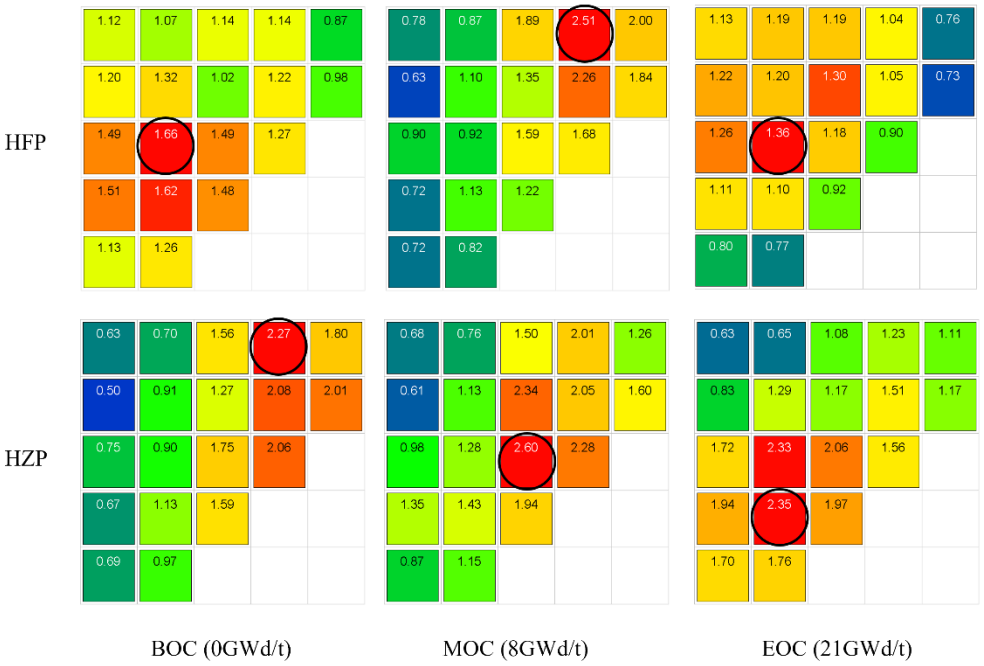

Figure 6.10 Highest axially-averaged radial power fraction for different states

6.3.2 Global Reactivity Response during REA

Figure 6.11 illustrates the evolution of total reactivity during REA for different states. At t=0, the highest-worth control rod is ejected, immediately introducing a positive reactivity insertion. The total reactivities reach their peaks at approximately 0.05s.

For HFP scenarios, the reactivities begin to decline immediately after peaking. The greater the initial positive reactivity introduced, the steeper the subsequent negative gradient. This reactivity decline signifies a prompt feedback mechanism acting to limit the accident.

The HZP scenarios exhibit a different trend compared to HFP. Following the initial rapid reactivity increasement, the reactivity reaches a plateau and remains near its peak value for a duration. This phenomena has also been found in other studies of rod ejection accidents (Mercatali, et al., 2023) (Campos-Muñoz, et al., 2024) (Alzaben, et al., 2019). For MOC and EOC, the reactivities begin their decrease after approximately 0.2s. For BOC, the reactivity starts its gradual decline after approximately 0.6s.

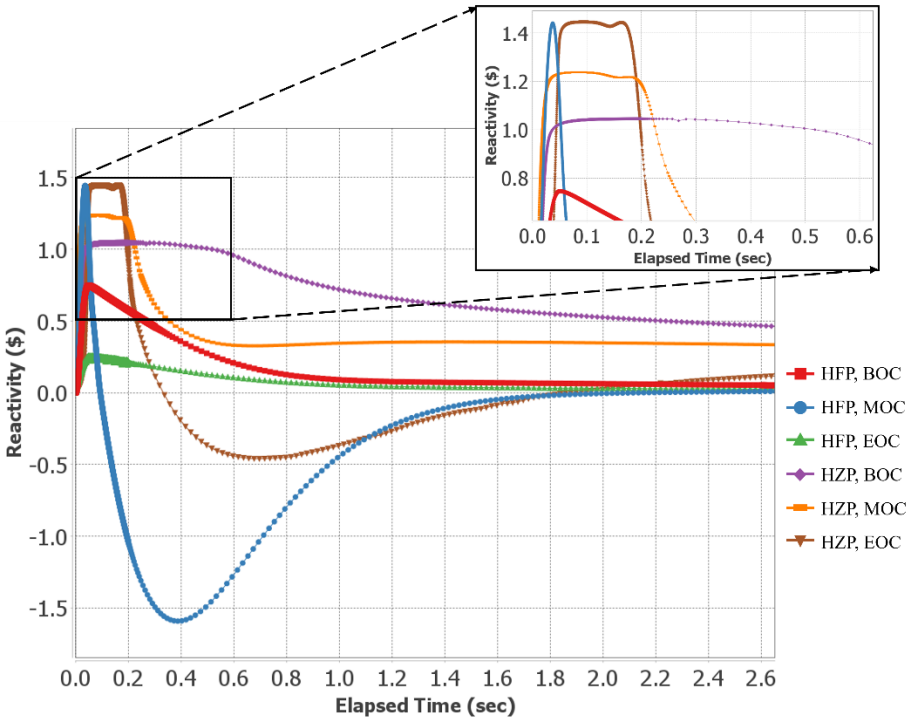

Figure 6.11 Total reactivity variation during REA

To investigate the underlying reasons for the reactivity behaviours for HFP and HZP scenarios, an analysis of the reactivity feedback mechanism from fuel temperature coefficient and the moderator temperature coefficient during REA was performed for HFP, MOC and HZP, MOC, see Figure 6.12. The black lines are the total reactivities, red lines are the reactivities due to fuel temperature coefficient (Doppler effect) and green lines are the reactivities caused by moderator temperature coefficient (Moderator feedback).

The feedbacks for the HFP, MOC scenario is shown in Figure 6.12 (a). The immediate response was the Doppler feedback. This negative reactivity caused the total reactivity to peak and begin to decline at 0.04 seconds. The moderator temperature coefficient, which is also negative, did not have an effect in this short time frame but reached a minimum value of -1.40$ along with the total reactivity -1.60$ around 0.40 seconds. After 2.0 seconds, the total reactivity value stabilizes at a final value of 0.01$.

For the HZP, MOC scenario, both fuel and moderator temperature feedback mechanisms remained at zero until 0.19 seconds. This delay is attributed to the energy deposition mechanisms. Due to the fuel's thermal inertia, a finite period is required for the released energy to accumulate to activate the doppler effect. At 0.19s, doppler feedback responded faster, effectively suppressing the total reactivity between 0.19 and 0.30 seconds and initiating the decrease in total reactivity. Similar to the HFP scenario, the MTC showed a delayed response, reaching a minimum reactivity of -0.37$ at approximately 0.65 seconds. This response contributes to the total reactivity reaching a minimum value of 0.33$ at the same time.

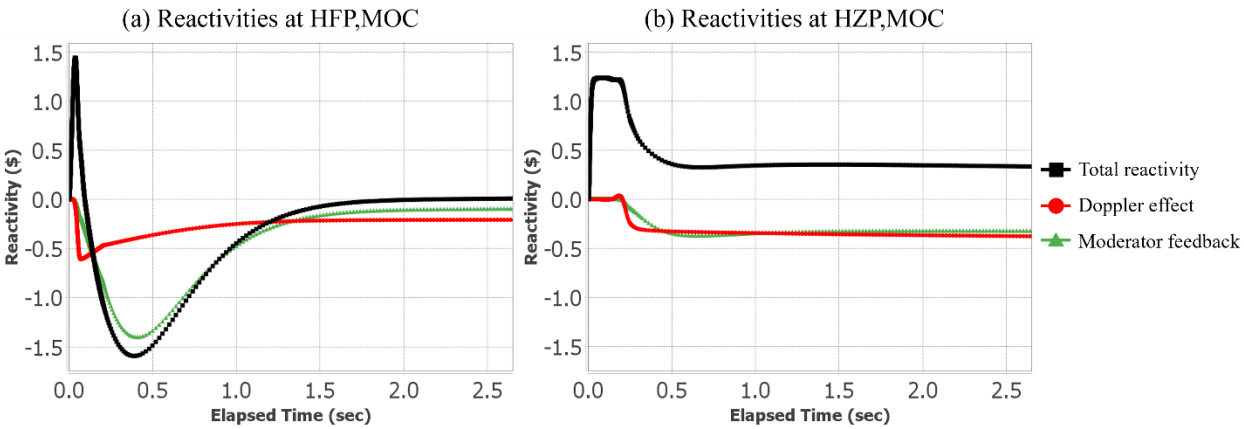

Figure 6.12 Reactivities under HFP,MOC and HZP,MOC

6.3.3 Global Power Response during REA

The global power responses of all the scenarios are displayed in Figure 6.13. In all the HFP scenarios, the highest-worth control rod assembly ejects at t = 0, introducing an immediate sudden insertion of positive reactivity, causing a rapid power surge, activating negative Doppler feedback mechanism (Figure 6.12). The doppler effect causes the total reactivity to decline sharply and eventually stabilize. The most severe accident occurs at MOC due to the maximum reactivity insertion of 1.44$, driving the core into a prompt supercritical condition and causing the highest power spike of 8710% of rated power. Conversely, at BOC, a comparably smaller reactivity insertion of 0.75$ results in a delayed supercritical condition, leading to a significantly lower power spike of 364%. The power peak is mildest at EOC because the control rod bank 1 is inserted by only 36.5cm before REA. This leads to the smallest reactivity insertion of 0.25$, causing the lowest power jump of 131%.

In all the HZP scenarios, the highest-worth control rod assembly also ejects at t = 0, introducing an immediate sudden insertion of positive reactivity. Compared to HFP conditions, the power starts to increase after approximately 0.1s due to the thermal inertia of materials. The negative reactivity feedback mechanisms begin to react after 0.1s (Figure 6.12), which caused reactivity to stay at its peak for a longer time before it starts to decrease after 0.15 s. At MOC and EOC, reactivity insertions of 1.45$ and 1.24$ drive the core into a prompt supercritical condition, yielding power spikes of 2932% and 810%. The power peaks for MOC and EOC are reached between 0.19s and 0.23s. Conversely, the inserted reactivity of 1.04$ at EOC only leads to a slightly prompt supercritical condition, resulting in a peak power of 66% reached at 0.6s.

For all the HFP/HZP scenarios, the global power settles slightly above initial levels in the simulation duration without insertion of control rods, demonstrating the core's self-limiting behavior.

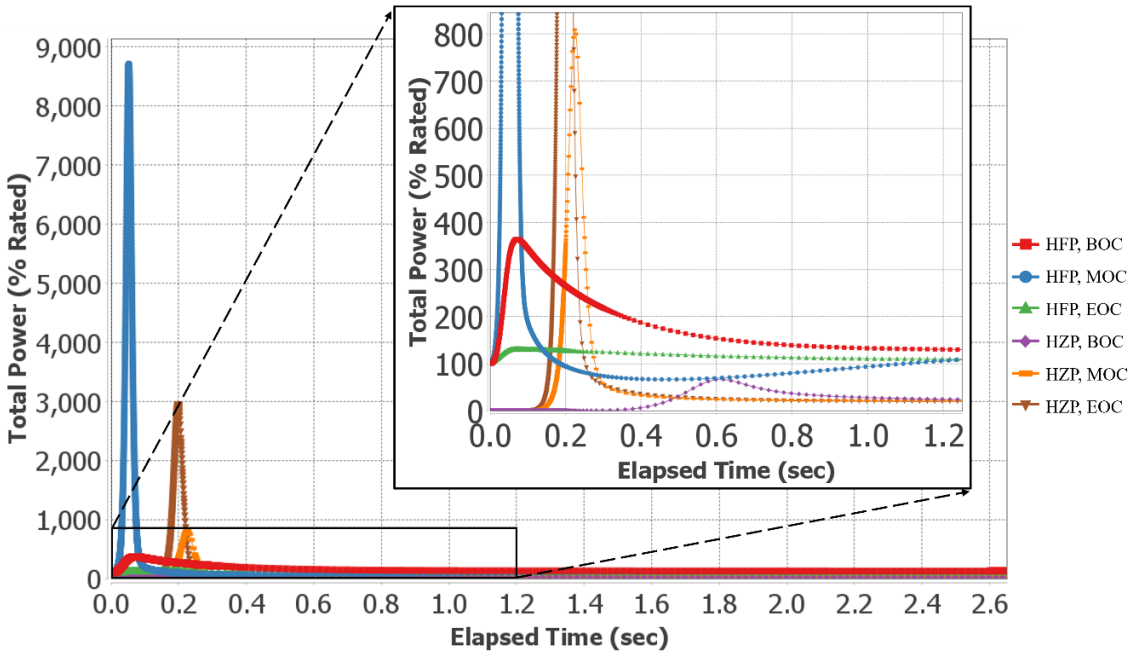

Figure 6.13 Total power rate variation during REA

6.3.4 Fuel Cladding Integrity Parameters and Core Cooling Capability

As previously discussed, the primary safety criterion during REA is to preserve the core's long-term cooling capability by restricting fuel cladding failure to a maximum of 10% of the total fuel volume. To assess this, two parameters are monitored to determine fuel cladding failure thresholds: maximum fuel enthalpy and minimum DNBR. Fuel cladding integrity is considered maintained as long as the fuel enthalpy remains below its maximum limit and DNBR stays above its minimum limit.

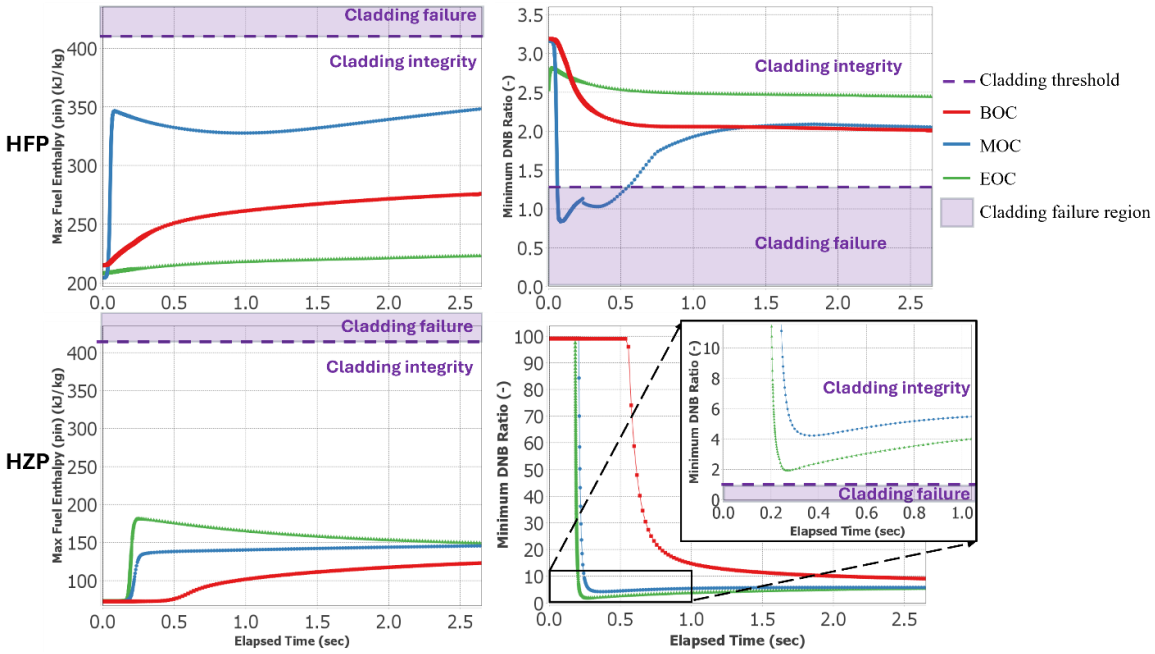

Figure 6.14 Evaluation of fuel cladding integrity under HFP and HZP conditions

As depicted in Figure 6.14, for HZP scenarios, the fuel enthalpies and the MDNBRs remain well within their respective safety limits. Conversely, in the HFP scenarios, while the fuel enthalpies remain below the maximum safety threshold, the MDNBR dropped below its minimum safety limit at MOC, thereby compromising the fuel cladding integrity.

As established by safety criteria during REA (OECD, 2022) (Stepniewski, et al., 2023)(Clifford, 2015), up to 10% of the total core volume is permitted to experience fuel cladding failure. In the SIMULATE5-K output file, the number of cladding-failed pins was recorded as 228 out of a total heated rod count of 15048 in the core. This corresponds to a fuel-cladding-failure percentage of 1.52% of the core volume, which is substantially less than 10% threshold, ensuring the core's cooling capability is maintained.

6.4 REA Results Analysis in the Equilibrium-cycle Core

6.4.1 Local Power Response during REA

Figure 6.15 shows the positions of the highest radial power fraction (RPF) for different states, with the circled areas indicating the position of the ejected control rod. The peak power fractions are observed at or around the ejected control rod assemblies for all the states. Under HFP/HZP condition, at BOC/MOC, the peak power fractions are located at the positions where the rod is ejected. At HFP/HZP,EOC, the peak power is located near the CR-ejected position.

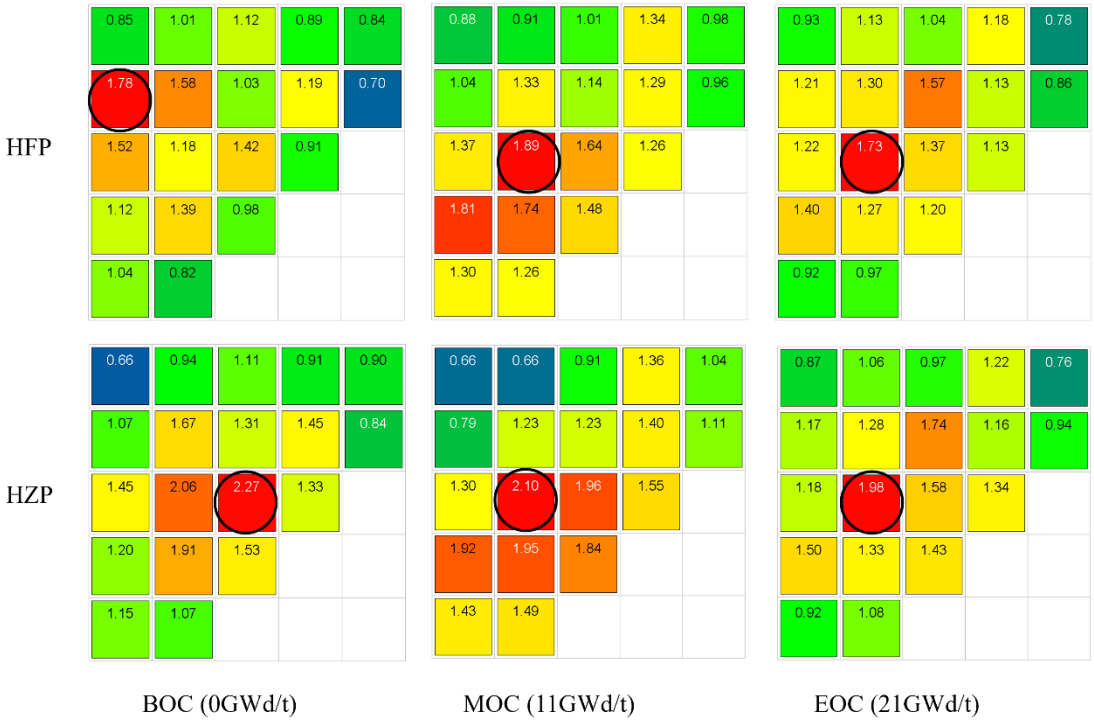

Figure 6.15 Highest radial power fraction and the ejected control rod positions for different states

6.4.2 Global Reactivity Response during REA

Figure 6.16 illustrates the evolution of total reactivity during REA for different states in the equilibrium cycle. At t=0, the highest-worth control rod is ejected, immediately introducing a positive reactivity insertion. The total reactivities reach their peaks at approximately 0.05s. The overall patterns of reactivity variation in the equilibrium cycle are similar to those observed in the first cycle.

For HFP scenarios, the reactivities begin their sharp declines immediately after peaking. The greater the initial positive reactivity introduced, the steeper the subsequent negative gradient.

For HZP scenarios, following the initial rapid reactivity increasement, the reactivity reaches a plateau and remains close to its peak value for a duration. Moreover, larger initial reactivity insertions correspond to a longer duration that the reactivity persists at its peak plateau.

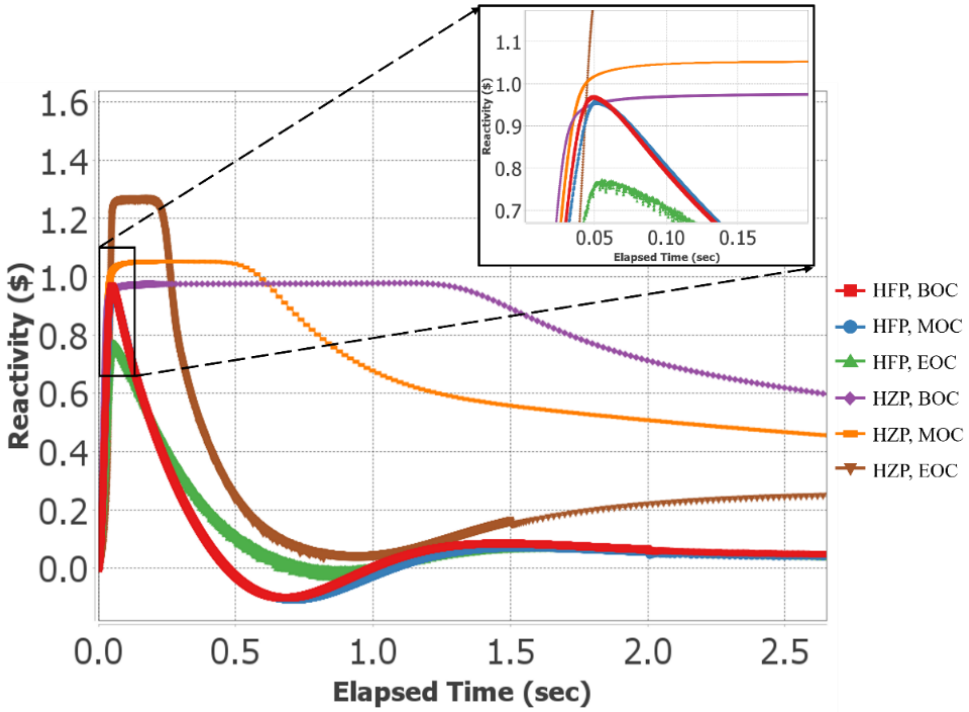

Figure 6.16 Total reactivity variation during REA

To investigate the underlying reasons for the reactivity behaviours for HFP and HZP scenarios, an analysis of the reactivity feedback mechanism from fuel temperature coefficient and the moderator temperature coefficient during REA was performed for HFP, EOC and HZP, BOC, see Figure 6.17. The black lines are the total reactivities, red lines are the reactivities due to fuel temperature coefficient (Doppler effect) and green lines are the reactivities caused by moderator temperature coefficient (Moderator feedback).

Similar to the first cycle, the immediate response is the doppler feedback for both HFP and HZP scenarios while the moderator feedback provides a long-term contribution to the reactivity decrease and final stabilization. For HFP,EOC scenario, the negative doppler feedback causes the total reactivity begin to decline from its peak at 0.04 seconds. For HZP,MOC scenario, both fuel and moderator temperature

feedback mechanisms remained at zero until 1.04 seconds because the HZP initial state lacks the thermal coupling. At 1.04s, doppler feedback responded faster than moderator feedback, effectively suppressing the total reactivity before 1.80 seconds and initiating the decrease in total reactivity.

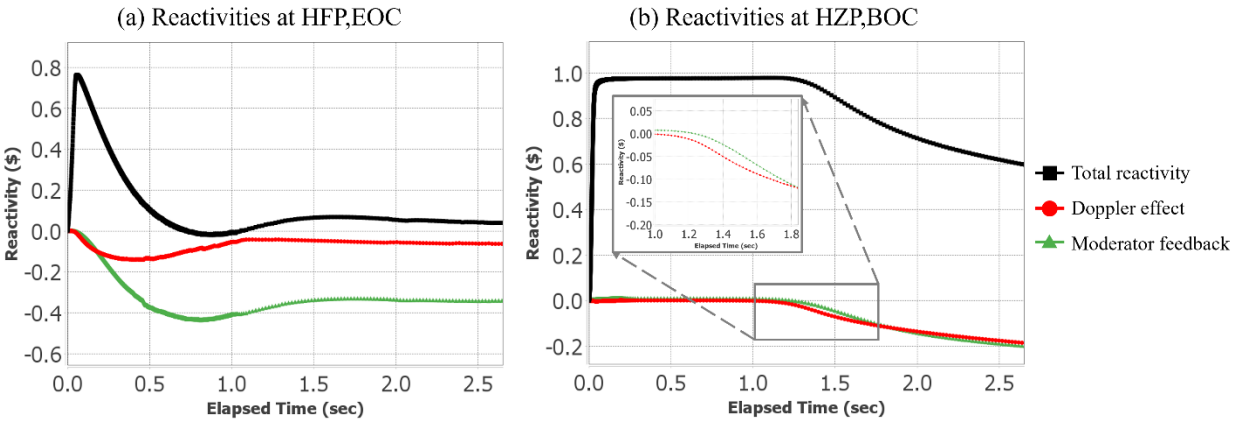

Figure 6.17 Reactivities under HFP,EOC and HZP,BOC

6.4.3 Global Power Response during REA

The global power responses of all the scenarios are displayed in Figure 6.18. The highest-worth control rod assembly ejects at t = 0, introducing an immediate sudden insertion of positive reactivity, causing a rapid power surge, activating negative Doppler feedback mechanism. The doppler effect causes the total reactivity to decline and eventually stabilize.

In all the HFP scenarios, the power spikes are comparably smaller than those observed in the first cycle, with the highest power spike of 993% at BOC. The power spikes for MOC and EOC are 857% and 371%, respectively. This reduction is attributed to ρ($) being smaller than 1.0 in all cases, leading to delayed supercritical conditions.

The HZP scenarios exhibit different patterns in power excursion magnitude and timing. The EOC corresponds to the largest reactivity insertion at HZP, resulting in the highest power spike of 1265%. The peak is reached earliest, at 0.26s. The reactivity insertion at MOC is intermediate, leading to a power spike of 106%. The peak is reached at an intermediate time of 0.62s. The smallest reactivity insertion occurs at BOC, yielding the lowest power spike of 34%. The power peak reached the latest, at 1.44s.

For all the HFP/HZP scenarios, the global power settles slightly above initial levels in the simulation duration without insertion of control rods, demonstrating the core's self-limiting behavior.

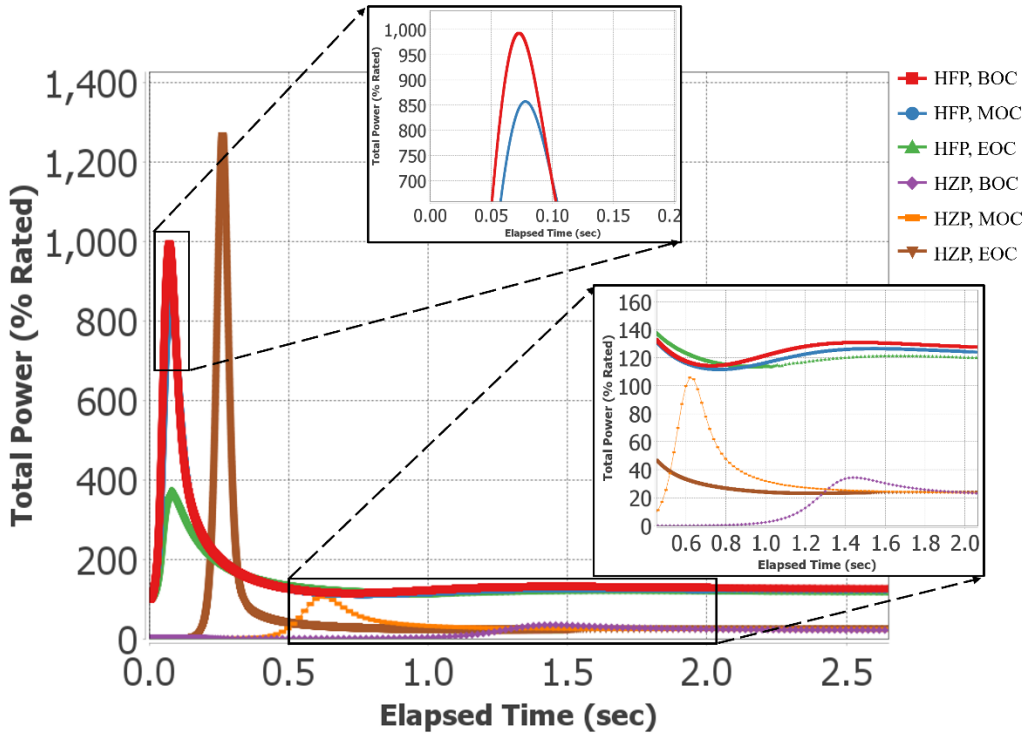

Figure 6.18 Total power rate variation during REA

6.4.4 Fuel Cladding Integrity Parameters

As previously discussed, the primary safety criterion during REA is to preserve the core's long-term cooling capability by restricting fuel cladding failure to a maximum of 10% of the total fuel volume. To assess this, two parameters are monitored to determine fuel cladding failure thresholds: maximum fuel enthalpy and minimum DNBR. Fuel cladding integrity is considered maintained as long as the fuel enthalpy remains below its maximum limit and DNBR stays above its minimum limit.

As depicted in Figure 6.19, for all the HFP and HZP scenarios, the fuel enthalpies and the MDNBRs remain well within their respective safety limits. Therefore, in the equilibrium states, all the fuel cladding interity are maintained.

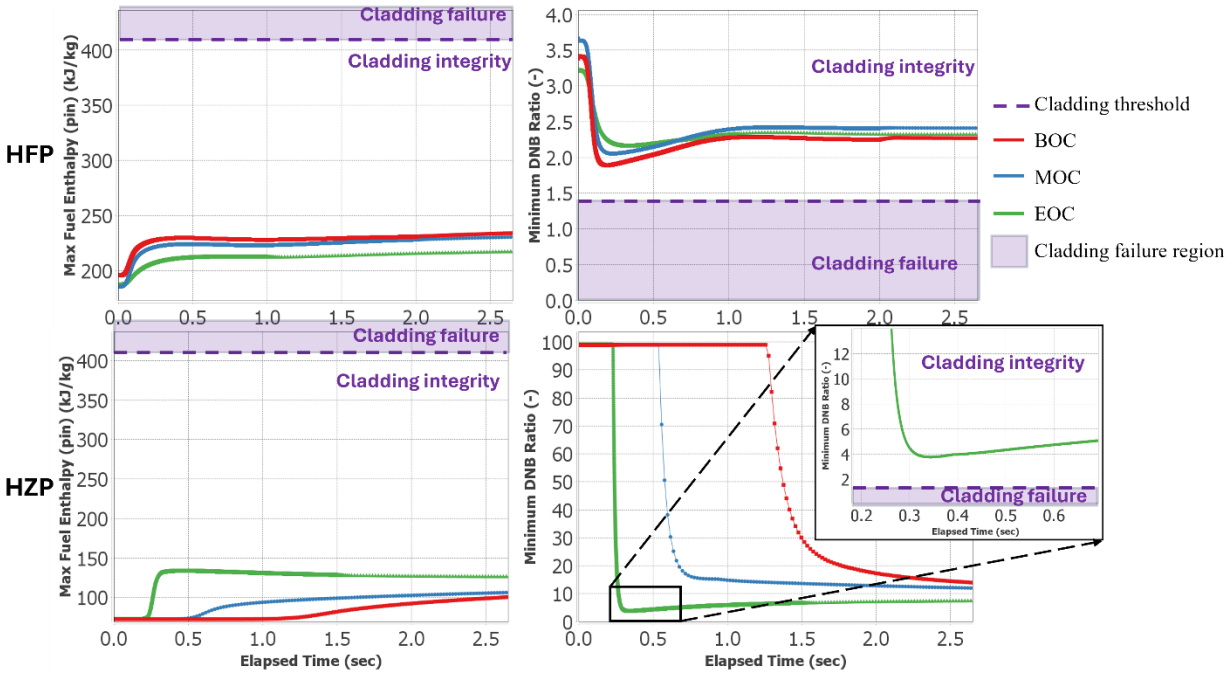

Figure 6.19 Evaluation of fuel cladding integrity under HFP and HZP conditions

In conclusion, in both first and equilibrium cycles, although the positive reactivity and power increase sharply after the rod ejection accident happens, the core's total reactivity decreases due to the doppler effect. This allows the core to return to a stable state without the extra control rod insertion, under both HFP and HZP conditions. Furthermore, the core's cooling capability is maintained during the transient for both first and equilibrium cycles, demonstrating the inherent safety of the designed core during REA. The safety analysis illustrates that the equilibrium cycle demonstrates better performance than the first cycle due to the full maintenance of fuel cladding integrity across all HFP and HZP scenarios.

7 Summaries and Outlooks

This thesis details a comprehensive core design process for a soluble-boron-free small modular reactor, ensuring the final SBF-SMR design satisfies all safety requirements throughout its operational cycle and achieves a target cycle length over 24 months. The methodology integrated fundamental principles from neutronics physics, thermal hydraulics, and reactor safety. With the defense-in-depth principle serving as a guiding framework, the safety criteria for operating conditions, postulated single-failure events, and rod ejection accidents were developed.

The design process relied on two primary deterministic codes, CASMO5 and SIMULATE5. To ensure their reliability, these codes were firstly assessed against the stochastic code SERPENT2, confirming that errors for both the fuel assembly and core models remained within an acceptable range of ±200 pcm. Based on

the parametric study, all subsequent analyses utilized 95 energy groups and a P_3 scattering order in CASMO5.

With the reliability of CASMO5 and SIMULATE5 established, a systematic study was conducted to determine the optimized core designs. After fixing key parameters such as operating conditions and core geometry, the remaining variables—fuel loading strategy, radial control rod layout, enrichment, and the concentration and number of burnable absorber rods—were systematically optimized. The main objective was to find the ideal combination of these variables to achieve the target 24-month cycle length (20 GWd/t) while meeting all safety criteria.

A novel tool, CoreOptimizer, was developed in Golang to automate and streamline this iterative design process. It manages all stages, from input file generation and simulation execution to output data extraction and results visualization. The design for both the first-cycle and equilibrium-cycle cores followed a multi-stage process involving an all-rod-out (ARO) search to analyze reactivity effects, followed by a control rod layout determination, and finally a critical search to identify configurations that met all requirements. For each configuration, two different control rod layouts were analyzed, and the designs for both CR layouts A and B with the lowest 3D peak pin power were selected for further analysis.

The analysis of the optimized cores includes the neutronics and safety characteristics throughout the operational cycle: 3D and 2D pin power fractions, axial power offset, radial power distribution, temperature coefficients and estimation of shutdown margins under all operating scenarios (hot-full-power, hot-zero-power, and cold-zero-power). Additionally, the first-cycle and equilibrium-cycle cores achieve a cycle length of 25.3 months with acceptable fuel exposures, and facilitates excellent heat transfer from the fuel to the coolant.

Finally, a hypothetical rod ejection accident was simulated in the optimized first-cycle and equilibrium-cycle cores with CR-A control rod layout. For these simulations, the REA was conservatively assumed to be completed within a very short duration of 0.05 seconds. Notably, SCRAM (emergency shutdown) was intentionally not considered in these simulations to represent a bounding, worst-case scenario, focusing solely on the inherent response of the core and fuel design to the reactivity insertion. Different scenarios HFP/HZP and different burnup stages BOC/MOC/EOC were investigated to comprehensively assess safety parameters. The results confirmed that the proposed SBF-SMR core design is not only robust under normal operating and performance requirements but also safe enough to handle potential accidents, maintaining its cooling ability even under the rod ejection accident condition.

Based on the investigations and results of this dissertation, several areas for further research and development are recommended.

- Expanded accident analysis. Since the first-cycle and equilibrium-cycle cores have been established, future work can extend the accident analysis in these cores. In addition to the rod ejection accident that was investigated in this study, other design-basis accidents could be simulated to evaluate the

core's inherent safety under a wider range of hypothetical scenarios. Give that the core design uses the operational parameters of KSMR and other parameters of the reactor can be found in Table 1.2 in (Alzaben Y. I., 2019), future simulations could include a loss of coolant accident (LOCA) or a loss of flow accident (LOFA).

- Refuelling strategy optimization: The refueling strategy used in this study was proposed based on a set of rules and is not further optimized. The core's cycle length and fuel utilization could be improved by exploring more refueling management schemes. Machine learning or artificial intelligence approaches could be applied in future research to explore various fuel arrangements to optimize fuel utilization and power distribution.
- Economic study: While this research focused on the neutronic, thermal-hydraulic and safety aspects, future work could include economic studies. This would involve modelling the manufacturing and operational costs of the optimized cores, estimating the potential revenue from electricity generation, and considering the long-term expenses associated with the post-processing and storage of burned fuel assemblies.

References

Abdelhameed, A. A., Nguyen, X. H., Lee, J., and Kim, Y. (2018). Feasibility of passive autonomous frequency control operation in a Soluble-Boron-Free small PWR. *Annals of Nuclear Energy, 116*, 319-333. doi:https://doi.org/10.1016/j.anucene.2018.02.036

Abdelhameed, A., Lee, J., and Kim, Y. (2020). Physics conditions of passive autonomous frequency control operation in conventional large-size PWRs. *Progress of Nuclear Energy*.

Aboanber, A., and Nahla, A. (2004). On pade′ approximations to the exponential function and application to the point kinetics equations. *Progress in Nuclear Energy, 44*(4), 347-368. doi:https://doi.org/10.1016/j.pnucene.2004.07.003

Alam, S. B., Kumar, D., Almutairi, B., Bhowmik, P. K., Goodwin, C., and Parks, G. T. (2019). Small modular reactor core design for civil marine propulsion using micro-heterogeneous duplex fuel. Part I: Assembly-level analysis. *Nuclear Engineering and Design*, 157-175.

Alam, S. B., Kumar, D., Almutairi, B., Ridwan, T., Goodwin, C., and Parks, G. T. (2020). Lattice benchmarking of deterministic, Monte Carlo and hybrid Monte Carlo reactor physics codes for the soluble-boron-free SMR cores. *Nuclear Engineering and Design, 356*, 110350. doi:https://doi.org/10.1016/j.nucengdes.2019.110350

Alzaben, Y. I. (2019). *Neutronics and Thermal-Hydraulics Safety Related Investigations of an Innovative Boron-Free Core Integrated Within a Generic Small Modular Reactor [Doctoral dissertation].* Karlsruher Institut für Technologie (KIT).

Alzaben, Y., Sanchez-Espinoza, V., and Stieglitz, R. (2019). Analysis of a control rod ejection accident in a boron-free small modular reactor with coupled neutronics/thermal-hydraulics code. *Annals of Nuclear Energy, 134*, 114-124. doi:https://doi.org/10.1016/j.anucene.2019.06.009

AREVA NP, I. (2013). *AREVA Design Control Document Rev.5 -- Tier 2 Chapter 04 -- Reactor - Section 4.4 Thermal-Hydraulic Design.* US NRC.

AREVA, I. (2015). *AREA-ARCADIA Rod Ejection Accident.*

Bahadir, T. (2022). Development and Benchmarking of Transient Nodal Code SIMULATE5-K Neutron Kinetics Solver. *PHYSOR.* Pittsburgh, USA. doi:10.13182/PHYSOR22-37639

Bahadir, T., and Grandi, G. (2021). *SIMULATE5 Methodology Proprietary, SSP-10/465 Rev 5.* Studsvik Scandpower, Inc.

Bateman, H. (1910). The solution of a system of differential equations occurring in the theory of radioactive transformations. *Proc. Camb. Phil. Soc., 15*, 423-427.

BBC. (2019). *Hinkley Point C nuclear plant to run £2.9bn over budget*. Retrieved from https://www.bbc.com/news/business-49823305

Becker, B. (2010). *On the influence of the resonance scattering treatment in Monte Carlo codes on high temperature reactor characteristics [Doctoral Thesis].* Stuttgurt, Germany: Institute of Nuclear Technology and Energy Systems, University of Stuttgart.

Bell, G. I., and Glasstone, S. (1970). *The Nuclear Reactor Theory.* New York, NY, USA: Van Nostrand Reinhold Company.

Bowsher, B. R. (1986). *Silver-indium-cadmium control rod behaviour during a severe reactor accident.* UKAEA Atomic Energy Establishment.

Breeze, P. (2014). Chapter 17 - Nuclear Power. In P. Breeze, *Power Generation Technologies (Second Edition)* (pp. 353-378). Newnes.

Bukharin, O. (2006). Russia's nuclear icebreaker fleet. *Science, 14*(1), 25-31. doi:10.1080/08929880600620559

Campos-Muñoz, A., Sanchez-Espinoza, V. H., Redondo-Valerob, E., and Queral, C. (2024). Verification of the Coupled Code PARCS/TWOPORFLOW with Rod Ejection Accident Calculations for Small Modular Reactors. *Nuclear Science and Engineering*, S777-S796. doi:https://doi.org/10.1080/00295639.2024.2357953

Carlvik, I. (1965). A Method for Calculating Collision Probabilities in General Cylindrical Geometry and Applications to Flux Distributions and Dancoff Factors. *Third U.N. International Conference on the Peaceful Uses of Atomic Energy.* Geneva, Switzerland.

Chen, W., Kuang, B., and Guo, L. (2006). New analysis of prompt supercritical process with temperature feedback. *Nucl. Eng. Des., 236*, 1326-1329.

Cho, S. H., Lee, W. J., and Hong, S. G. (2025). Neutronic design and analysis of a soluble boron-free small modular reactor core with GdN-CBA burnable absorber rods for load-following operations. *Annals of Nuclear Energy, 214*, 111203.

Choi, J. Y., Hong, S. G., and Kwon, H. (2020). Conceptual design of a long cycle small modular reactor core with annular UO2 and FCM (TRU) fuels. *International Journal of Energy Research*. doi:https://doi.org/10.1002/er.5957

Clifford, P. M. (2015). *Technical and Regulatory Basis for the Reactivity-Initiated Accident Acceptance Criteria and Guidance.*

Company, W. E. (2011). *4. Reactor, AP1000 Design Control Document, Rev. 18.*

Compton, J., and Clouse, C. (2005). Tiling Models for Spatial Decomposition in AMTRAN. *Proceedings of the Join Russian-American Five-Laboratory Conference on Computational Mathematics/Physics.* Vienna, Austria.

Corporation, W. E. (2005). *Westinghouse Technology Systems Manual - Section 2.2 Power Distribution Limits.* US NRC library.

Crane, S., and Cullen, W. (2004). *Survey of Boric Acid Corrosion Events, Rev.9.* Materials Engineering Branch, Office of Regulatory Research, US Nuclear Regulatory Commission.

Croff, A. (1980). *A User's Manual for the ORIGEN2 Computer Code, ORNL/TM-7175.* Oak Ridge National Laboratory.

Duderstadt, J., and Hamilton, L. (1976). *Nuclear Reactor Analysis.* New York: John Wiley & Sons, Inc.

Dulla, S., Mund, E. H., and Ravetto, P. (2008). The quasi-static method revisited. *Progress in Nuclear Energy, 50*(8), 908-920. doi:https://doi.org/10.1016/j.pnucene.2008.04.009

Duran-Gonzalez, J., Sanchez-Espinoza, V. H., Mercatali, L., Gomez-Torres, A., and Valle-Gallegos, E. d. (2022). Verification of the Parallel Transport Codes Parafish and AZTRAN with the TAKEDA Benchmarks. *Energies, 15*(7), 2476. doi:https://doi.org/10.3390/en15072476

Durazzo, M., and Riella, H. G. (2008). Studies on the Sintering Behaviour of UO2-Gd2O3 Nuclear Fuel. *IYNC 2008*, (p. 114). Interlaken, Switzerland.

Ecomatrix. (2009). *Investigation of the Environmental Fate of Tritium in the Atmosphere. Report: INFO-0792. ISBN 978-1-100-13928-9.* Canadian Nuclear Safety Commission.

Eklund, M., Alamaniotis, M., Hernandez, H., and Jevremovic, T. (2015). Method of characteristics – A review with applications to science and nuclear engineering computation. *Progress in Nuclear Energy, 85*, 548-567. doi:https://doi.org/10.1016/j.pnucene.2015.05.002

EPRI. (1989). *limination of Soluble Boron for a New PWR Design. Report: EPRI-NP-6536.* California, USA.

Evans, T., Stafford, A., Slaybaugh, R., and Clarno, K. (2010). Denovo: A New Three-Dimensional Parallel Discrete Ordinates Code in Scale. *Nucl. Technol., 171*, 171-200. doi:https://doi.org/10.13182/NT171-171

Fernández-Prini, R., and Dooley, R. B. (1997). *The International Association for the Properties of Water and Steam.* Erlangen, Germany.

Ferrer, R. M. (2022). *CASMO5, methodology manual.*

Ferrer, R., and Hykes, J. (2019). Development of a Spatially-Dependent Resonance. *M&C 2019 - International Conference on Mathematics and Computational Methods Applied to Nuclear Science and Engineering.* Portland, Oregon, USA.

Ferrer, R., and Hykes, J. (2021). Improved Rational Approximation for Spatially-Dependent Resonance Self-Shielding in CASMO5. *M&C 2021 – The International Conference on Mathematics and Computational Methods Applied to Nuclear Science and Engineering.* Raleigh, North Carolina, USA.

Ferrer, R., and Rhodes, J. (2014). Extension of Linear Source MOC Methodology to Anisotropic Scattering in CASMO5. *PHYSOR.* Kyoto, Japan.

Ferrer, R., and Rhodes, J. (2021). Generation and initial validation of a new CASMO5 ENDF/B-VIII.0 nuclear data library. *EPJ Web of Conferences*, *247*, p. 09001. Marseille, France. doi:https://doi.org/10.1051/epjconf/202124709001

Fetterman, R. e. (2011). An Overview of the Westinghouse Small Modular Reactor. *ASME 2011 Small Modular Reactors Symposium.* Washington, DC, USA.

Fletcher, J. K. (1983). The Solution of the Multigroup Neutron Transport Equation Using Spherical Harmonics. *Nuclear Science and Engineering, 84*, 33.

G., G., and Tamer, B. (2023). *SIMULATE5-K methodology.*

Galahom, A. A. (2017). Study of the possibility of using Europium and Pyrex alloy as burnable absorber in PWR. *Annals of Nuclear Energy, 110*, 1127-1133. doi:https://doi.org/10.1016/j.anucene.2017.08.052

Glasstone, S., and Sesonske, A. (2012). *Nuclear reactor engineering: reactor systems engineering.* Springer Science & Business Media.

Gold, R. (2017, August 2). Tab swells to $25 billion for nuclear-power plant in georgia. *The wall street journal*. Retrieved from https://www.foxbusiness.com/markets/tab-swells-to-25-billion-for-nuclear-power-plant-in-georgia

Grossi, R. M. (2024). *Climate Change and Nuclear Power.* IAEA.

Gunow, G. A. (2018). *Full Core 3D Neutron Transport Simulation Using the Method of Characteristics with Linear Sources.* Michigan: University of Michigan.

Halfinger, J. A., and Haggerty, M. D. (2012). The B&W mPower™ Scalable, Practical Nuclear Reactor Design. *Nuclear Technology, 178*(2), 164-169. doi:https://doi.org/10.13182/NT11-65

Hennart, J. (1977). Piecewise polynomial approximations for nuclear reactor point and space kinetics. *Nucl. Sci. Eng., 64*(4), 875-901.

Hernandez, H., Knezevic, J., T. Fogal, T. S., and Jevremovic, T. (2013). Visual numerical steering in 3D AGENT code system for advanced nuclear reactor modeling and design. *Ann. Nucl. Energy, 55*, 248-257.

Hong, S., and Cho, N. (1998). CRX: a code for rectangular and hexagonal lattices based on the method of characteristics. *Ann. Nucl. Energy, 25*(8), 547-565.

Hykes, J. (2022). *CASMO5 a fuel assembly burnup program, Proprietary SSP-07/431 Rev 21.* Studsvik Scandpower, Inc.

IAEA. (1981). *Handling of Tritium-Bearing Wastes. IAEA Technical Reports Series No. 203. ISBN 92-0-125081-9.* Vienna.

IAEA. (1998). *Fuel Modelling at Extended Burnup (IAEA-TECDOC-998).* Vienna, Austria: International Atomic Energy Agency.

IAEA. (2006). *Fundamental Safety Principles.* Vienna, Austria: IAEA Safety Standard Series No. SF-1.

IAEA. (2012). *Status of small and medium sized reactor designs: A Supplement to the IAEA Advanced Reactors.* Vienna.

IAEA. (2013). *Design safety considerations for water cooled small modular reactors incorporating lessons learned from the fukushima daiichi accident.* Vienna.

IAEA. (2019). *Design of the Reactor Core for Nuclear Power Plants.* Safety Standards Series No. SSG-52.

IAEA. (2020). *Light water reactor fuel enrichment beyond the five per cent limit: perspectives and challenges.* Vienna: IAEA TECDOC Series.

IAEA. (2020). *Reload Design and Core Management in Operating Nuclear Power Plants .* Vienna: IAEA.

IAEA. (2024). Small Modular Reactors: Advances in SMR Developments 2024. *International Conference on Small Modular Reactors and Their Applications.* Brussels, Belgium.

Ikonen, J.-P., Lindroos, T. J., and Hiltunen, P. (2025). Feasibility of small modular reactors for decarbonizing district heating systems: a case study of the Helsinki metropolitan area. *Nuclear Engineering and Design*, 114262. doi:https://doi.org/10.1016/j.nucengdes.2025.114262

Jo, B. H., and Hah, C. J. (2020). Investigation on long-term daily load follow operation capability of soluble boron-free SMR. *Annals of Nuclear Energy, 149*, 107764. doi:https://doi.org/10.1016/j.anucene.2020.107764

Kang, H. O., Lee, B. J., and Lim, S. G. (2024). Light water SMR development status in Korea. *Nuclear Engineering and Design, 419*, 112966.

KEPCO, and KHNP. (2014). *APR1400 Design control document tier 2: chapter 4.* Maryland: U. S. NRC.

Khoshahval, F., and Akbari, M. (2020). A new method for the solution of the point kinetics equations in the presence of Newtonian temperature feedback. *Progress in Nuclear Energy, 119*, 103165. doi:https://doi.org/10.1016/j.pnucene.2019.103165

Kim, C., and al, e. (2024). Core Design Study for Soluble Boron-Free and Long-cycle Operation of Small Modular Reactor using Enriched Gadolinia. *KNS Spring Meeting.*

Kim, D. (2020). Boron-Free Small Modular Reactor Design by McCARD Burnup Calculation with T/H feedback. *Transactions of the Korean Nuclear Society Autumn Meeting.*

Kooreman, G., and Griesheimer, D. P. (2021). Predictor-Corrector Quasi-Static Method for Tightly-Coupled. *PHYSOR2020. 247.* EPJ Web of Conferences. doi:https://doi.org/10.1051/epjconf/202124707011

KTA. (2012). *Design of Reactor Cores of Pressurized Water and Boiling Water Reactors; Part 2: Neutron-Physical Requirements for the Design and Operation of the Reactor Core and Adjacent Systems.* Germany: Safety Standards Report No. 3101.2 of the Nuclear Safety Standards Commission (KTA).

Kumar, S., Liang, J., Forget, B., and Smith, K. (2020). BEAVRS: An integral full core multi-physics PWR benchmark with measurements and uncertainties. *Progress in Nuclear Energy, 129*, 103488. doi:10.1016/j.pnucene.2020.103488

Lamarsh, J. R., and Baratta, A. J. (2001). *Introduction to nuclear engineering.* Prentice-Hall.

Lassmann, K., and Hohlefeld, F. (1987). The revised URGAP model to describe the gap conductance between fuel and cladding. *Nuclear Engineering and Design*.

Lee, C., Shim, K., Rho, H., Yoon, J., Jeong, H., and Lee, Y. (2025). Full-core fuel analysis of a soluble boron-free SMR: Pellet-cladding interaction issue and enhancing fuel safety through loading pattern design. *Nuclear Engineering and Technology, 57*(10), 103709.

Lee, D. (2024). *5.2 Nuclear Reactor Core Characteristics and Advanced Design Methods of Soluble Boron-free SMRs.* Aix-en-Provence: FJOH summer school.

Leppänen, J. (2015). *Serpent -- a continuous-energy Monte Carlo Reactor Physics Burnup Calculation Code.* Espoo, Finland: VTT Technical Research.

Leppänen, J., Valtavirta, V., Rintala, A., and Tuominen, R. (2025). Status of Serpent Monte Carlo code in 2024. *EPJ Nuclear Sci. Technol., 11*(3). doi:https://doi.org/10.1051/epjn/2024031

Leppänen, J., Valtavirta, V., Tuominen, R., Rintala, A., and Lauranto, U. (2021). A Finnish district heating reactor: Neutronics design and fuel cycle simulations. *International Conference on Nuclear Engineering.*

Li, H., Chen, W., and Zhang, F. (2007). Approximate solutions of point kinetics equations with one delayed neutron group and temperature feedback during delayed supercritical process. *Ann. Nucl. Energy, 34*, 521-526.

Lindley, B., Hosking, J., Smith, P., Powney, D., Tollit, B., Newton, T., . . . Smith, P. (2017). Current status of the reactor physics code WIMS and recent developments. *Annals of Nuclear Energy, 102*, 148-157. doi:https://doi.org/10.1016/j.anucene.2016.09.013

Liu, Y., Yan, R., Zou, Y., Yu, S., Zhou, B., Kang, X., . . . Cai, X. (2020). Sensitivity/uncertainty comparison and similarity analysis between TMSR-LF1 and MSR models. *Progress in Nuclear Energy, 122*, 103289. doi:https://doi.org/10.1016/j.pnucene.2020.103289

Lloyd, C. A., Roulstone, T., and Lyons, R. E. (2021). Transport, constructability, and economic advantages of SMR modularization. *Progress in Nuclear Energy*, 103672. doi:https://doi.org/10.1016/j.pnucene.2021.103672

Lovering, J. R., Nordhaus, T., and Yip, A. (2017). Apples and oranges: Comparing nuclear construction costs across nations, time periods, and technologies. *Energy Policy, 102*, 650-654. doi:https://doi.org/10.1016/j.enpol.2016.11.004

LU Hao-liang, C. J.-l.-n. (2017). Verification and Validation of Self-reliant Core Nuclear Design Code COCO (in Chinese). *Atomic Energy Science and Technology, 51*(8), 1459-1463. doi:10.7538/yzk.2017.51.08.1459

Mart, J. (2013). *Feasibility study on a soluble boron-free small modular reactor.* Master thesis, Oregon State University.

Mart, J., Klein, A., and Soldatov, A. (2014). Feasibility Study of a Soluble Boron–Free Small Modular Integral Pressurized Water Reactor. *Nuclear Technology, 188*(1), 8-19.

Mercatali, L., Huaccho, G., and Sanchez-Espinoza, V.-H. (2023). Multiphysics modeling of a reactivity insertion transient at different fidelity levels in support to the safety assessment of a SMART-like small modular reactor. *Front. Energy Res., 11*. doi:https://doi.org/10.3389/fenrg.2023.1130554

Moreau, F., Sanchez, R., Santandrea, S., I. Zmijarevic, E., and Masiello. (2004). CRONOS2 and APOLL02 results for the NEA C5G7 MOX benchmark. *Prog. Nucl. Energy, 45*(2), 179-200.

Muth, B. (2016). *Parametric Study on Burnable Absorber Rod to Control Excess Reactivity for a Soluble Boron Free Small Modular Reactor.* Cambodia: Institute of Technology of Cambodia.

Myerscough, P. B. (1992). *Nuclear Power Generation, 3rd Edition (British Electricity International)* (Vol. J). Pergamon.

Nahla, A. (2009). An analytical solution for the point reactor kinetics equations with one group of delayed neutrons and the adiabatic feedback model. *Prog. Nucl. Energy, 51*, 124-128.

NewNuclear. (2025, 10 16). *Cold testing of Chinese SMR completed*. Retrieved from World nuclear news: https://www.world-nuclear-news.org/articles/cold-testing-of-chinese-smr-completed

Nguyen, X., Jang, S., and Kim, Y. (2021). Truly-Optimized PWR Lattice for Innovative Soluble-Boron-Free Small Modular Reactor. *Scientific Reports*, 12891.

Ning, B., Yaodong, C., Feng, S., Canhui, S., Zhaocan, M., and Mian, X. (2019). General technology proposal of low-pressurized heating reactor HAPPY200. *Atomic Energy Science and Technology, 53*(6), 1044-1050. doi:10.7538/yzk.2017.youxian.0566

NOBREGA, J. A. (1971). A New Solution of the Point Kinetics Equations. *Nucl. Sci. Eng.* doi:http://dx.doi.org/10.13182/NSE71-A22373

NuScale. (2016). *NuScale Standard Plant Design Certification Application.* US Nuclear Regulatory Commission (NRC) .

O'Neill, R. (1971). Algorithm AS 47: Function Minimization Using a Simplex Procedure. *Applied Statistics, 3*, 338-345.

OECD. (2022). *State-of-the-art Report on Nuclear Fuel Behaviour Under Reactivity-initiated Accident Conditions, NEA No.7575.* NUCLEAR ENERGY AGENCY.

Ott, K., and Madell, J. (1966). Quasistatic treatment of spatial phenomenon in reactor dynamics. *Nuclear Science and Engineering, 26*, 563-565.

P. Suk, O. C. (2021). Simulation of a NuScale core design with the CASL VERA code. *Nuclear Engineering and Design 371*, 110956.

Pinem, S., Sembiring, T. M., Tukiran, Deswandri, and Rina, G. (2018). Reactivity Coefficient Calculation for AP1000 Reactor Using the NODAL3 Code. *Journal of Physics:Conference Series.*

power, N. (n.d.). *Neutron Reflector*. Retrieved from https://www.nuclear-power.com/nuclear-power-plant/nuclear-reactor/neutron-reflector/

Pusa, M. (2011). Rational Approximations to the Matrix Exponential in Burnup Calculations. *Nucl. Sci. Eng., 169*(2), 155-167. doi: doi:https://doi.org/10.13182/NSE10-81

Qing, L., Danrong, S., Wei, Z., Zhang, C., Jia, L., Donghui, W., and Renjie, X. (2020). Overall design and verification of ACP100S floating nuclear power plant. *Nucl. Power Eng., 41*(5), 189-192.

R. Vuiart, A. E. (2024). PRATIC: A soluble-boron-free, pressurized water cooled, SMR core benchmark,. *EPJ - Nuclear Sciences & Technologies 10*.

R., H. G., and F.E., P. (1979). *HEDL-TME72-128.*

Rhodes, J. D. (2005). *Pn-Scattering Results for Simple Criticals with JEF 2.2 and ENDF/B-VI in CASMO-4E SSP-05/455 Rev 1.* Studsvik Scandpower, Inc.

Romano, P. K. (2015). OpenMC: A state-of-the-art monte carlo code for research and development. *Annals of Nuclear Energy*, 90-97.

Santamarina, A., Bernard, D., Blaise, P., and al., e. (2009). APOLLO2.8: A validated code package for PWR neutronics calculations. *Advances in Nuclear Fuel Management IV (ANFM 2009).* Hilton Head Island, South Carolina, USA.

Santandrea, S., Graziano, L., and Sciannandrone, D. (2018). Accelerated polynomial axial expansions for full 3D neutron transport MOC in the APOLLO3® code system as applied to the ASTRID fast breeder reactor. *Annals of Nuclear Energy, 113*, 194-236. doi:https://doi.org/10.1016/j.anucene.2017.11.010

Scott.V, B, T., and al., e. (2021). *SIMULATE5 User's Manual Rev 16.*

Serviere, D. M. (2023). Core Design Studies of a Soluble Boron Free Small Modular Reactor. *Proceedings of the International Conference on Nuclear Energy for New Generations (ICONE).*

Seubert, A., Zwermann, W., and Langenbuch, S. (2006). Solution of the C5G7 3-D Extension Benchmark by the SN Code TORT. *Prog. Nucl. Energy, 48*, 432-438. doi:https://doi.org/10.1016/j.pnucene.2006.01.007

She, D., Wang, K., and Yu, G. (2013). Development of the point-depletion code DEPTH. *Nucl. Eng. Des., 258*, 235-240.

Shen, Q., and Kochunas, B. (2023). High-Order Accurate Solutions of the Point Kinetics Equations with the Spectral Deferred Correction Method. *Nuclear Science and Engineering, 197*(7), 1364-1385. doi:https://doi.org/10.1080/00295639.2022.2159276

Silva, R. C., Bitelli, U. D., and Mura, L. E. (2017). Experimental estimation of moderator temperature coefficient of reactivity of the IPEN/MB-01 research reactor. *International Nuclear Atlantic Conference - INAC.* Belo Horizonte, MG, Brazil.

(n.d.). *SIMULATE-3 Speed-up Models, SSP-97/10.*

Slaybaugh, R., Evans, T., Davidson, G., and Wilson, P. (2013). Multigrid in Energy Preconditioner for Krylov Solvers. *J. Comput. Phys., 242*, 405-419. doi:https://doi.org/10.1016/j.jcp.2013.02.012

Smith, M. A. (2022). *DIF3D-VARIANT Usage Guide, ANL/NSE-22/33.* Argonne national laboratory.

SMR, R.-R. (2024). *Environment, Safety, Security and Safeguards Case Version 2, Tier 1, Chapter 4: Reactor (Fuel and Core).*

Stammler, R., and Abbate, M. (1983). *Methods of Steady-State Reactor Physics in Nuclear Design.* Academic Press.

Steam, X. (2024, April). *Thermodynamic properties of water and steam*. Retrieved from Excel file, version 2.6., .: X Steam, Thermodynamic properties of water and steam. https://github.com/KurtJacobson/XSteam/blob/master/Excel/XSteam_Excel_v2.6.xls

Stepniewski, M., Rudling, P., and Jernkvist, L. O. (2023). *Nuclear Fuel Behaviour under RIA Conditions.* Tollered, Sweden: Advanced Nuclear Technology International.

Stoker, C., and Weiss, Z. (1996). Spatially Dependent Resonance Cross Sections in a Fuel. *Ann. Nucl. Eng., 23*, 765-778.

Tabuchi, M., Yamamoto, A., T. Endo, N. S., Ushio, T., and Mori, M. (2005). Yet Another Optimum Polar Angle Quadrature Set for the Method of Characteristics. *Winter ANS meeting.* Washington, D.C.

TAGIROVA, T. (2025). *Status of RITM Technology Development and Deployment.* ROSATOM.

Tatsuya, F., and Tomohiro, S. (2021). Analysis of the BEAVRS benchmark using CASMO5/SIMULATE5 with JENDL-4.0 and ENDF/B-VII.1. *PHYSOR2020. 247*, p. 02014. EPJ Web of Conferences. doi:https://doi.org/10.1051/epjconf/202124702014

Thomas E. Booth, J. T. (2003). *MCNP–a general Monte Carlo N-particle transport code, version 5.*

Todreas, N. E., and Kazimi, M. S. (2012). *Nuclear Systems Vol I: Thermal Hydraulic Fundamentals.* Taylor&Francis.

Trefethen, L., Weideman, J., and Schmelzer, T. (2006). Talbot quadratures and rational approximations. *BIT Numer. Math., 46*(3), 653-670.

U.S.NRC. (2021). *Appendix A to Part 50—General Design Criteria for Nuclear Power Plants.* U.S.NRC. Retrieved from https://www.nrc.gov/reading-rm/doc-collections/cfr/part050/part050-appa

USGAOffice. (2006). *Report to Congress.* United States Government Accountability Office.

Vidal, J.-F., Frölicher, K., Archier, P., Hébert, A., and Buiron, L. (2021). New reference APOLLO3 calculation scheme for light water reactors - analysis of the BEAVRS benchmark. *PHYSOR2020. 247*, p. 06031. EPJ Web of Conferences. doi:https://doi.org/10.1051/epjconf/202124706031

Viitanen, T. (2015). *Development of a stochastic temperature treatment technique for Monte Carlo neutron tracking, VTT SCIENCE 84.* Espoo, Finland: JULKAISIJA, UTGIVARE.

Vuiart, R., Eustache, A., Eveillard, S., and Prulhière, G. (2024). PRATIC: A soluble-boron-free, pressurized water cooled, SMR core benchmark. *EPJ - Nuclear Sciences & Technologies, 10*.

Wang, G., Yue, Z., Sun, R., Li, D., Liu, X., Wang, B., and Tian, R. (2022). Preliminary study on thermal–hydraulic behavior of loss-of-flow accident in deep pool-type nuclear reactor. *Ann. Nucl. Energy, 170*, 108992. doi:10.1016/j.anucene.2022.108992

Wang, L., and al, e. (2021). Multiple Choices of Reactor Core Nuclear Design for ACP100's Application in Different Scenarios. *EPJ Web Conf.*, 19002.

Wang, Y., Chen, W., Zhang, L., and al., e. (2024). Small Modular Reactors: An Overview of Modeling, Control, Simulation, and Applications. *IEEE Access*. doi:10.1109/ACCESS.2024.3351220

Wang, Y., Wang, Z., Meng, Y., and Xie, H. (2025). Study on safety of advanced integrated natural circulation reactor of NHR200-II under LOCA condition. *Nuclear Engineering and Design, 443*, 114348. doi:https://doi.org/10.1016/j.nucengdes.2025.114348

Weiss, W. (1990). A Consistent Definition of the Number Density of Pseudo-Isotopes. *Ann. Nucl. Energy, 17*(3), 153-156.

Western European Nuclear Regulators Association. (2013). *Safety of New NPP Designs.*

Westinghouse. (2013). *ANC user manual Rev 10.* Westinghouse Electric Company.

Woodcock, E., Murphy, T., Hemmings, P., and Longworth, S. (1965). Techniques used in the GEM code for Monte Carlo neutronics calculation. *Proc. Conf. Appl. Comput. Methods to React. ANL-7050, 3*, 557-579.

Xie, Z., Wu, H., and Zhang, S. (2010). *Nuclear reactor physics analysis (in Chinese).* Xi'an, China: Xi'an Jiaotong University.

Y.Song, and Sánchez-Espinoza, V. (2025). Safety-related Investigations Designing a Soluble-boron-free Small Modular Reactor Core at Equilibrium (Accepted). *EPJ-Nuclear Sciences & Technologies*. doi:https://doi.org/10.1051/epjn/2025077

Y.Song, and Sánchez-Espinoza, V. H. (2026). Neutron-physical and safety-related core design optimization of a soluble-boron-free small modular reactor . In S. X. Tan (Ed.), *Proceedings of the 32nd International Conference on Nuclear Engineering. 6.* Weihai, China: Springer, Singapore. doi:https://doi.org/10.1007/978-981-95-3293-3_37

Yahya, M. S., H.Yu, and Kim, Y. (2015). Burnable absorber-integrated Guide Thimble (BigT) – I: design concepts and neutronic characterization on the fuel assembly benchmarks. *Journal of Nuclear Science and Technology, 53*(7), 1048–1060.

Yamamoto, A. (1998). *Study on Advanced In-Core Fuel Management for Pressurized Water Reactors using Loading Pattern Optimization Methods.* Kyoto: KYOTO UNIVERSITY.

Yamamoto, A., Tatsumi, M., Sugimura, N., and al., e. (2007). Numerical solution of stiff burnup equation with short half lived nuclides by the Krylov subspace method. *J. Nucl. Sci. Technol., 44*(2), 147-154.

Yamoah, S., Akaho, E., and Nyarko, B. (2013). An accurate solution of point reactor neutron kinetics equations of multi-group of delayed neutrons. *Annals of Nuclear Energy, 54*, 104-108.

Yu, Y., He, X., Cheng, M., and Dai, Z. (2025). Review of the Discrete-Ordinates Method for Particle Transport in Nuclear Energy. *Energies, 18*(11), 2880. doi:https://doi.org/10.3390/en18112880

Zain, J. A., Hajjaji, O. E., Bardouni, T. E., and Lahdour, M. (2021). Validation of deterministic code DRAGON5 for the fuel depletion analysis of a PWR pin-cell benchmark. *Radiation Physics and Chemistry, 186*, 109545. doi:https://doi.org/10.1016/j.radphyschem.2021.109545

Zhang, B., Li, Q., Cai, Y., Liu, K., and al., e. (2022). Validation and verification for nuclear design software package TORCH V2.0 of pressurized water reactor (in Chinese). *Atomic energy science and technology, 56*.

Zhou, X., Zhang, D., Li, X., Deng, J., Tian, W., Qiu, S., . . . Yu, H. (2024). Development of a neutron space–time kinetics solver with improved quasi-static method based on OpenFOAM. *Nuclear Engineering and Design*, 112990. doi:https://doi.org/10.1016/j.nucengdes.2024.112990

Ziver, A., Shahdatullah, M., Eaton, M., Oliveira, C. d., Umpleby, A., Pain, C., and Goddard, A. (2005). Finite element spherical harmonics (PN) solutions of the three-dimensional Takeda benchmark problems. *Annals of Nuclear Energy, 32*(9), 925-948. doi:https://doi.org/10.1016/j.anucene.2005.01.009

Zverev, D. L., Pakhomov, A. N., Polunichev, V. I., Veshnyakov, K. B., and Kabin, S. V. (2013). RITM-200: new-generation reactor for a new nuclear icebreaker. *Atomic Energy, 113*, 404-409.

Appendix A Isotopes of the 2-D Lattice Models in CASMO5 and SERPENT2

Table 7-1 Isotopes and their mass fraction of the 2-D lattice model

Materials	Isotopes	Mass fraction
Air	C-12	0.00022
	C-13	0.00000
	O-16	0.22793
	O-17	0.00009
	O-18	0.00053
	N-14	0.74291
	N-15	0.00291
	Ar-36	0.00008
	Ar-38	0.00002
	Ar-40	0.00000
Stainless steel 304	Si-28	0.00551
	Si-29	0.00029
	Si-30	0.00020
	Cr-50	0.00793
	Cr-52	0.15903
	Cr-53	0.01838
	Cr-54	0.00466
	Mn-55	0.02000
	Fe-54	0.03862
	Fe-56	0.62860
	Fe-57	0.01478
	Fe-58	0.00200
	Ni-58	0.06720
	Ni-60	0.02678
	Ni-61	0.00118
	Ni-62	0.00383
	Ni-64	0.00101
Ag-In-Cd	Ag-107	0.41101
	Ag-109	0.38899
	In-113	0.00633
	In-115	0.14367
	Cd-106	0.00059

	Cd-108	0.00043
	Cd-110	0.00611
	Cd-111	0.00631
	Cd-112	0.01201
	Cd-113	0.00614
	Cd-114	0.01456
	Cd-116	0.00386
Inconel718	Si-28	0.00322
	Si-29	0.00017
	Si-30	0.00012
	Cr-50	0.00791
	Cr-52	0.15870
	Cr-53	0.01834
	Cr-54	0.00465
	Mn-55	0.00870
	Fe-54	0.01616
	Fe-56	0.26311
	Fe-57	0.00619
	Fe-58	0.00084
	Ni-58	0.34399
	Ni-60	0.13707
	Ni-61	0.00606
	Ni-62	0.01963
	Ni-64	0.00516
Zr-4	O-16	0.00125
	O-17	0.00000
	O-18	0.00000
	Cr-50	0.00004
	Cr-52	0.00084
	Cr-53	0.00010
	Cr-54	0.00002
	Fe-54	0.00012
	Fe-56	0.00193
	Fe-57	0.00005
	Fe-58	0.00001
	Zr-90	0.49750

	Zr-91	0.10970
	Zr-92	0.16953
	Zr-94	0.17554
	Zr-96	0.02888
	Sn-112	0.00013
	Sn-114	0.00009
	Sn-115	0.00005
	Sn-116	0.00206
	Sn-117	0.00110
	Sn-118	0.00349
	Sn-119	0.00125
	Sn-120	0.00477
	Sn-122	0.00069
	Sn-124	0.00088

Appendix B Conversion Between Cycle Burnup and Operational Time

The accumulated change in material composition effects the operational cycle length of the reactor core. This cycle length is quantified by fuel burnup, which is the thermal energy output per metric ton of initial heavy metal in the fuel, commonly denoted as MWd/t or GWd/t. This burnup unit (GWd/t) can also be used to indicate the duration of a core's operational cycle. While cycle length is commonly expressed in months, the conversion from cycle exposure to operational months varies for different reactor cores. In the context of core design, the conversion can be calculated as follows, taking a burnup of 20GWd/t as an example.

The cycle length is predicted as follows: Prediction of the volume of one fuel rod is expressed in (*7.1*), the volume of UO_2 in the core is calculated in (*7.2*). Therefore, the mass of UO_2 in the core is calculated in (*7.3*), leading to the mass of U in the core expressed in (*7.4*).

$$V_{rod} = \pi \times r^2 \times h = \pi \times 0.39218^2 \times 200 = 96.6cm^3 \tag{7.1}$$

$$V_{UO2} = V_{rod} \times N_{rod} \times N_{FA} = 96.6 \times 240 \times 57 = 1322016cm^3 \tag{7.2}$$

$$m_{UO2} = \rho \times V_{UO2} = 10.4 \times 1322016 = 13748971g \tag{7.3}$$

$$m_U = m_{UO2} \times 88.147\% = 12119305g = 12.12t \tag{7.4}$$

Finally, the total released energy is calculated in (*7.5*) and the corresponding operational months is calculated in (*7.6*).

$$\text{energy released} = \frac{20\text{GWd}}{\text{t}} \times 12.12\text{t} = 242.4\text{GWD} \tag{7.5}$$

$$\text{operation months} = \frac{242.4\ GWd}{0.33GW \times 30.44\ days/month} = 24.1 \tag{7.6}$$

Using these conversion equations, the correspondence of cycle length with the units of GWd/t and months are listed in Table 7-2. For this study, a target burnup of 20 GWd/t corresponds to 24.1 operational months.

Table 7-2 Conversion of cycle burnup to cycle length

Cycle burnup (GWd/t)	Cycle length (months)
16	19.3
17	20.5
18	21.7
19	22.9
20	24.1
21	25.3
22	26.5
23	27.8